論文 / 著書情報
Article / Book Information

題目(和文)	肝臓画像分割のためのレベルセットに基づく能動的輪郭法に関する研究
Title(English)	Study of a Level-Set Based Active Contour Method for Liver-Image Segmentation
著者(和文)	Narkbuakaew Walita
Author(English)	Walita Narkbuakaew
出典(和文)	学位:博士（工学）, 学位授与機関:東京工業大学, 報告番号:甲第9878号, 授与年月日:2015年3月26日, 学位の種別:課程博士, 審査員:長橋　宏,熊澤　逸夫,小池　康晴,山口　雅浩,小尾　高史
Citation(English)	Degree:, Conferring organization: Tokyo Institute of Technology, Report number:甲第9878号, Conferred date:2015/3/26, Degree Type:Course doctor, Examiner:,,,,
学位種別(和文)	博士論文
Type(English)	Doctoral Thesis

Study of a Level-Set Based Active Contour Method for Liver-Image Segmentation

By
Walita Narkbuakaew

Department of Information Processing
Interdisciplinary Graduate School of Science and Engineering
Tokyo Institute of Technology

This Dissertation is submitted for the degree of Doctoral of Engineering
March 2015

Acknowledgements

I would like to thank the Thai Government Science and Technology Scholarship and Royal Thai Embassy for supporting my study in a whole period of the doctoral program. I greatly appreciate Professor Hiroshi Nagahashi, my academic advisor, who gives opportunities, supports, and encouragements. I really thank assistant professor Kota Aoki and assistant professor Yoshiki Kubota for all invaluable suggestions. Thank all persons, who support me. Lastly, I would like to thank my parents for love and everything.

Abstract

This thesis proposes a 3D CT liver-image segmentation system based on a level-set image segmentation method. It consists of three main modules. First, the construction of confident region images is proposed. It describes approximate liver regions as homogeneous regions after boundaries of anatomical structures are determined by a combination of gradient information. In the second module, a two-resolution level-set image segmentation approach is introduced. This approach firstly performs level-set image segmentation at the low-resolution. Then, its result is used for the initialization process of level-set image segmentation at the original resolution. This approach contains two main components including initialization and level-set evolution processes. The initialization process is studied to construct the good initial zero level-set function. Furthermore, it generates mask regions for preventing the leakage regions after the evolution process is performed. For the level-set evolution process, a modified Chan-Vese model is proposed to control directions of the curve propagation. Finally, the segmentation result is refined in the last module.

The proposed system was applied to 3D CT images acquired by a 4D-CT imaging system. From experimental results, the proposed system possibly gives higher accuracy than some modern level-set image segmentation methods. After a liver-segmented volume is extracted, two kinds of its applications are investigated in this study.

The first application is liver-tumor segmentation. The integration of modified Chan-Vese model and a clustering method is examined to segment tumor regions in a noisy image. It is assumed that a segmented liver-region includes several tumor areas, which are possibly approximated by a clustering result.

In the second application, enhancement in visualization of anatomical structures is considered. The segmentation result is combined with the original 3D-CT data before applying a ray-casting technique. This combination probably improves visualization of anatomical structures. Moreover, opacity and color transfer functions are simply studied for controlling appearances of segmented volumes.

Table of Contents

Chapter 1
Introduction

1.1 Motivation and challenges

Liver cancer is the second most common cause of worldwide cancer deaths in 2012 as mentioned by IARC GLOBOCAN [1], and it has been one of the four most common causes of cancer death since 1975 [2].

To diagnose liver cancer, anatomical structures and tumors are visualized by one or several imaging systems [3], such as ultrasound, computed tomography (CT), magnetic resonance imaging (MRI), angiography, laparoscopy, and so on. Generally, a CT scanner is utilized to seek abnormalities or signs of cancer in the liver and other organs. After diagnosing and staging the liver cancer, a multidisciplinary treatment team, which includes different types of specialists, such as a surgeon, a radiation oncologist, a medical oncologist, and a gastroenterologist, will decide a treatment option for a patient [3, 4]. For example, the liver transplantation may be chosen when the cancer has not spread out of the liver and a suitable liver is available. Hepatectomy is to remove a portion of liver including the cancer, and then the liver tissue grows back to its normal size. However, this option is suitable for a patient who does not have cirrhosis. Further, if the cancers are too large or spread beyond the liver, this treatment option will be cancelled. Radiation therapy is to deliver high-energy to eliminate cancer cells by destroying their DNA. Conversely, this treatment option is a limited use because the radiation of high-energy can damage healthy liver tissue.

Actually, many treatment options relate to liver-image segmentation. For example, the liver-image segmentation is used to determine the liver's volume [5] that is essential information of liver surgery for primary hepatic tumors, metastatic lesions, and transplantation. Further, it is utilized to plan radiation treatments that need to maximize high radiation energy on the cancer cells and minimize the radiation energy on the nearby healthy tissues [6].

This study mainly considers liver-image segmentation in CT images acquired by a 4D-CT imaging system. It is a challenging topic because of large variations in shapes and sizes. Moreover, some ranges of gray-intensities of liver generally overlap other soft tissues. CT data sometimes presents high levels of image noises, some

artifacts, low image contrast, and weak edges due to the conditions of image acquisition and respiratory status [7, 8].

1.2 Literature review

Many algorithms [9, 10, 11] have been proposed to give high efficiency of liver-image segmentation and reduce user involvement. In recent years, four kinds of fundamental image-segmentation methods have been proposed to segment liver in CT images.

First, region-growing based methods consider properties of seed regions and their neighbor pixels or voxels to grow them. For instance, a semi-automatic liver segmentation system called HepaTux [12] was presented to segment the liver in three main steps. The interactive filling is started to flood-fill the volume from seed voxels, and it is stopped by the non-linear coupling criterion. Next, segmented results are corrected by cutting leakage regions, and then post processing is performed to refine the 3D liver's shape.

The second kind is graph-cut based methods. These methods represent pixels or voxels as vertices, which are connected by edges. Meanwhile, the weight of edge connecting two adjacent vertices is used to describe the similarity between two connected vertices. Further, these methods require some seed regions of foreground and background regions. Then, the cost function is fundamentally formulated by using a combination of boundary and region terms. However, these methods sometimes need additional seed regions to refine the segmentation results. For example, a segmentation refinement approach [13] was introduced to segment the liver by using a graph-cut segmentation algorithm [14] and two refinement steps. The first refinement allows a user to add or remove volume chunks to or from the current result. Further, the editing tool [15] is required to perform the second refinement.

Third, level-set based methods begin with a rough contour, and then it is evolved under the speed function or energy function. Indeed, the speed function plays an important role to control directions of the curve propagation. For example, the speed of the propagation process is adaptively controlled by a dynamic speed function [16]. It is utilized to control contours after rough contours are manually created inside the liver. It is also used to achieve a semi-automatic liver-segmentation application [17].

Furthermore, probabilistic atlases based methods are grouped into the fourth kind. These methods require manual segmentation to obtain a probability value in each pixel or voxel from large training image data. In fact, it is necessary to transform

all training images into a common space by using affine transformation. Then, the posterior probability is used to segment the object of interest. For example, nonrigid atlas matching [18] was introduced to segment the liver. The atlas is created from twenty training images by using two image-registration methods. It subsequently computes an affine transformation using the mutual information metric [19] and a B-spline non-rigid registration [20]. For segmentation in a test image, the probabilistic atlas segmentation is transformed into the test image. Then, the thresholding is applied to the transformation result before employing a morphological opening and removing unconnected components. However, this approach consumes long computation time caused by the nonrigid registration method and it is dependent on the precision of manual drawing in the training images.

1.3 Objectives

This study proposes an efficient liver-image segmentation system based on a level-set method. It is aimed to segment the liver volume in CT images acquired by a 4D-CT imaging system.

Subsequently, an example of liver-tumor segmentation is studied. Moreover, a simple visualization tool is designed and developed to demonstrate an example of liver-image segmentation application. In this example, a liver-segmented volume is combined with an original 3D-CT data before applying a ray-casting technique. This combination helps to enhance visualization of liver in the ray-casting result. Therefore, these objectives support a simple pipeline of liver-image segmentation application as shown in Figure 1-1.

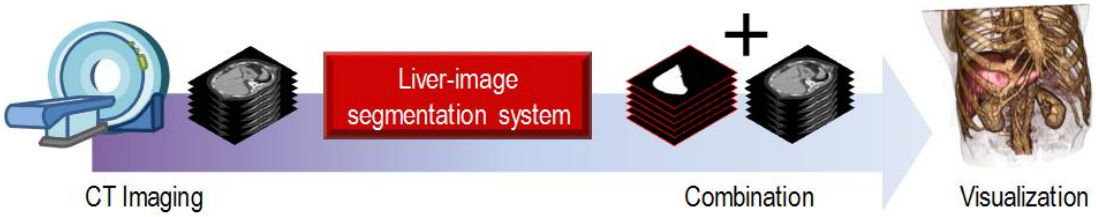

Figure 1-1 An example of a simple pipeline of liver-image segmentation application

1.4 Thesis structure

This thesis is organized as follows. Chapter 2 briefly explains related methods containing level-set image segmentation with free re-initialization, geodesic active contour (GAC), active contour without edges or Chan-Vese (CV), and edge based level-set method. Chapter 3 describes the proposed 3D CT liver-image segmentation

system. It includes construction of confident region image, generation of initial zero level-set function, and a modified Chan-Vese model. Chapter 4 shows experimental results and two major issues are investigated. First, it shows the influence of types of image representations on standard level-set methods. Second, it demonstrates a performance of the proposed modified Chan-Vese model in a comparatives assessment. Afterwards, two related applications of liver-image segmentation are studied and described in chapters 5 and 6. Chapter 5 introduces an integration of the modified Chan-Vese model and a clustering method. It is aimed to illustrate an idea for segmenting tumor regions after a liver-segmented region is presented. However, in this study, the proposed method was applied to an eight-bit mock liver-tumor image. Chapter 6 presents a visualization application. A simple visualization tool is developed to support a ray-casting technique. It is aimed to visualize anatomical structure after the segmentation result is integrated into the original image data. Lastly, all studies are concluded in the chapter 7.

Chapter 2
Level-Set Image Segmentation

2.1 Introduction

This chapter briefly explains general concepts of level-set image segmentation. Section 2.2 describes definition of a level-set method. Section 2.3 shows a summary of level-set image segmentation with free re-initialization. Section 2.3 summarizes concepts of a geodesic active contour (GAC), a Chan-Vese (CV) model, and an edge-based level-set method.

2.2 A Level-Set Method

In a basic description, the level-set function describes an objective function in different levels of the cut-planes. A contour at the zero-level is called the zero level-set function. For example, a function of a surface $\phi(x,y) = \sqrt{x^2+y^2} - 1$ is separately described by a constant in a z-axis (see Figure 2-1.) The zero level-set function is outlined by the red contour (it is sometimes called front). Due to this definition, the red front represents implicit-curve properties as a signed distance function as

$$\phi(x,y)\begin{cases} < 0 & \text{if } (x,y) \text{ is inside } C, \\ = 0 & \text{if } (x,y) \in C, \\ > 0 & \text{if } (x,y) \text{ is outside } C. \end{cases} \tag{2.1}$$

where C denotes the given contour or front.

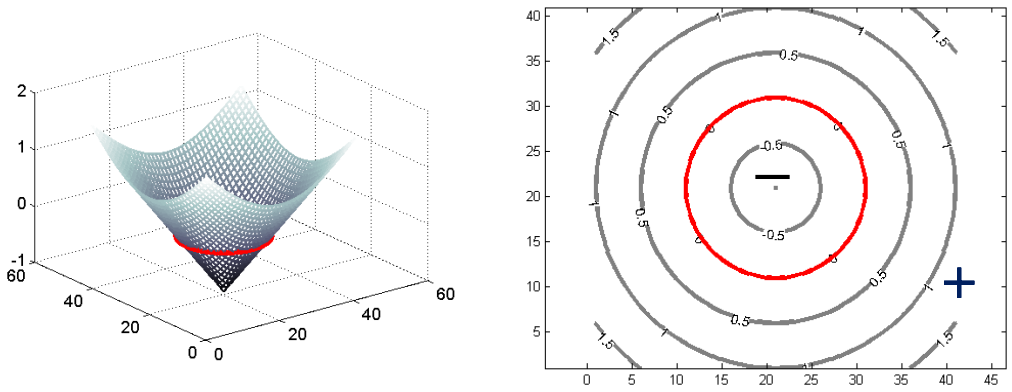

Figure 2-1 An example of (left) the level set function $f(x,y) = \sqrt{x^2+y^2} - 1$, and (right) the different cut-planes based on levels of z-constants as shown by numbers over the contours

Subsequently, if a target level differs from the current state, a speed function F will be required to propagate the contour in normal direction over an artificial time t. This traditional approach was presented by Osher and Sethian [21]. Let $\boldsymbol{x}(t)$ be a point on the propagating contour, and $\boldsymbol{x}(t=0)$ is a point on the initial contour. To evolve the level-set function with preserving the zero level-set function on a hypersurface, it needs $\phi(\boldsymbol{x}(t),t)=0$. By the chain rule,

$$\begin{aligned}\frac{\partial\phi(\boldsymbol{x}(t),t)}{\partial t}=\frac{\partial\phi}{\partial t}+\frac{\partial\phi}{\partial\boldsymbol{x}}\frac{\partial\boldsymbol{x}}{\partial t}&=\quad 0,\\ \phi_t+\nabla\phi(\boldsymbol{x}(t),t)\boldsymbol{x}'(t)&=\quad 0.\end{aligned}\tag{2.2}$$

Since $\hat{\mathbf{n}}=-\frac{\nabla\phi}{|\nabla\phi|}$ is an inward unit normal vector, the level-set evolution equation is

$$\phi_t-\hat{\mathbf{n}}|\nabla\phi|\boldsymbol{x}_t=\phi_t-F|\nabla\phi|=\quad 0,\tag{2.3}$$

Consequently, if the front moves inwards, the level-set evolution equation is given by

$$\begin{cases}\dfrac{\partial\phi}{\partial t}=F|\nabla\phi| & ;t\in(0,\infty)\text{ and }\boldsymbol{x}\in\mathbb{R}^2\\ \phi(\boldsymbol{x},t=0)=\phi_0(\boldsymbol{x}) & ;\boldsymbol{x}\in\mathbb{R}^2\end{cases}\tag{2.4}$$

where ϕ_0 is the initial zero level-set function, and the variable $\boldsymbol{x}$ is a position in a two dimensional space $\mathbb{R}^2$. Actually, the speed function F in Equation (2.4) can be described by the mean curvature κ [21] as

$$F=\kappa=\nabla\cdot\frac{\nabla\phi}{|\nabla\phi|}=\operatorname{div}\left(\frac{\nabla\phi}{|\nabla\phi|}\right),\tag{2.5}$$

where div(·) is a divergence operator. Thus, the level-set evolution equation is rewritten by

$$\begin{cases}\dfrac{\partial\phi}{\partial t}=\operatorname{div}\left(\dfrac{\nabla\phi}{|\nabla\phi|}\right)|\nabla\phi| & ;t\in(0,\infty)\text{ and }\boldsymbol{x}\in\mathbb{R}^2\\ \phi(\boldsymbol{x},t=0)=\phi_0(\boldsymbol{x}) & ;\boldsymbol{x}\in\mathbb{R}^2.\end{cases}\tag{2.6}$$

2.3 Level-set image segmentation with free re-initialization

Traditionally, the evolution of level-set function ϕ requires the re-initialization process to preserve numerical accuracy [22] because the evolution process may cause the level-set function to be flat. Thus, the traditional level-set image segmentation is performed as a diagram in Figure 2-2. First, the initialization process constructs the initial zero level-set function ϕ_0. Then, the given contour is propagated by the speed

function F. Next, the re-initialization is computed to regularize the level-set function for representing the signed distance function. Afterwards, a stop condition is checked to terminate the iteration process. If the stop condition is not satisfied, the level-set function will be sent backwards to the evolution process.

However, the re-initialization process consumes high computation cost. Many studies [23, 24, 25, 26] have been proposed to solve this problem. From the literature review, the distance regularized level-set evolution (DRLSE) [24] and the reaction diffusion (RD) [26] method demonstrated attractive results. Indeed, the DRLSE method has been referred in many studies [27, 28, 29], but this method may not perform well when the speed function or energy functional is a geodesic active contour [30] or an active contour without edge (Chan-Vese) [31] model as described in some results [26]. Therefore, this study chooses the reaction diffusion technique to remove the re-initialization process and preserve numerical accuracy. However, both DRLSE and RD methods are briefly explained in this section.

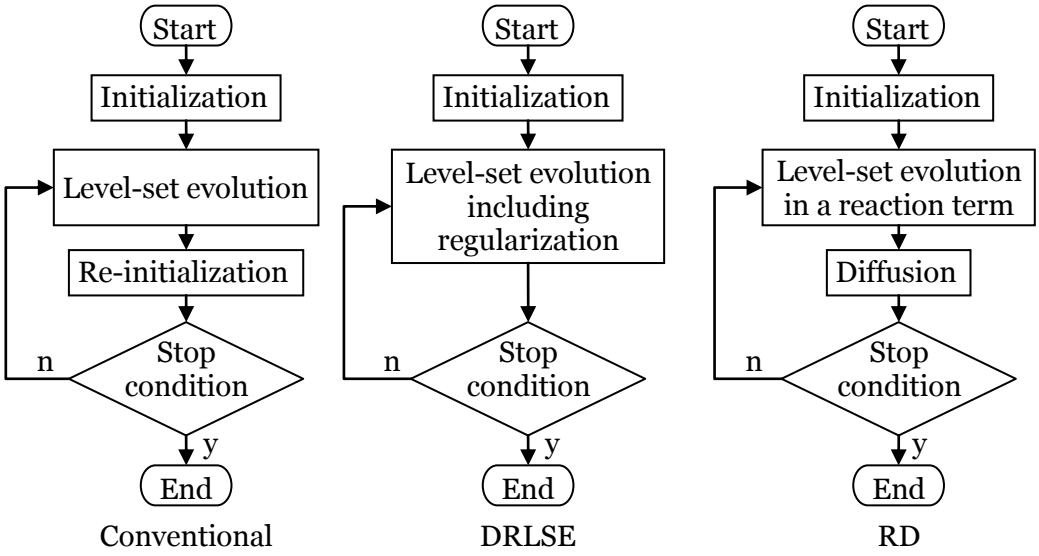

Figure 2-2 Three diagram of the level-set image segmentation based on conventional, DRLSE, and RD methods

2.3.1 Distance regularized level-set evolution (DRLSE)

From [24], a level-set function is defined by an energy-functional $\mathcal{E}(\phi)$ as

$$\mathcal{E}(\phi) = \mu R_p(\phi) + \mathcal{E}_{\text{ext}}(\phi). \tag{2.7}$$

$$R_p(\phi) \triangleq \int p(|\nabla\phi|)\, d\boldsymbol{x} \tag{2.8}$$

where $R_p(\phi)$ is the level-set regularization term formulated by a potential function $p(\cdot): [0, \infty) \rightarrow \mathbb{R}$, μ is a positive constant, and $\mathcal{E}_{\text{ext}}(\phi)$ denotes an external energy. This regularization term is aimed to achieve a minimum when the zero level-set function moves to a target location. The potential function is declared by $p(s) \triangleq 0.5 * (s-1)^2$; thus, the level-set regularization is expressed by

$$R_p(\phi) \triangleq \frac{1}{2} \int (|\nabla \phi| - 1)^2 \, d\boldsymbol{x}. \tag{2.9}$$

Next, to determine a level-set evolution (LSE) equation, the energy functional is minimized by using the Gâteaux derivative and the gradient flow equation [32] $\frac{\partial \phi}{\partial t} = -\frac{\partial \mathcal{E}}{\partial \phi}$. Therefore, the energy functional $\mathcal{E}(\phi)$ is transformed to

$$\frac{\partial \mathcal{E}}{\partial \phi} = \mu \frac{\partial R_p}{\partial \phi} + \frac{\partial \mathcal{E}_{\text{ext}}}{\partial \phi}, \tag{2.10}$$

and

$$\frac{\partial \phi}{\partial t} = -\mu \frac{\partial R_p}{\partial \phi} - \frac{\partial \mathcal{E}_{ext}}{\partial \phi}. \tag{2.11}$$

Then, referring to [24], the Gâteaux derivative is applied to $R_p(\phi)$ as shown in Equation (2.9) and it is given by

$$\frac{\partial R_p}{\partial \phi} = -\text{div}\big(d_p(|\nabla \phi|)\nabla \phi\big). \tag{2.12}$$

Thus, the Equation (2.11) is rewritten by

$$\frac{\partial \phi}{\partial t} = \mu \text{div}\big(d_p(|\nabla \phi|)\nabla \phi\big) - \frac{\partial \mathcal{E}_{ext}}{\partial \phi}, \tag{2.13}$$

From [24], $d_p(s) \triangleq \frac{p'(s)}{s} = \frac{(s-1)}{s}$, or $d_p(|\nabla \phi|) = \frac{|\nabla \phi| - 1}{|\nabla \phi|} = 1 - \frac{1}{|\nabla \phi|}$

$$\frac{\partial \phi}{\partial t} = \mu \text{div}\left(\nabla \phi - \frac{\nabla \phi}{|\nabla \phi|}\right) - \frac{\partial \mathcal{E}_{ext}}{\partial \phi}, \tag{2.14}$$

$$= \mu \underbrace{\left(\Delta \phi - \text{div}\left(\frac{\nabla \phi}{|\nabla \phi|}\right)\right)}_{\text{A Regularization term}} - \frac{\partial \mathcal{E}_{ext}}{\partial \phi}.$$

Consequently, the level-set function is propagated by the time-step t as follows.

$$\phi_{i+1} = \phi_i + t\left(\mu\left(\Delta \phi - \text{div}\left(\frac{\nabla \phi}{|\nabla \phi|}\right)\right) - \frac{\partial \mathcal{E}_{ext}}{\partial \phi}\right). \tag{2.15}$$

2.3.2 Reaction Diffusion (RD)

In [26], the reaction-diffusion equation in a two-dimension space for the level-set method is formulated by

$$\begin{cases} \dfrac{\partial \phi}{\partial t} = k\Delta\phi - \dfrac{1}{k}R(\phi) & ; t \in (0,\infty) \text{ and } \boldsymbol{x} \in \mathbb{R}^2, \\ \phi(\boldsymbol{x}, t=0) = \phi_0(x) & ; \boldsymbol{x} \in \mathbb{R}^2. \end{cases} \tag{2.16}$$

The $k\Delta\phi$ presents a diffusion term used to regularize the level-set function into a piecewise constant instead of a re-initialization process. Meanwhile, the reaction term $-\frac{1}{k}R(\phi)$ is used to control directions of the curve propagation. Subsequently, the level-set evolution is implemented by using a two-step splitting method modified from [33]. In summary, the reaction diffusion method contains three main steps. First, the initial zero level-set function ϕ_0 is constructed from an initial region R_0 and a positive constant c_0 as defined by

$$\phi_0(\boldsymbol{x}) = \begin{cases} -c_0 & ; \text{if } \boldsymbol{x} \in R_0, \\ c_0 & ; \text{otherwise.} \end{cases} \tag{2.17}$$

Second, the level-set evolution (LSE) equation $\mathcal{E}$ is defined to produce the reaction term for controlling directions of the curve propagation. This reaction term is

$$\phi_{R(i)} = \phi_i + k_{\mathrm{R}}\mathcal{E}, \tag{2.18}$$

where k_{R} is a constant that gives the reaction time-step. Then, its result is updated into the level-set function (LSF) in the diffusion term by

$$\phi_{i+1} = \phi_i + k_{\mathrm{D}}\Delta\left(\phi_{\mathrm{R}(i)}\right), \tag{2.19}$$

where k_{D} is a constant for diffusion time-step. Next, the updated result of the LSF is backwards sent to the second step for performing the iteration process. Further, this iteration process is terminated when a stop condition is satisfied.

2.4 GAC, CV, and Edge-based level-set methods

From literature review, geodesic active contour, active contour without edge (Chan-Vese), and edge based level-set models are often mentioned in image segmentation applications. These level-set models are briefly discussed in this section.

2.4.1 Geodesic active contour in the RD technique: RD-GAC

The energy functional of the geodesic active contour [30] is defined as the length as

$$L = \int_0^1 \mathrm{g}(C(q))\left|C_q(q)\right| dq, \tag{2.20}$$

where $\mathrm{g}(\cdot)$ is the edge detector of a parameterized planar curve $C(q)\colon [0,1] \to \mathbb{R}^2$ and $C_q(q) \equiv \frac{\partial C(q)}{\partial q}$. To determine the evolution equation, the energy function needs minimization. Let $C = C(q)$ and $C_q = C_q(q)$; thus the derivative of L with respect to t is computed by

$$\begin{aligned} \frac{\partial}{\partial t}L(C) &= \int_0^1 \left[\frac{d}{dt}\mathrm{g}(C)\right]\left|C_q\right| dq + \int_0^1 \mathrm{g}(C)\left[\frac{d}{dt}\left|C_q\right|\right] dq, \\ &= \int_0^1 [\nabla \mathrm{g}(C)\cdot C_t]\left|C_q\right| dq + \int_0^1 \mathrm{g}(C)\hat{T}\cdot C_{tq}\, dq, \end{aligned} \tag{2.21}$$

where $\hat{T}$ is a unit tangent to the curve C. Then, integration by parts is applied to the second term as

$$\begin{aligned} \frac{\partial}{\partial t}L(C) &= \int_0^1 [\nabla \mathrm{g}(C)\cdot C_t]\left|C_q\right| dq - \int_0^1 \left[\mathrm{g}(C)\cdot \hat{T}\right]_q C_t\, dq \\ &= \int_0^1 [\nabla \mathrm{g}(C)\cdot C_t]\left|C_q\right| dq - \int_0^1 \left[\nabla \mathrm{g}(C)\cdot C_q\hat{T}\right]\cdot C_t\, dq - \int_0^1 \left[\mathrm{g}(C)\hat{T}_q\right]\cdot C_t\, dq \\ &= \int_0^1 \left[[\nabla \mathrm{g}(C)\cdot C_t] - \left[(\nabla \mathrm{g}(C)\cdot C_s)\times\left(\hat{T}\cdot C_t\right)\right]\right]\left|C_q\right| dq - \int_0^1 \left[\mathrm{g}(C)\hat{T}_q\right]\cdot C_t\, dq, \end{aligned} \tag{2.22}$$

From $\left|C_q\right| dq = ds$ and $\hat{T}_s\left|C_q\right| = \hat{T}_q$then

$$\begin{aligned} \frac{\partial}{\partial t}L(C) &= \int_0^1 \left[[\nabla \mathrm{g}(C)\cdot C_t] - \left[(\nabla \mathrm{g}(C)\cdot C_s)\times\left(\hat{T}\cdot C_t\right)\right] - \mathrm{g}(C)\hat{T}_s\cdot C_t\right]\left|C_q\right| dq \\ &= \int_0^L \left[[\nabla \mathrm{g}(C)\cdot C_t] - \left[\left(\nabla \mathrm{g}(C)\cdot \hat{T}\right)\left(\hat{T}\cdot C_t\right)\right] - \mathrm{g}(C)\cdot \hat{T}_s\cdot C_t\right] ds \\ &= \int_0^L \left[\nabla \mathrm{g}(C) - \left(\nabla \mathrm{g}(C)\cdot \hat{T}\right)\hat{T} - \mathrm{g}(C)\hat{T}_s\right]\cdot C_t ds \end{aligned} \tag{2.23}$$

Since $\hat{T}_s = \kappa\hat{\mathbf{n}}$

$$\frac{\partial}{\partial t}L(C) = \int_0^L [\nabla \mathrm{g}(C) - (\nabla \mathrm{g}(C)\cdot \hat{\mathbf{n}})\hat{\mathbf{n}} - \mathrm{g}(C)\kappa\hat{\mathbf{n}}]\cdot C_t ds \tag{2.24}$$

Next, the steepest descent method is applied to connect an initial curve C_0 with a minimum length of $L(C)$. The evolution equation is given by

$$\frac{\partial C}{\partial t} = \mathrm{g}(C)\kappa\hat{\mathbf{n}} - (\nabla \mathrm{g}(C) \cdot \hat{\mathbf{n}})\hat{\mathbf{n}}. \tag{2.25}$$

It should be rewritten in a level-set form [34, 35] as

$$\frac{\partial \phi}{\partial t} = \underbrace{\left(\mathrm{div}\left(\mathrm{g}\frac{\nabla\phi}{|\nabla\phi|}\right) + v\mathrm{g}\right)}_{\text{Speed function}} |\nabla\phi|, \tag{2.26}$$

$$\mathrm{g}(I) = \frac{1}{1 + |\nabla(G_\sigma * I)|^2}, \tag{2.27}$$

where $\mathrm{g}(\cdot)$ is an edge detector function used in a given image I. The variable G_σ is a Gaussian function with a standard deviation σ. The variable v is a constant. Further, this level-set evolution equation can be directly integrated into Equation (2.18) in the RD technique as

$$\phi_{R(i)} = \phi_i + k_{\mathrm{R}}\left(|\nabla\phi|\left(\mathrm{div}\left(\mathrm{g}\frac{\nabla\phi}{|\nabla\phi|}\right) + v\mathrm{g}\right)\right), \tag{2.28}$$

and the curve propagation of the level-set function is

$$\phi_{i+1} = \phi_i + k_{\mathrm{D}}\Delta\left(\phi_i + k_{\mathrm{R}}\left(|\nabla\phi|\left(\mathrm{div}\left(\mathrm{g}\frac{\nabla\phi}{|\nabla\phi|}\right) + v\mathrm{g}\right)\right)\right). \tag{2.29}$$

2.4.2 A Chan-Vese model in the RD technique: RD-CV

The Chan-Vese (CV) [31] model considers an energy-functional instead of the speed function of the given contour, which is based on the gradient of the level-set function $|\nabla\phi|$ as Equation (2.4). The energy functional of the CV model $\mathcal{E}^{CV}$ is a combination of length, area, and the global gray-intensity fitting terms, and it is formulated by

$$\begin{aligned}
&\mathcal{E}^{CV}(c_1, c_2, \phi) \qquad (2.30)\\
&= \underbrace{\mu \int_\Omega \delta_\varepsilon(\phi(\boldsymbol{x}))|\nabla\phi(\boldsymbol{x})|d\boldsymbol{x}}_{\text{length}} + \underbrace{\nu \int_\Omega H_\varepsilon(\phi(\boldsymbol{x}))d\boldsymbol{x}}_{\text{area}}\\
&+ \underbrace{\lambda_1 \int_\Omega |I(\boldsymbol{x}) - c_1|^2 H_\varepsilon(\phi(\boldsymbol{x}))d\boldsymbol{x} + \lambda_2 \int_\Omega |I(\boldsymbol{x}) - c_2|^2 \left(1 - H_\varepsilon(\phi(\boldsymbol{x}))\right)d\boldsymbol{x}}_{\text{global gray-intensity fitting}},
\end{aligned}$$

$$c_1(\phi) = \frac{\int_\Omega I(\boldsymbol{x}) H_\varepsilon\big(\phi(\boldsymbol{x})\big) d\boldsymbol{x}}{\int_\Omega H_\varepsilon\big(\phi(\boldsymbol{x})\big) d\boldsymbol{x}}, \tag{2.31}$$

$$c_2(\phi) = \frac{\int_\Omega I(\boldsymbol{x}) \Big(1 - H_\varepsilon\big(\phi(\boldsymbol{x})\big)\Big) d\boldsymbol{x}}{\int_\Omega \Big(1 - H_\varepsilon\big(\phi(\boldsymbol{x})\big)\Big) d\boldsymbol{x}}, \tag{2.32}$$

$$H_\varepsilon(z) = \frac{1}{2}\left(1 + \frac{2}{\pi}\arctan\left(\frac{z}{\varepsilon}\right)\right), \tag{2.33}$$

$$\delta_\varepsilon(z) = \frac{1}{\pi}\frac{\varepsilon^2}{\varepsilon^2 + z^2}, \tag{2.34}$$

where c_1 and c_2 are equivalent to mean-intensities of regions inside and outside the given contour, respectively. The $H_\varepsilon(\cdot)$ is the Heaviside function, and $\delta_\varepsilon(\cdot)$ is the Dirac delta function where the variable ε denotes the width of the Dirac delta function. Further, the variables μ, ν, λ_1, and λ_2 are constants. Then, the level-set evolution equation is determined by minimizing the energy functional $\mathcal{E}^{CV}$.

In order to minimize this energy function $\mathcal{E}^{CV}$, weak differential (Gâteaux derivative) is applied to each term. The definition of the weak differential is

$$DF(\phi;\psi) = \lim_{t\to 0}\frac{F(\phi + t\psi) - F(\phi)}{t} = \frac{d}{dt}F(\phi + t\psi)|_{t=0}. \tag{2.35}$$

First, the length term $\mathcal{L}(\phi)$ is considered as

$$\mathcal{L}(\phi) = \int_\Omega \delta_\varepsilon\big(\phi(\boldsymbol{x})\big)|\nabla\phi(\boldsymbol{x})| d\boldsymbol{x} \tag{2.36}$$

$$D\mathcal{L}(\phi;\psi) = \lim_{t\to 0}\frac{\int_\Omega \delta_\varepsilon(\phi + t\psi)|\nabla(\phi + t\psi)|\, d\boldsymbol{x} - \int_\Omega \delta_\varepsilon(\phi)|\nabla\phi|\, d\boldsymbol{x}}{t} \tag{2.37}$$

$$= \int_\Omega \frac{d}{dt}\delta_\varepsilon(\phi + t\psi)|\nabla(\phi + t\psi)|\Big|_{t=0} d\boldsymbol{x}$$

From differential rule $\frac{d}{dt}[u(t)\cdot v(t)] = u'(t)\cdot v(t) + u(t)\cdot v'(t)$ and the linearity of gradient $\nabla(f+g) = \nabla f + \nabla g$,

$$D\mathcal{L}(\phi;\psi) = \int_{\Omega}\left(\frac{d}{dt}\delta_{\varepsilon}(\phi+t\psi)\right)|\nabla(\phi+t\psi)| \tag{2.38}$$

$$+\delta_{\varepsilon}(\phi+t\psi)\frac{d}{dt}|\nabla(\phi+t\psi)|\Big|_{t=0} d\boldsymbol{x}$$

$$= \int_{\Omega} \delta'_{\varepsilon}(\phi+t\psi)\psi|\nabla(\phi+t\psi)| + \delta_{\varepsilon}(\phi+t\psi)\nabla\psi\frac{\nabla(\phi+t\psi)}{|\nabla(\phi+t\psi)|}\Big|_{t=0} d\boldsymbol{x}$$

$$= \int_{\Omega} \delta'_{\varepsilon}(\phi)|\nabla\phi|\cdot\psi + \delta_{\varepsilon}(\phi)\frac{\nabla\phi}{|\nabla\phi|}\cdot\nabla\psi d\boldsymbol{x}$$

Let $\delta_{\varepsilon}(\phi)\frac{\nabla\phi}{|\nabla\phi|} = A$, $\nabla\phi\hat{\mathbf{n}} = \frac{\partial\phi}{\partial\hat{\mathbf{n}}}$, and the Greens theorem is applied to the second term as

$$\int_{\Omega} A\nabla\psi d\boldsymbol{x} = \int_{\partial\Omega}\psi A\hat{\mathbf{n}}dS - \int_{\Omega}\psi\nabla\mathrm{A}d\boldsymbol{x}, \tag{2.39}$$

$$= \int_{\partial\Omega}\psi\left(\frac{\delta_{\varepsilon}(\phi)}{|\nabla\phi|}\frac{\partial\phi}{\partial\hat{\mathbf{n}}}\right)dS - \int_{\Omega}\psi\cdot\nabla\left(\delta_{\varepsilon}(\phi)\frac{\nabla\phi}{|\nabla\phi|}\right)d\boldsymbol{x},$$

When the second term is substituted to the differentiation of $\mathcal{L}(\phi;\psi)$,

$$D\mathcal{L}(\phi;\psi) = \int_{\Omega}\delta'_{\varepsilon}(\phi)|\nabla\phi|\cdot\psi\,, d\boldsymbol{x} \tag{2.40}$$

$$+\int_{\partial\Omega}\psi\left(\frac{\delta_{\varepsilon}(\phi)}{|\nabla\phi|}\frac{\partial\phi}{\partial\hat{\mathbf{n}}}\right)dS - \int_{\Omega}\psi\cdot\nabla\left(\delta_{\varepsilon}(\phi)\frac{\nabla\phi}{|\nabla\phi|}\right)d\boldsymbol{x}$$

$$= \int_{\Omega}\left(\delta'_{\varepsilon}(\phi)|\nabla\phi| - \nabla\left(\delta_{\varepsilon}(\phi)\frac{\nabla\phi}{|\nabla\phi|}\right)\right)\psi d\boldsymbol{x} + \int_{\partial\Omega}\psi\left(\frac{\delta_{\varepsilon}(\phi)}{|\nabla\phi|}\frac{\partial\phi}{\partial\hat{\mathbf{n}}}\right)dS.$$

Since $\frac{\delta_{\varepsilon}(\phi)}{|\nabla\phi|}\frac{\partial\phi}{\partial\hat{\mathbf{n}}} = 0$ on the curve evolution domain,

$$D\mathcal{L}(\phi;\psi) = \int_{\Omega}\left(\delta'_{\varepsilon}(\phi)|\nabla\phi| - \delta'_{\varepsilon}(\phi)\frac{\nabla\phi}{|\nabla\phi|} - \delta_{\varepsilon}(\phi)\left(\nabla\cdot\frac{\nabla\phi}{|\nabla\phi|}\right)\right)\psi d\boldsymbol{x}. \tag{2.41}$$

$$= \int_{\Omega}\left(-\delta_{\varepsilon}(\phi)\left(\nabla\cdot\frac{\nabla\phi}{|\nabla\phi|}\right)\right)\psi d\boldsymbol{x}.$$

Second, the area term is $\mathcal{A}(\phi) = \int_{\Omega} H_{\varepsilon}(\phi(\boldsymbol{x}))d\boldsymbol{x}$, and its weak differential is formulated by

$$D\mathcal{A}(\phi;\psi) = \lim_{t\to 0}\int_{\Omega}\frac{H_{\varepsilon}(\phi+t\psi)-H_{\varepsilon}(\phi)}{t}d\mathbf{x} = \int_{\Omega}\frac{d}{dt}H_{\varepsilon}(\phi+t\psi)\Big|_{t=0}d\mathbf{x}, \tag{2.42}$$

$$= \int_{\Omega}\delta_{\varepsilon}(\phi)\psi d\mathbf{x}.$$

Third, the weak differential of the global intensity fitting term is similarly determined, and it finally presents

$$D\mathcal{F}(\phi;\psi) = \int_{\Omega}|I-c_1|^2\cdot\delta_{\varepsilon}(\phi)\psi d\mathbf{x} - \int_{\Omega}|I-c_2|^2\cdot(\delta_{\varepsilon}(\phi)\psi)d\mathbf{x}. \tag{2.43}$$

Consequently, from $\frac{\partial\phi}{\partial t} = -\frac{\partial\mathcal{E}}{\partial\phi}$ and $\mathrm{div}(F) = \nabla\cdot\mathrm{F}$, the level-set evolution equation of the CV model is

$$\frac{\partial\phi}{\partial t} = \delta_{\varepsilon}(\phi)\left(\mu\mathrm{div}\left(\frac{\nabla\phi}{|\nabla\phi|}\right) - v - \lambda_1(I-c_1)^2 + \lambda_2(I-c_2)^2\right), \tag{2.44}$$

where $t\in(0,\infty)$ and $\boldsymbol{x}\in\mathbb{R}^2$, and $\phi(\boldsymbol{x},t=0) = \phi_0(\boldsymbol{x})$. Moreover, in this study, this level-set evolution equation is directly applied to the reaction term (Equation (2.18)) for controlling directions of the curve propagation as

$$\phi_{R(i)} = \phi_i + k_{\mathrm{R}}\left(\delta_{\varepsilon}(\phi)\left(\mu\mathrm{div}\left(\frac{\nabla\phi}{|\nabla\phi|}\right) - v - \lambda_1(I-c_1)^2 + \lambda_2(I-c_2)^2\right)\right). \tag{2.45}$$

Consequently, the level-set function is propagated by

$$\phi_{i+1} = \phi_i + \tag{2.46}$$

$$k_{\mathrm{D}}\Delta\left(\phi_i + k_{\mathrm{R}}\left(\delta_\varepsilon(\phi)\left(\mu\mathrm{div}\left(\frac{\nabla\phi}{|\nabla\phi|}\right) - v - \lambda_1(I-c_1)^2 + \lambda_2(I-c_2)^2\right)\right)\right).$$

2.4.3 An edge-based level-set method in the DRLSE technique: DRLSE-E

In this section, the edge-based level-set method in the DRLSE technique [24] is referred. It starts from defining the external energy functional as a combination of length and area terms in Equation (2.7).

$$\mathcal{E}(\phi) = \mu R_p(\phi) + \underbrace{\lambda\mathcal{L}(\phi)}_{\text{length}} + \underbrace{v\mathcal{A}(\phi)}_{\text{area}}. \tag{2.47}$$

$$\mathcal{L}(\phi) \triangleq \int_\Omega \mathrm{g}\delta_\varepsilon\big(\phi(\boldsymbol{x})\big)|\nabla\phi(\boldsymbol{x})|d\boldsymbol{x}, \tag{2.48}$$

$$\mathcal{A}(\phi) \triangleq \int_\Omega \mathrm{g}H_\varepsilon\big(\phi(\boldsymbol{x})\big)d\boldsymbol{x} \tag{2.49}$$

$$\mathrm{g}(I) = \frac{1}{1+|\nabla(G_\sigma * I)|^2} \tag{2.50}$$

$$H_\varepsilon(\boldsymbol{x}) = \begin{cases} \frac{1}{2}\left(1+\frac{\boldsymbol{x}}{\varepsilon}+\frac{1}{\pi}\sin\left(\frac{\pi\boldsymbol{x}}{\varepsilon}\right)\right), & \text{if } |\boldsymbol{x}| \le \varepsilon \\ 1, & \text{if } \boldsymbol{x} > +\varepsilon \\ 0, & \text{if } \boldsymbol{x} < -\varepsilon \end{cases} \tag{2.51}$$

$$\delta_\varepsilon(\boldsymbol{x}) = \begin{cases} \frac{1}{2\varepsilon}\left(1+\cos\left(\frac{\pi\boldsymbol{x}}{\varepsilon}\right)\right), & \text{if } |\boldsymbol{x}| \le \varepsilon \\ 0, & \text{if } |\boldsymbol{x}| > \varepsilon \end{cases} \tag{2.52}$$

where $\mathrm{g}(\cdot)$ is an edge detector function as it is defined in the GAC model, and the variable I denotes a given image. The variables μ, λ, and α are constants. To obtain the level-set evolution equation, the energy functional in each term is minimized by applying the weak differential as explained in the Chan-Vese model section 2.4.2. Then, the curve evolution of the level-set function is formulated by

$$\phi_{i+1} = \phi_i + t\left(\mu\left(\Delta\phi - \mathrm{div}\left(\frac{\nabla\phi}{|\nabla\phi|}\right)\right) + \delta_\varepsilon(\phi)\left(\lambda \mathrm{div}\left(\mathrm{g}\frac{\nabla\phi}{|\nabla\phi|}\right) + v\mathrm{g}\right)\right). \quad (2.53)$$

where t is an artificial time-step.

2.5 Summary

Level-set image segmentation generally starts from constructing the initial zero level-set function. Then, the level-set evolution equation is defined to control directions of the curve moving. Further, a re-initialization process is traditionally required to preserve numerical accuracy after performing much iteration. However, the re-initialization process consumes high computation cost. Thus, a reaction-diffusion (RD) evolution technique is preferred to remove the re-initialization process and keep accuracy. Afterwards, the stop condition is used to terminate the iteration process.

To control the curve moving, RD-GAC, RD-CV, and DRLSE-E methods are considered and summarized in this study. Actually, the GAC and CV denote the geodesic active contour and Chan-Vese, respectively. Further, the DRLSE-E method is the integration of the distance regularization level-set evolution and edge-based level-set model.

Both the RD-GAC and DRLSE-E require gradient information from a given image to control the curve propagation. However, the propagation of the RD-GAC model is dominated by the gradient magnitude of the level-set function. On the other hand, the DRLSE-E model uses the Dirac delta function to manage the curve propagation. Further, it is possible to control the smoothness of the curve evolution by adjusting the coefficient of the curvature term in the DRLSE-E model.

Furthermore, the RD-CV model considers the global variation of gray-intensities between inside and outside the curve. Thus, the curve evolution of the RD-CV is not dependent on gradient information.

Chapter 3
An Image Segmentation System for 3D CT Liver-images

3.1 Introduction

This chapter explains details of the proposed liver-image segmentation system. This system is aimed to segment a liver volume from CT images. Section 3.2 describes an overview of the process. Section 3.3 discusses about the construction of the specific image representations. Section 3.4 introduces a concept of multi-resolutions used in the curve evolution. Section 3.5 presents the generation of initial zero level-set functions. Section 3.6 explains prevention of leakage regions outside ribs. Section 3.7 describes the modification of Chan-Vese model, which is used to control directions of the curve propagation. Section 3.8 explains a refinement step.

3.2 An Overview of the 3D CT liver-image segmentation system

This study presents an efficient system of liver-image segmentation. It performs under a concept of the level-set image segmentation.

The proposed system contains three main modules. First, construction of specific image representations is introduced. This module is used to generate two alternative types of image representations. One is an edge-based image referred as a seed-region-growing image [36]. The other is a confident region image proposed in this study. Moreover, the latter is constructed from a new technique called multilevel edge detections. However, this module will be ignored if gray-intensity image type is considered as an image input.

The second module is a level-set image segmentation process. This process is implemented by a multi-resolution technique. It requires two main operations including initialization and level-set evolution. The initialization is required to construct initial zero-level-set function and define the mask regions inside ribs. Actually, the mask regions are created to prevent leakage regions outside ribs after a given curve is moved. The level-set evolution controls the curve propagation that is dependent on the type of level-set evolution equations, such as geodesic active contour (GAC), edge, and Chan-Vese models.

In the last module, segmentation results are refined. An overview diagram of the proposed liver-image segmentation system is illustrated in Figure 3-1.

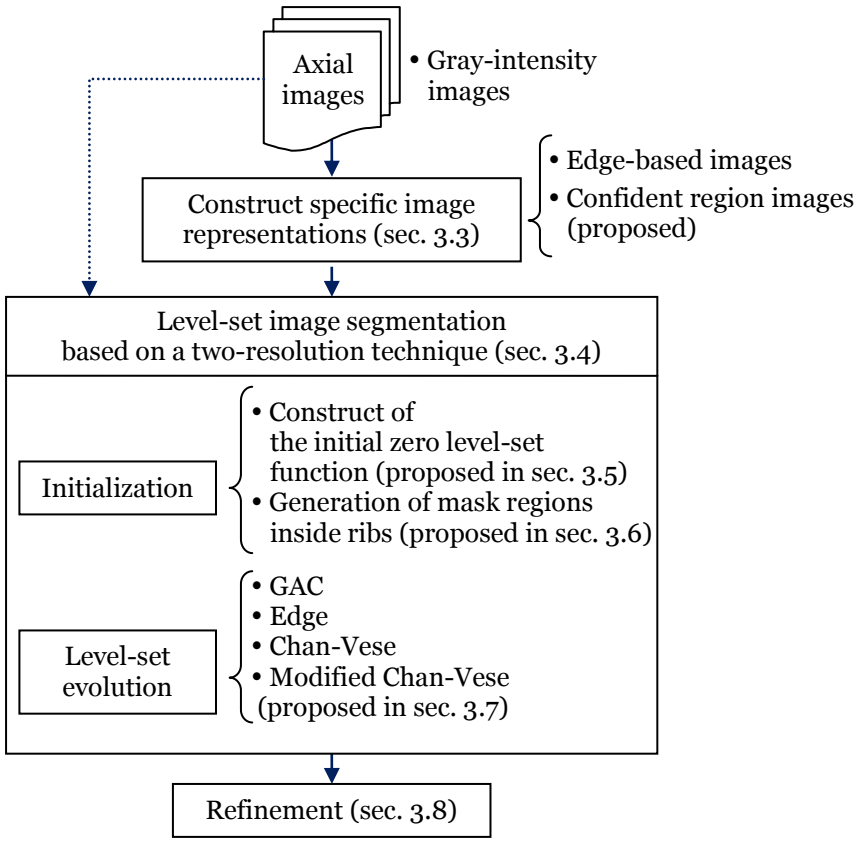

Figure 3-1 An overview of the 3D CT liver-image segmentation system based on a level-set method

3.3 Construction of the specific image representations

Many algorithms have been proposed in sophisticated formulas. Some algorithms add an extra term into a conventional method. These algorithms probably provide good segmentation results after they are applied to a typical gray-intensity image. However, they often consume high computation cost or may be limited by some requirements such as a large number of training data sets.

Alternatively, it is possible to improve the quality of segmentation results by constructing good image representation for describing the region of interest. For example, the seed region growing images [36] are produced to present the regions of interest in edge-based images. Indeed, this idea conveys the motivation to this study. This study proposes confident region images that are generated from a combination of multi-levels of gradient information. Meanwhile, the region of interest is described as a homogeneous region.

3.3.1 Edge-based image representation

This image type starts from generating the speed images (SI) [36]. First, it requires an image filter to reduce a level of image noise. In some cases, an advanced filter like a modified curvature diffusion filter [37] is required to reduce image noise and preserving edge information. Next, a sigmoid function is applied to extract edge information.

$$\mathrm{SI}(\boldsymbol{x}) = \frac{1}{1 + \exp\left(-\frac{|\nabla I(\boldsymbol{x})| - \beta}{\alpha}\right)} \tag{3.1}$$

where $I(\boldsymbol{x})$ is a given image and $\boldsymbol{x}$ is a pixel coordinate. The parameter β and α present the center and the width of the sigmoid function, respectively. This speed image is aimed to present homogenous regions towards one and boundary regions near zero. Then, each speed image is inverted by thresholding to construct a seed region growing (SRG) image as shown in Equation (3.2). The seed-region growing image represents homogeneous regions as zero and boundaries of anatomical structures as one.

$$\mathrm{SRG}(\boldsymbol{x}) = \begin{cases} 1 & \text{if } \mathrm{SI}(\boldsymbol{x}) \le T_1, \\ 0 & \text{otherwise,} \end{cases} \tag{3.2}$$

where T_1 is a threshold level. Therefore, this SRG image is considered as an edge-based image representation (see Figure 3-2).

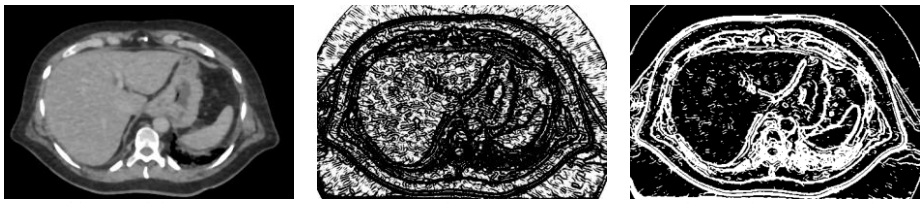

Filtered image | Speed Image (SI) | Seed Region Growing (SRG)

Figure 3-2 An example of filtered image, speed image (SI), and seed region growing (SRG) image [38]

Although the seed region-growing (SRG) image presents an attractive edge-image, some dirty edges appear inside the homogeneous regions. In fact, it is difficult to get clear regions from using only one level of thresholding when a given image includes a high level of image noise. If a threshold value is very small, boundaries of anatomical structures will be opened.

3.3.2 Confident region image representation

This study proposes a confident region image (CRI). It determines good boundaries of anatomical structures from using a combination of edge detector functions. Then, the result of this combination is used to describe the region of interest as a homogeneous region.

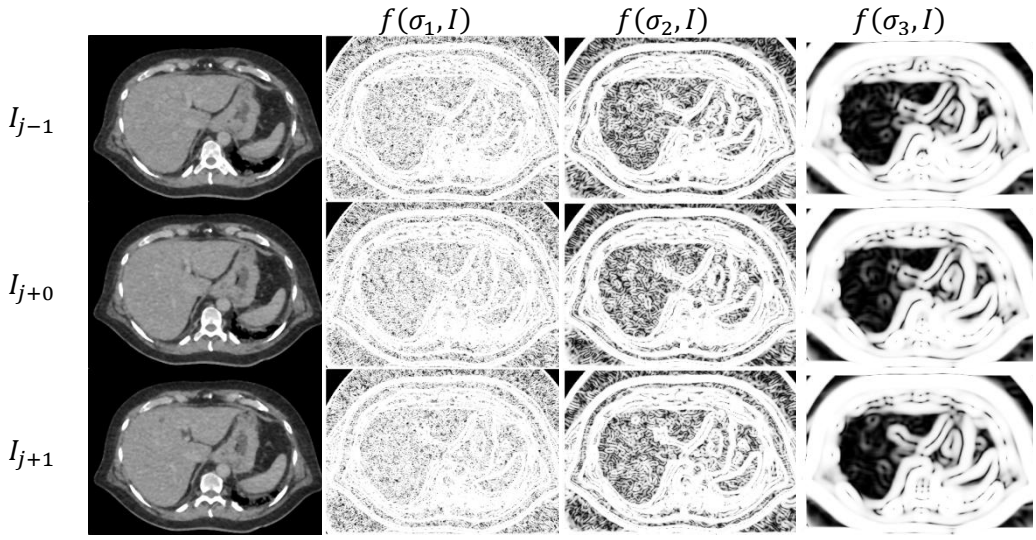

Figure 3-3 An example of three levels of edge detectors ($\sigma_1 = 0.5, \sigma_2 = 2.0$, and $\sigma_3 = 6.5$) on a given image I_j and its neighbors I_{j-1} and I_{j+1}.

This idea comes from an empirical study (see Figure 3-3). The result of edge detector function presents many details of edge information when a 3x3 Gaussian window with standard deviation $\sigma = 0.5$ is applied. However, image noises also contribute edge information into the result. Meanwhile, a 27x27 Gaussian window with standard deviation $\sigma = 6.5$ mostly illustrates a region including large variation on gray-intensities. Conversely, some details of anatomical structures are disappeared. In addition, anatomical structures in 3D-CT images are presented in consecutive image cut-planes. Further, some information of anatomical structures may be distorted due to high levels of image noises and artifacts. Consequently, this study presents an idea to combine edge information from multilevel edge detectors and three consecutive image slices. This combination is aimed to reduce unclear boundary as shown by F_{COM} in Figure 3-4.

This study formulates the edge detector function $f(\sigma, I)$ in an exponential form as given by

$$f(\sigma, I) = \exp\left(-\frac{1}{1 + |\nabla G_\sigma * I|^2}\right), \tag{3.3}$$

where σ is a standard deviation of a Gaussian window that is convolved with a given image I. This edge detector function presents pixels beside boundaries of anatomical structures towards one. Otherwise, pixel values are gradually reduced to near zero. Next, 3x3, 9x9, and 27x27 Gaussian windows with standard deviations $\sigma_1 = 0.5$, $\sigma_2 = 2.0$, and σ_3=6.5, are applied to a given image and its neighbors. Let a standard deviation be indexed by i, and the index of a given image slice be j. Therefore, the combination function F_{COM} is determined by

$$F_{\mathrm{COM}} = \prod_{i=\{1,2,3\},m=\{j-1,j,j+1\}} f(\sigma_i, I_m), \tag{3.4}$$

or

$$= \exp\left(- \sum_{m=j-1}^{j+1} \sum_{i=1}^{3} \left(\frac{1}{1 + \left| \nabla G_{\sigma_i} * I_m \right|^2} \right) \right).$$

Then, the result of F_{COM} is transformed to a binary image for presenting homogeneous regions and clear edges. This transformation is achieved by giving a threshold level T_2 of edge responses and it is called the confident map function (CMF) as

$$\mathrm{CMF}(\boldsymbol{x}) = \begin{cases} 1 & \text{if } F_{\mathrm{COM}}(\boldsymbol{x}) > T_2 \text{ , } T_2 \in (0,1], \\ 0 & \text{otherwise.} \end{cases} \tag{3.5}$$

Subsequently, the object of interest is selected from binary regions in the result of CMF. This selection is performed by using the connected component labeling method. If the selected binary-region is denoted by L, the confident region image (CRI) will be given by

$$\mathrm{CRI}(\boldsymbol{x}) = \begin{cases} \mu & \text{if } \boldsymbol{x} \in L, \\ I(\boldsymbol{x}) & \text{otherwise,} \end{cases} \tag{3.6}$$

where μ is a mean of gray-intensities of a given image $I(\boldsymbol{x})$ inside the labeled region $L(\boldsymbol{x})$ whereas the variable $\boldsymbol{x}$ denotes a pixel coordinate.

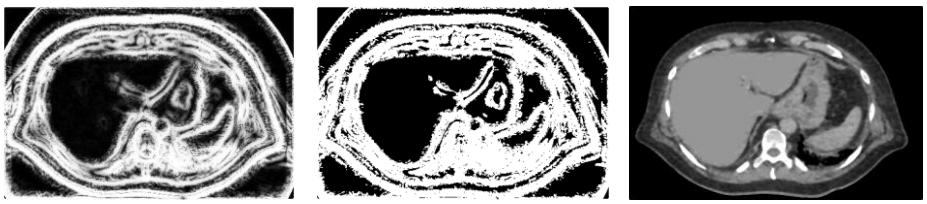

F_{COM} CMF CRI

Figure 3-4 An example of a combination of multilevel edge detectors (F_{COM}), a confident map function (CMF), and a confident region image (CRI).

3.4 Level-set image segmentation based on a two-resolution technique

This study proposes a two-resolution level-set image segmentation approach (see Figure 3-5). This approach contains two main steps. The first step performs the level-set image segmentation at the low resolution. Subsequently, the second step computes the level-set image segmentation at the original resolution.

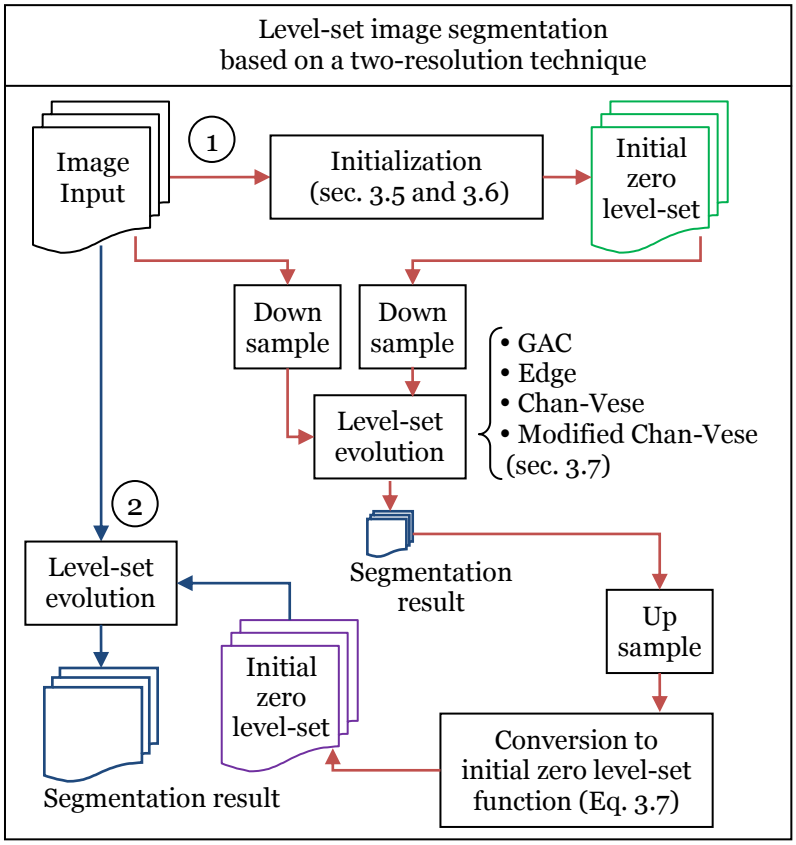

Figure 3-5 A diagram of level-set image segmentation using a two-resolution technique

This approach starts from the initialization process. An image input represents one of gray-intensity, edge, and confident region images. The image input is used to construct the initial zero level-set function. Then, the level-set function and all relate spaces are down sampling into 25 percent of the original image resolution. These relate spaces are dependent on the level-set evolution equation. For example, the proposed level-set model requires gray-intensities from an image input. Thus, the initial zero level-set function ϕ_0 and the image input are down sampled. Afterwards, the level-set evolution is performed.

Next, the segmentation region at the low resolution is up sampled to the original resolution. This up-sampled region is denoted by R_{b}. Moreover, it is used to construct the initial zero level-set function for the second computation of the level-set evolution process. It is given by

$$\phi_0(\boldsymbol{x}) = \begin{cases} -c_0 & ;\text{if } \boldsymbol{x} \in R_{\mathrm{b}}, \\ c_0 & ;\text{otherwise.} \end{cases} \tag{3.7}$$

where c_0 is a constant. Then, the level-set evolution process is repeated to get the final segmentation result at the original resolution.

Actually, the proposed two-resolution approach shows two advantages. First, it helps to adjust parameters. Indeed, the level-set image segmentation at the low resolution consumes computation cost less than the high resolution. Second, it is possible to reduce the number of iterations when the higher resolution is computed. The reason is that the result at low-resolution shows an approximate region near to the boundary of the object of interest.

3.5 Construction of initial zero level-set function (LSF)

This study generates the initial zero level-set function ϕ_0 from a binary region R_0 and a positive constant c_0, this generation is defined by

$$\phi_0(\boldsymbol{x}) = \begin{cases} -c_0 & \text{if } \boldsymbol{x} \in R_0, \\ c_0 & \text{otherwise.} \end{cases} \tag{3.8}$$

Indeed, the boundary of the binary region R_0 is equivalent to the boundary of the initial zero level-set function. If the binary region gives a contour near a boundary of the object of interest, it is possible to reduce the number of iterations and affect the accuracy of segmentation result.

For example, if the geodesic active contour (GAC) [30] is applied to the SRG image and a boundary of initial zero level-set function is far from the region of interest, propagation of the given curve will be prematurely stopped as demonstrated in Figure 3-6.

Consequently, this study proposes two methods to generate the initial zero level-set function. The first method is considered when a given image is represented by gray-intensities. Meanwhile, the second method is selected when an image input is the SRG (section 3.3.1) or CMF (section 3.3.2) image.

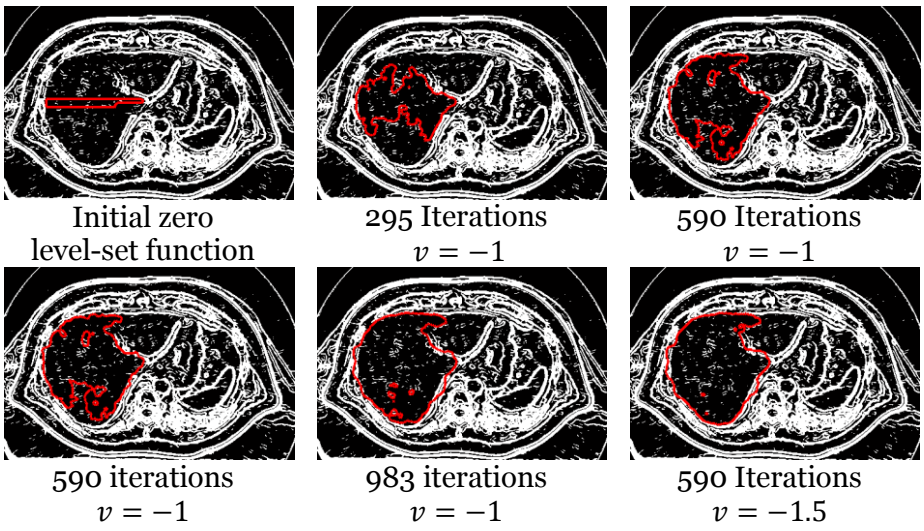

Figure 3-6 Five examples of segmentation results (red contours) when initial zero level-set is far from the region of interest and the curve is propagated by using the GAC model, $\boldsymbol{\phi_t = \left(\mathrm{div}\left(g\frac{\nabla\phi}{|\nabla\phi|}\right) + vg\right)|\nabla\phi|}$ where v is a constant.

3.5.1 Generation of initial zero LSF in gray-intensity images

The main idea is to obtain a region that presents a statistical distribution model of gray-intensities as same as a seed region. Indeed, mean μ_{seed} and standard deviation σ_{seed} are measured from a seed region allocated inside the object of interest in a given image I. Then, the initial region R_0 for creating the initial zero LSF ϕ_0 (Equation (3.8)) is obtained by

$$R_0(\boldsymbol{x}) = \begin{cases} 1 & \text{if } I(\boldsymbol{x}) \in \{\mu_{\text{seed}} \pm \sigma_{\text{seed}}\}, \\ 0 & \text{otherwise,} \end{cases} \tag{3.9}$$

where $\boldsymbol{x}$ is a pixel coordinate in an axial-image.

From a diagram in Figure 3-7, this study utilizes the coronal images to assist the construction of the seed regions of approximate liver-regions in axial-image planes. Actually, the coronal image visualizes anatomical image in the front-to-back direction. This image plane is perpendicular to the axial image plane that displays anatomical image in a head-to-foot direction. In this study, from preliminary experiment, the number of coronal image slices should be sampled at least 20 image slices for giving good seed regions inside axial image planes.

After coronal images are sampled around the center of a given 3D-CT volume, approximate liver-regions in these coronal images are obtained. In each coronal image I_c, it begins with some random rectangular patches. Indeed, these random patches are utilized to obtain an average of approximate liver-regions. Furthermore, these patches should be allocated on the left side of the considered image in

accordance with a physical location of the liver. Then, each patch is used to measure mean μ_{patch} and standard deviation σ_{patch} of gray-intensities. Next, the binary region R_c is extracted by thresholding as

$$R_c(\boldsymbol{y}) = \begin{cases} 1 & \text{if } I_c(\boldsymbol{y}) \in \{\mu_{\text{patch}} \pm \sigma_{\text{patch}}\}, \\ 0 & \text{otherwise,} \end{cases} \tag{3.10}$$

where $\boldsymbol{y}$ is a pixel coordinate in each coronal-image.

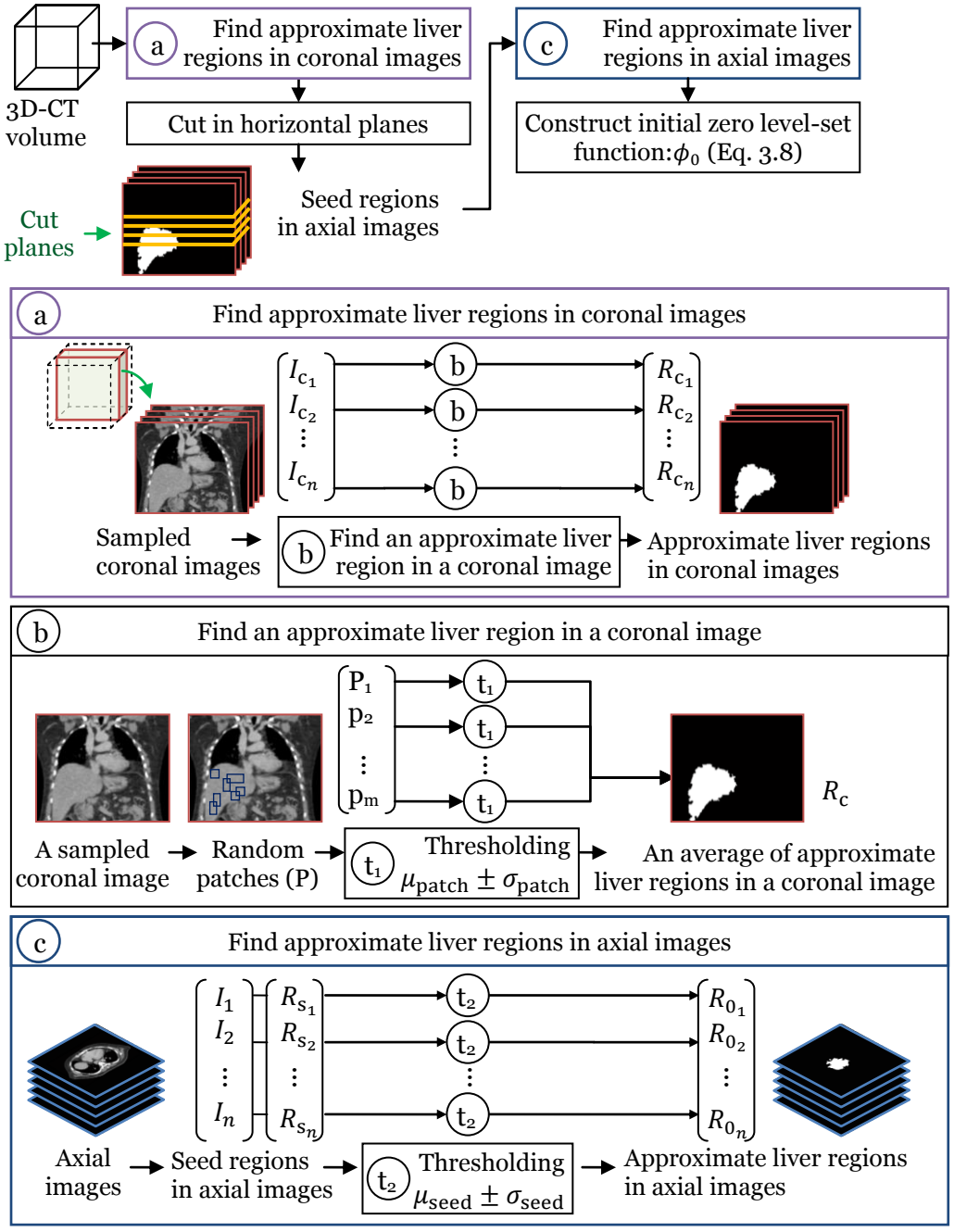

Figure 3-7 A diagram of the construction of initial zero level-set function in each gray-intensity image

Afterwards, this binary region is refined by the morphological operations [39] , such as hole filling, opening, and erosion. Next, the connected component labeling technique is applied to select the approximate liver region.

This selection considers three properties. First, a range of gray-intensities of liver is in a soft-tissue type (see standard CT numbers in section 4.2.1). Second, the liver region mostly locates on the left side of the coronal image. Third, the liver regions present the largest area if coronal images are sampled around the center of a 3D CT volume.

After all patches are applied to the considered coronal-image, it is possible to obtain an average of approximate liver regions. Similarly, averages of approximate liver-regions in the other coronal images can be determined.

Subsequently, the approximate liver regions of all sampled coronal images are cut in the horizontal planes to generate seed regions R_s in axial-image planes. Then, these seed-regions are used to measure mean μ_{seed} and standard deviation σ_{seed} for thresholding in Equation (3.9). The results of thresholding represent approximate liver regions R_0 in axial image planes. Next, these regions are sometimes refined by using morphological operations and approximate liver region R_c in coronal images to limit boundaries of approximate liver-regions R_0 in axial image planes. Actually, these approximate liver regions R_0 should be inside the liver volume.

3.5.2 Generation of initial zero LSF in edge and confident region images

In this study, the seed region growing (SRG) image is considered as the edge image. Further, the confident region image is produced from the confident map function (CMF). Both the SRG and CMF present boundaries of anatomical structures like binary images. Therefore, this section proposed a simple algorithm to generate the initial zero level-set function for the both SRG and CMF images. This algorithm is shown in Figure 3-8.

First, some images are cut in the vertical planes from the 3D-SRG or 3D-CMF volume to represent the coronal SRG or CMF images. Next, approximate liver-regions in coronal images are obtained. It begins with the inverse operation to present boundaries of anatomical structures as black pixels. Meanwhile, homogeneous regions are inverted into the white pixels. Afterwards, morphological operations, such as opening and erosion, are use to separate large regions and remove tiny regions. Then, the connected component labeling technique is used to select the approximate liver region. Indeed, three properties of liver-region selection

(as presented in section 3.5.1) are used to seek the approximate liver regions R_c in coronal images.

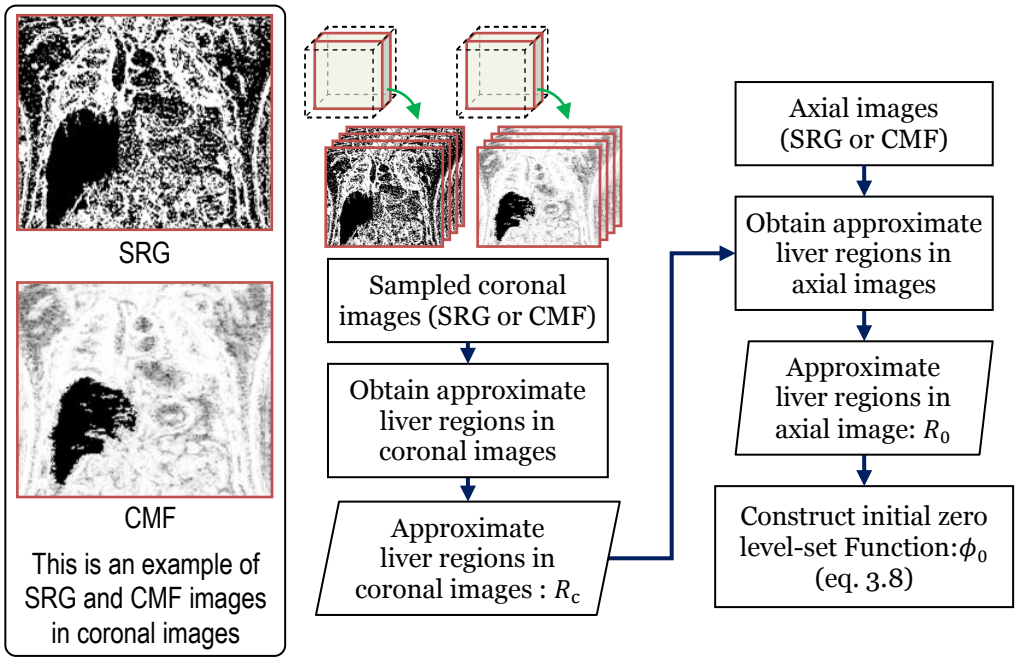

Figure 3-8 Diagram of the construction of initial zero level-set function in edge-based and confident region images

Afterwards, approximate liver-regions R_0 in axial images are extracted by the same consequent processes used in coronal images. Indeed, this region extraction is possibly assisted by the approximate liver regions R_c in coronal images because both axial and coronal images are perpendicular to each other. Subsequently, the approximate liver-region R_0 in each axial image is used to generate the initial zero level-set function by Equation (3.8).

In addition, if the construction of confident region images are considered, the approximate liver regions R_0 are equivalent to the labeled region L in Equation (3.6). Therefore, these regions are directly utilized to generate the confident region images.

3.6 Mask Generation for preventing leakage regions outside ribs

Due to the conditions of CT-image acquisition, some ranges of gray-intensities of the liver overlap other soft tissues such as spleen and tissues around ribs. Furthermore, some parts of the liver in CT images sometimes adhere to soft tissues outside ribs without edge information. Thus, the leakage regions outside ribs occasionally appear.

This section introduces an algorithm to generate masks for preventing these leakage regions. It aims to connect all bone regions in each axial image plane. It

begins with the extraction of the bone regions. This study introduces a two-stage multilevel Otsu's method with a range constraint (see section 3.6.1). It automatically extracts five classes of regions from each axial image. These classes contain background, three levels of soft tissues, and hard-tissue regions. Then, borders of all hard-tissue regions are linked. For example, a template of seed points (Figure 3-9) is created and moved to the boundary of the hard-tissue regions. Then, these seed points are connected by straight lines.

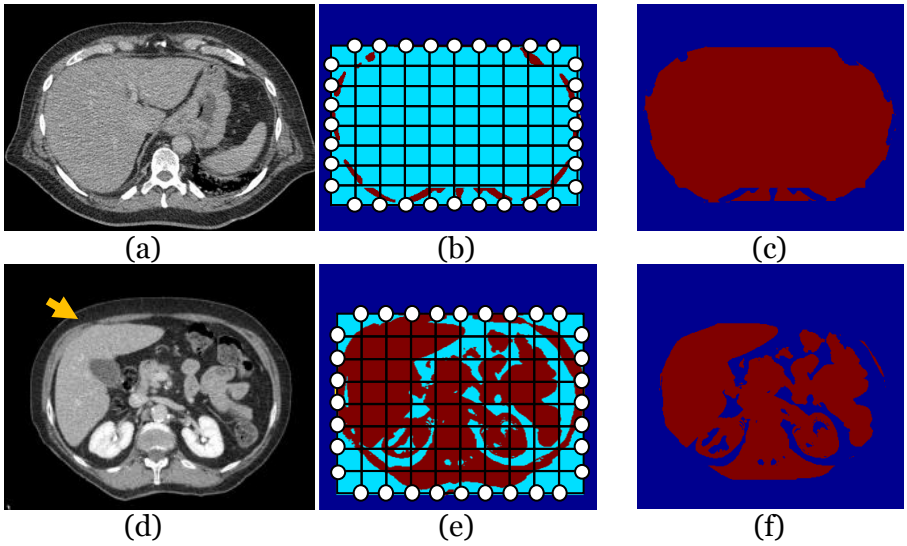

Figure 3-9 An example of mask creation; (a) and (d) Two sample images, (b) and (e) templates of seed points, (c) and (f) mask regions [38]

However, hard-tissue regions as ribs and vertebrae are not always clearly displayed as shown by a yellow arrow in Figure 3-9. Thus, a combination of soft-tissue regions is preferred instead of the hard-tissue regions. Conversely, the combined region of the soft tissue is often larger than a boundary of the ribcage. Therefore, morphological erosion is required to shrink this combined region after connecting all seed points together.

3.6.1 A two-stage multilevel Otsu's method with a range constraint

The Otsu's method [40] is a famous algorithm for image segmentation from a histogram of gray-intensities [41]. However, it consumes high computation cost when multiple-classes thresholding is preferred. Some algorithms [42, 43, 44] have been proposed to solve this problem. An attractive method is a two-stage multilevel Otsu's (TSMO) method [43]. It is introduced to accelerate computation without changing the result of original Otsu's method. Conversely, its results are not good to present

hard-tissue regions as shown in Figure 3-11. Thus, this study presents a simple solution by giving a range constraint.

To smooth comprehension, a summary of the Otsu's method is firstly explained. First, a given image is represented in L gray levels $\{1,2,3,\dots,L\}$. Let f_i denote the number of pixels at the gray level i, and then the total number of pixels is $N = \sum_{i=1}^{L} f_i$. Thus, the probability of occurrence of gray-level i is given by $p_i = \frac{f_i}{N}$. If a given image is divided into K classes $\{C_1, C_2, C_3, \dots, C_K\}$, the number of thresholds will be $K-1$. Consequently, the cumulative probabilities P_k and the mean levels μ_k in each class k is described by

$$P_k = \sum_{i \in C_k} p_i, \tag{3.11}$$

$$\mu_k = \frac{1}{P_k} \sum_{i \in C_k} i p_i. \tag{3.12}$$

Thus, the average μ_{image} of gray-levels in a given image is

$$\mu_{\text{image}} = \sum_{i=1}^{L} i p_i = \sum_{k=1}^{K} P_k \mu_k. \tag{3.13}$$

Meanwhile, the between-class variance is

$$\sigma^2 = \sum_{k=1}^{K} P_k \left(\mu_k - \mu_{\text{image}}\right)^2. \tag{3.14}$$

Therefore, the optimal thresholds $T^* = \{t_1^*, t_2^*, t_3^*, \dots, t_{K-1}^*\}$ is determined by

$$T^* = \underset{1 \le T \le L}{\arg\max}\ \sigma^2(T). \tag{3.15}$$

In the first stage of the TSMO [43], it groups the histogram of gray intensities to present as a small number of bins (see Figure 3-10). For example, if a given image contains 256 gray levels, these levels will be grouped into eight bins (32 levels per bin). Next, the Otsu's method is applied to these bins, and its results indicate optimal bins giving the maximum between-class variances. Afterwards, the Otsu's method is applied to gray-levels inside these optimal bins and their neighbors for obtaining optimal thresholds.

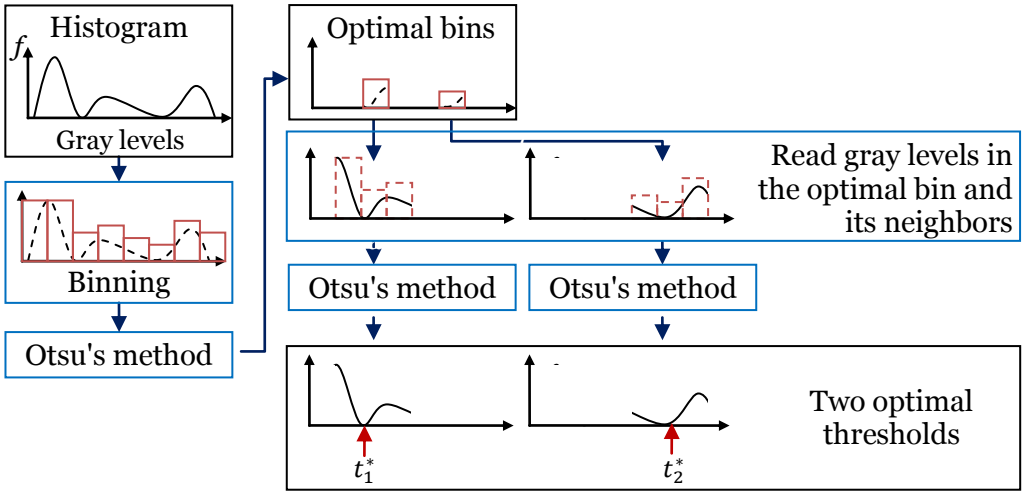

Figure 3-10 An example of the two-stage multilevel Otsu's method [43] for obtaining two optimal thresholds t_1^* and t_2^*.

Actually, many studies [45, 46, 47] presented a specific range constraint to improve results of the Otsu's method. However, it depends on a specific pattern of gray-intensities in a given image. This study defines a range constraint by cutting gray-intensities below the CT number of the water from original data. This range comes from two reasons. First, CT numbers of soft and hard tissues are normally higher than the water. Second, gray-intensities in the cut range generally illustrate air and some artifacts. This range constraint improves the original TSMO's result as shown in Figure 3-11.

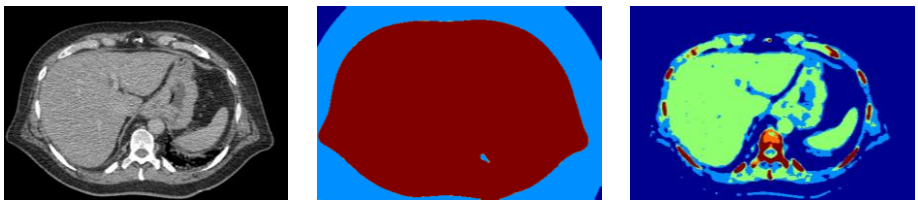

(a) (b) (c)

Figure 3-11 An example of five-class clustering on a 16-bits CT image (a) using TSMO method (b) and including a proposed range-constraint (c) [38].

3.7 Modified Chan-Vese model

An original Chan-Vese (CV) [31] model normally considers the global variation in mean of gray-intensities between inside and outside a given contour. In some cases, it will be difficult to stop the curve propagation at the boundary of the object of interest if this boundary shows lower variation of gray-intensities than another location. Therefore, this study proposes a modified Chan-Vese (MCV) model to reduce this

problem and achieve liver-image segmentation. This modification is formulated by connecting two main ideas.

First, the level-set evolution (LSE) equation of the CV model is referred, and it is defined by

$$\frac{\partial \phi}{\partial t} = \delta_\varepsilon(\phi)\left(\underbrace{\mu \mathrm{div}\left(\frac{\nabla \phi}{|\nabla \phi|}\right)}_{\text{curvature}} - \underbrace{v}_{\text{area}} - \underbrace{\lambda_1 (I - c_1)^2 + \lambda_2 (I - c_2)^2}_{\text{global gray intensity fitting}}\right), \tag{3.16}$$

$$c_1(\phi) = \frac{\int_\Omega I(\boldsymbol{x}) H_\varepsilon\big(\phi(\boldsymbol{x})\big) d\boldsymbol{x}}{\int_\Omega H_\varepsilon\big(\phi(\boldsymbol{x})\big) d\boldsymbol{x}}, \tag{3.17}$$

$$c_2(\phi) = \frac{\int_\Omega I(\boldsymbol{x}) \Big(1 - H_\varepsilon\big(\phi(\boldsymbol{x})\big)\Big) d\boldsymbol{x}}{\int_\Omega \Big(1 - H_\varepsilon\big(\phi(\boldsymbol{x})\big)\Big) d\boldsymbol{x}}, \tag{3.18}$$

where μ, v, λ_1, and λ_2 are constants. The variable I is a given image. The $H_\varepsilon(\cdot)$ is the Heaviside function, and $\delta_\varepsilon(\cdot)$ is the Dirac delta function where the variable ε denotes the width of the Dirac delta function. This LSE equation describes an area term as a constant v. It gives small contribution to the whole force if it is compared with remaining terms. Therefore, this study introduces an artificial balloon force to explain regions as a signed function. It is formulated by $F_\mathrm{A} = 2(G * R_0) - 1$ where G is a Gaussian smooth function. The variable R_0 is an initial region used to construct the initial zero level-set function.

Second, this study considers the Heaviside and Dirac delta functions. Actually, these functions differ from the definitions given in the edge-based level-set method [24]. The major difference is a quantity of elements responding to the Heaviside and Dirac delta functions. To explain the difference, the Heaviside $H_\varepsilon(z)$ and Dirac delta functions $\delta_\varepsilon(z)$ of the CV model are called "global type" and re-denoted by $H_\mathrm{G}(\varepsilon, z)$ and $\delta_\mathrm{G}(\varepsilon, z)$, respectively. On the other hand, "local type," $H_\mathrm{L}(\varepsilon, z)$ and $\delta_\mathrm{L}(\varepsilon, z)$ denote the Heaviside and Dirac delta functions used in the edge-based level-set model [24]. These definitions are rewritten as

$$H_\mathrm{G}(\varepsilon, z) = \frac{1}{2}\left(1 + \frac{2}{\pi}\arctan\left(\frac{z}{\varepsilon}\right)\right), \tag{3.19}$$

$$\delta_\mathrm{G}(\varepsilon, z) = \frac{1}{\pi}\frac{\varepsilon^2}{\varepsilon^2 + z^2}, \tag{3.20}$$

$$H_{\mathrm{L}}(\varepsilon, z) = \begin{cases} \frac{1}{2}\left(1 + \frac{z}{\varepsilon} + \frac{1}{\pi}\sin\left(\frac{\pi z}{\varepsilon}\right)\right) & \text{if } z \le |\varepsilon| \\ 1 & \text{if } z > \varepsilon \\ 0 & \text{if } z < -\varepsilon, \end{cases} \tag{3.21}$$

$$\delta_{\mathrm{L}}(\varepsilon, z) = \begin{cases} \frac{1}{2\varepsilon}\left(1 + \cos\left(\frac{\pi z}{\varepsilon}\right)\right) & \text{if } |z| \le \varepsilon, \\ 0 & \text{otherwise}. \end{cases} \tag{3.22}$$

If the input signal is varied from -2 to 2, and widths of the Dirac delta functions are defined by $\varepsilon = 0.1$, 0.3, and 0.5, the response signals will be illustrated in Figure 3-12.

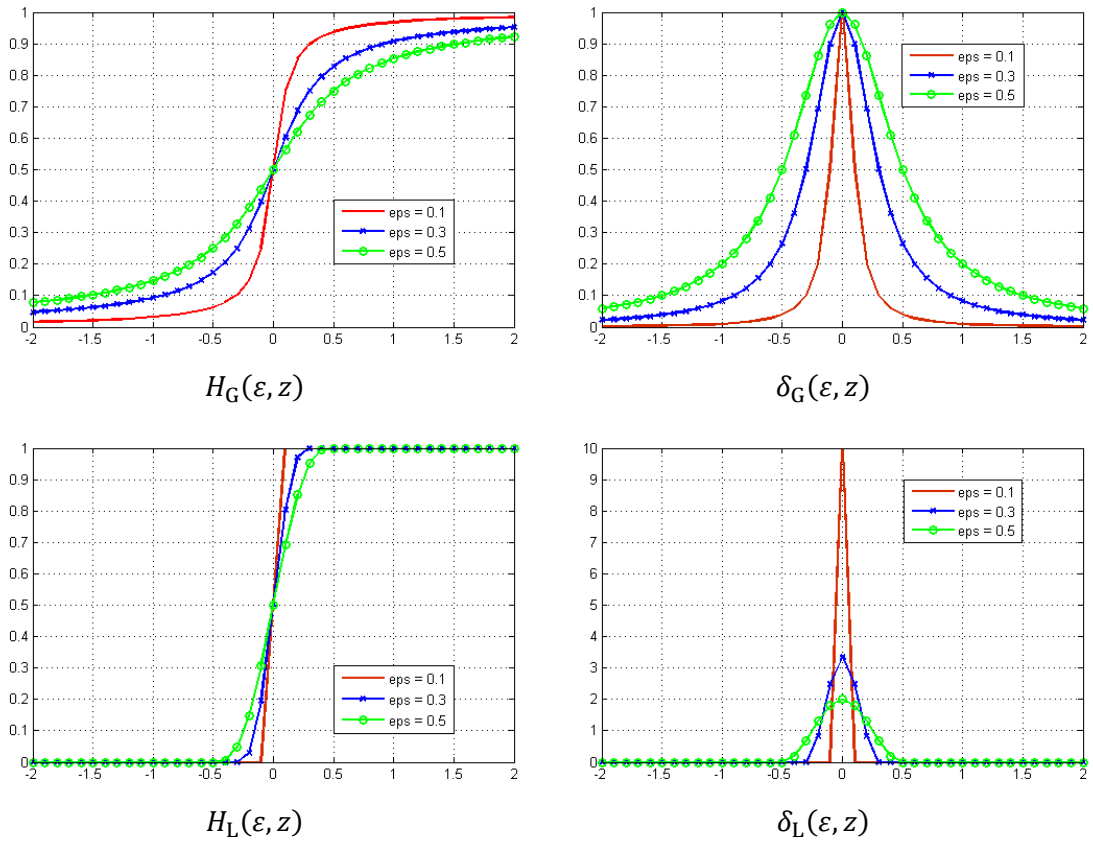

Figure 3-12 Three examples of response signals of (top) local and (bottom) global Heaviside functions where the width ε of the Dirac delta function are defined by ε = 0.1, 0.3, and 0.5.

The global type of the Heaviside function considers the wide range of the input signal. There are some small responses from the global Heaviside function although the input signal is out of a range of $-\varepsilon$ to ε. Further, if the level of ε is increased, the output of the Dirac delta function will be raised up.

On the other hand, the local type of the Heaviside function responds the input signal when it is more than the negative width of the Dirac delta function ($-\varepsilon$). It is

completely activated to one when the input signal is more than the positive width of the Dirac delta function (ε). Meanwhile, the Dirac delta function gives the output signal if the input signal is in a range of $-\varepsilon$ to ε.

However, from observation, CT axial images in an abdomen area contain many types of tissues and levels of gray-intensities. Furthermore, a variation of gray-intensities between a patient's body and background is larger than the difference in gray-intensities between the liver and neighbor soft tissues. Consequently, this study selects the local type to limit the force contribution in the curve propagation. For this local type of functions, the force is not computed from everywhere in a given image space. Moreover, this study simplifies the level-set evolution equation as

$$\frac{\partial \phi}{\partial t} = k_{\mathrm{P}} \left(\mathrm{div}\left(\frac{\nabla \phi}{|\nabla \phi|}\right) - F_{\mathrm{A}} + F \right) \delta_{\mathrm{L}}(\varepsilon, \phi), \tag{3.23}$$

$$F_{\mathrm{A}} = 2(G * R_0) - 1,$$

$$F = \lambda[-(I - c_1)^2 + (I - c_2)^2]$$

where k_{P} is a constant. In addition, the reaction-diffusion (RD) technique [26] is preferred to control the curve evolution with free re-initialization (see details in section 2.3.2). Thus, the proposed level-set model given by Equation (3.23) is integrated into the reaction term (Equation (2.18)). This reaction term is

$$\phi_{R(i)} = \phi_i + k_{\mathrm{R}} \left(k_{\mathrm{P}} \left(\mathrm{div}\left(\frac{\nabla \phi}{|\nabla \phi|}\right) - F_{\mathrm{A}} + F \right) \delta_{\mathrm{L}}(\varepsilon, \phi) \right), \tag{3.24}$$

where k_{R} is a constant for giving the reaction time-step. Next, the level-set function is propagated by

$$\phi_{i+1} = \phi_i + k_{\mathrm{D}} \Delta \left(\phi_i + k_{\mathrm{R}} \left(k_{\mathrm{P}} \left(\mathrm{div}\left(\frac{\nabla \phi}{|\nabla \phi|}\right) - F_{\mathrm{A}} + F \right) \delta_{\mathrm{L}}(\varepsilon, \phi) \right) \right). \tag{3.25}$$

where k_{D} is a constant for diffusion time-step.

In addition, an example of the difference in the original Chan-Vese model and the proposed modified Chan-Vese model are shown in Figure 3-13.

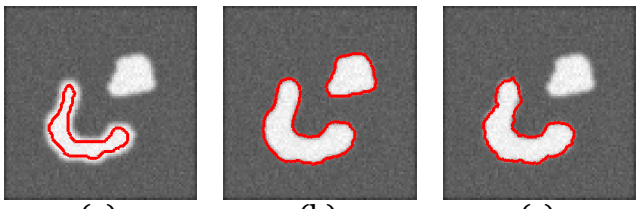

(a) (b) (c)

Figure 3-13 An example of image segmentation results when an initial zero level-set function is specific (a), and the level-set function is evolved by the original Chan-Vese model (b) and the proposed modified Chan-Vese model (c).

From the comparative result, the proposed modified Chan-Vese model presents the region near the initial region of the initial zero level-set function. Meanwhile, the original Chan-Vese model shows all regions, which present the same level of gray-intensities.

3.8 Refinement

To refine the segmentation results, this study applies a Gaussian smooth filter to coronal and sagittal image planes. Further, a hole-filling method is utilized to get outside boundaries of the liver regions.

3.9 Summary

The proposed liver-image segmentation system consists of three main steps. First, the construction of specific image representations is considered. This study considers edge-based and confident region images as alternative forms of gray-intensity images. Second, the level-set image segmentation is implemented by a concept of two-resolution approach for extracting the object of interest. It consists of initialization and evolution processes. This chapter proposes the construction of the initial zero level-set function and the modified Chan-Vese model. In the final step, the segmentation result is refined.

Chapter 4
Experiment and Results of 3D CT Liver-Image Segmentation

4.1 Introduction

This chapter presents some experiments and their results on the proposed liver-image segmentation system. First, some details of data sets are explained in section 4.2. Section 4.3 introduces the evaluation method for indicating accuracy of liver-image segmentation. Section 4.4 shows accuracy of segmentation results under four case studies that consist of the effect of the initial zero level-set function, the impact of multilevel edge detectors, the influence of image representation on GAC, CV, and edge-based level-set methods, and the performance of the proposed modified Chan-Vese model.

4.2 Materials

This section briefly introduces some characteristics of computed tomography (CT) images and a 4D-CT imaging system. The basic principle of CT imaging is to transform a series of projection datasets that are acquired at different angles around an object of interest into a cross-section image. This transformation is called an image-reconstruction process. The projection data is measurements of X-ray attenuation after X-rays transmit the object of interest to detectors locating on the opposite side [48]. Thus, a typical CT imaging scanner contains a couch, where a patient lies down, and the gantry, which is used to rotate an X-rays source and detectors for acquiring projection data (see Figure 4-1).

4.2.1 Standard CT numbers

After the image-reconstruction process finishes, cross-section images in axial image planes of the object of interest are visualized. Gray-intensities are described by standard CT numbers in the Hounsfield unit (HU). Indeed, the Hounsfield unit is computed from the linear attenuation coefficient of materials. These CT numbers are related to the attenuation coefficient of water [49] as

$$\text{CT number} = \frac{\mu_0 - \mu_{H_2O}}{\mu_{H_2O}} \times 1000 \tag{4.1}$$

where μ_0 and μ_{H_2O} are the linear attenuation coefficient of the object and water, respectively. Examples of CT numbers are shown in Table 4-1 [50].

Table 4-1 An example of CT numbers of different tissues (unit: HU)

Tissue Types	CT numbers	Tissue Types	CT numbers
Bone	+1000	Kidneys	30
Liver	40 to 60	Water	0
Blood	40	Fat	-100 to -50
Muscle	10-40	Air	-1000

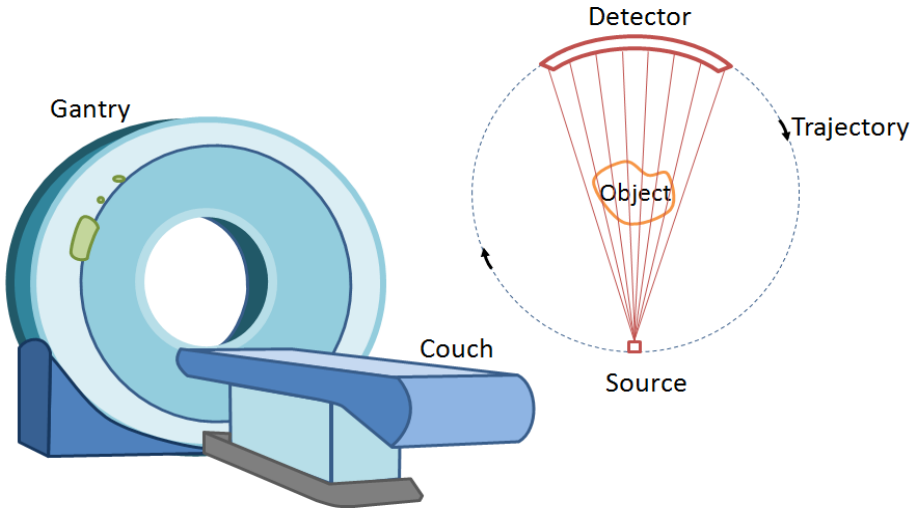

Figure 4-1 Basic Components of (left) a 3D-CT scanner and (right) projection-data acquisition

4.2.2 4D-CT Imaging

Generally, a 4D-CT imaging system contains two main components. First, a 3D-CT scanner is used to visualize anatomical structures. Second, a respiratory gate system is required to synchronize a respiratory signal with a 3D-CT imaging process. Thus, the 4D-CT imaging system can give a sequence of 3D-CT data sets in accordance with subsequent phases of a breathing cycle.

For example, a 4D-CT data set is acquired in a cine-mode [51] with a real-time position management (RPM) respiratory monitoring system as demonstrated in Figure 4-2. In this acquisition system, a small plastic block including infrared retro-reflective dots is placed on a patient's abdomen at a specific location to track motion by using an infrared camera. This tracking system gives the respiratory signal, which is correlated with the free-breathing CT data. In each couch's position, CT data is

continuously acquired covering a whole breathing-cycle before moving to the next couch's position. Indeed, the translation of couch's position is needed to collect anatomical images covering the region of interest. Afterwards, all CT images in different couch's positions at the same phase of a breathing cycle are arranged to generate a 3D-CT data volume.

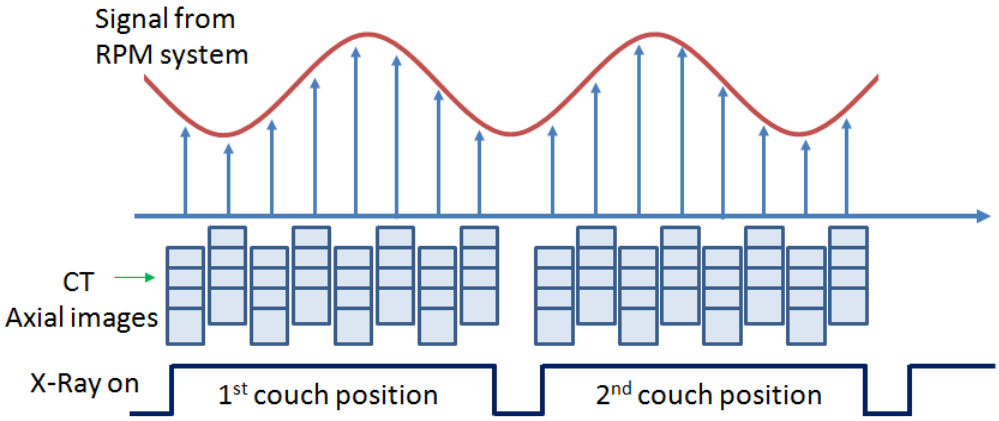

Figure 4-2 A diagram of 4D-CT imaging in a cine mode (modified from [51])

4.2.3 Information of data sets

This study investigated liver-image segmentation in CT images including following information.

Data sets are acquired from four patients by a 4D-CT imaging system (a GE Discovery ST machine and a Varian RPM system) in a cine mode with the free breathing conditions. For each patient, 10 different sets of 3D CT liver data are collected from different time-phases of a breathing cycle. These data sets correspond to the sequence of 0%, 10%, 20%, ..., and 90% time-phases of a breathing cycle. Thus, it may be possible to observe a change in anatomical structures caused by a respiratory process. These data sets are provided by the medical image data archive system (MIDAS) community, http://midas.kitware.com/community/view/47. Each 3D-CT data set includes 136, 120, 150, and 120 slices of 16-bits axial images for patient A, B, C, and D, respectively. The size of each axial image is 512x512 pixels with resolution 0.98 square millimeters, and slice thickness is 2.5 millimeters. In addition, this resource also provides manual delineations drawn by a radiologist.

4.3 Evaluation methods

To evaluate the accuracy of all segmentation results, three different types of similarity measures are used. They are the relative absolute-difference volume similarity (AVS), volume overlapped coefficient (VOC), and dice similarity coefficient (DSC) [52]. Then, these measures are averaged to present average accuracy of segmentation.

$$AVS = \left(1 - \frac{|V_S - V_M|}{|V_M|}\right) \times 100, \tag{4.2}$$

$$VOC = \left(\frac{|V_S \cap V_M|}{|V_S \cup V_M|}\right) \times 100, \tag{4.3}$$

$$DSC = \left(\frac{2|V_S \cap V_M|}{|V_S| + |V_M|}\right) \times 100, \tag{4.4}$$

where V_S and V_M represent a segmented volume and a manual-drawing volume, respectively.

4.4 Experimental results

The experiment contains four sections. First, an example of a quantitative measure is shown when the initial zero level-set function was constructed by the proposed process. It was compared with a manual-drawing based method. Second, the influence of the multilevel edge detectors in the confident region image representations is illustrated. Third, the effect of three different image representations is examined. Three standard level-set models were applied to gray-images, edge-images, and confident region images. Lastly, the proposed modified Chan-Vese method and some modern level-set methods are comparatively evaluated.

4.4.1 Influence of the initial zero level-set function

This section shows an example of influence of initial zero level-set function. The proposed initialization method was compared with a manual-drawing based method. The both methods were assessed under the conditions of edge-based image representation and a geodesic active contour (GAC) model.

The manual-drawing based method starts from subdividing a liver volume into two sections in the z-axis (a head-to-foot direction). This subdivision is required to reduce complicated shapes of the liver. Indeed, the liver region is small at the top layer and then it expands to the middle layer. Then, it shrinks to the small region at

the bottom. Two manual-drawing regions on the top and bottom of the liver volume are provided. Subsequently, the GAC model is selected to control the curve propagation. In addition, the segmentation result in each axial-image slice is used to construct the initial zero level-set function in the next consecutive image slice. Therefore, the segmentation process will perform from the top to the middle layers of the liver volume if the top section is considered. Otherwise, the segmentation process will be started from the bottom to the middle layers of the liver volume. The average accuracy of the liver-segmentation results is shown in Table 4-2.

A major problem found in the manual-drawing based method is an accumulated error. For example, an over segmented region from the prior axial-image is used to be an initial curve. If this initial curve is far from a boundary of the object of interest, it will be difficult for the GAC method to move the curve towards the boundary of the object of interest.

On the other hand, the proposed method used the liver regions extracted from the coronal images to correct an initial curve in each axial image before starting propagation. For instance, an initial curve was possibly shrunk by using morphological erosion in accordance with the size of liver regions in coronal images. However, liver segmentation in coronal images needs adequate accuracy.

Table 4-2 Average accuracy of segmentation results from 40 sets of 3D-CT data when initial zero level-set function is generated by two different types (unit : %)

Methods	AVS		VOC		DSC		Average	
	Mean	SD	Mean	SD	Mean	SD	Mean	SD
Manual-Drawing based Method	73.95	7.07	76.78	5.12	86.77	3.24	79.17	5.15
The Proposed Method	82.09	6.16	83.59	4.18	91.00	2.64	**85.56**	**4.33**

4.4.2 Influence of multilevel edge detectors

This section demonstrates an effective example of multilevel edge detectors based on $f(\sigma, I)$ and F_{COM} in Equations (3.3) and (3.4). The confident region images (CRI) were constructed from two choices. First, the CRI was created from an edge detector using a 9x9 Gaussian window with standard deviation $\sigma = 2.0$. Second, the CRI was generated from three levels of edge detectors and three consecutive images. The levels of edge detectors were formed by using 3x3, 9x9, and 27x27 Gaussian windows with standard deviations $\sigma_1 = 0.5$, $\sigma_2 = 2.0$, and σ_3=6.5, respectively. To construct the confident map function (CMF), the threshold value (T_2 in Equation (3.5)) was manually adjusted to get the best result in each choice. Moreover, the GAC model

with the reaction-diffusion technique was applied to control the curve propagation in the two choices. An example of segmentation result is shown in Figure 4-3 and an average accuracy of liver-image segmentation results is demonstrated in Table 4-3.

An advantage of a combination of gradient information is to reduce unclear boundaries. These boundaries are normally distorted by high level of image noises and some artifacts (see an arrow in Figure 4-3). Further, this combination can improve liver-image segmentation results around 1.73 % of accuracy.

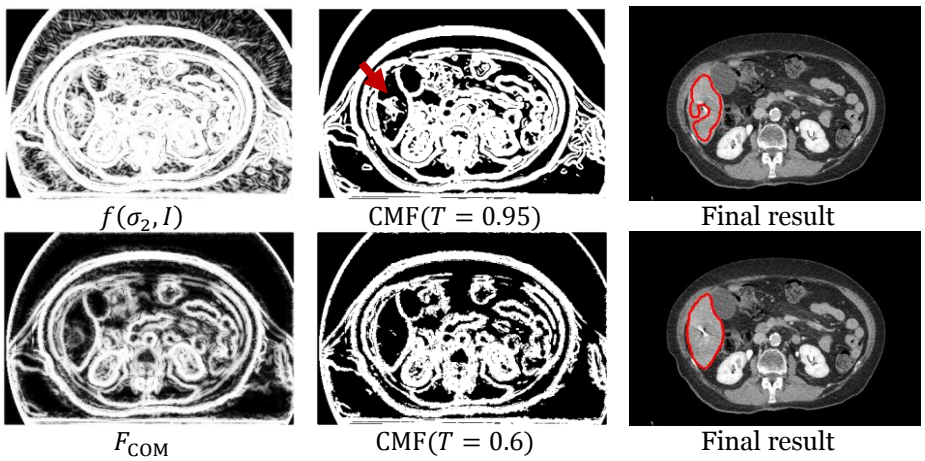

Figure 4-3 An example of liver-image segmentation when the RD-GAC method is applied to confident region images that are constructed from (top) one level edge detector without neighbor and (bottom) three level edge detectors with three consecutive images.

Table 4-3 Average accuracy of segmentation results from 40 sets of 3D-CT data when one level edge detector without neighbor is compared to three-level edge detectors with three consecutive images (unit : %)

Methods	AVS		VOC		DSC		Average	
	Mean	SD	Mean	SD	Mean	SD	Mean	SD
One level edge detector without neighbor	80.36	6.18	82.11	4.39	90.11	2.76	84.19	4.44
Three-level edge detectors with three consecutive images	82.48	1.85	83.99	1.47	91.29	0.87	**85.92**	**1.40**

4.4.3 Influence of image representations on standard level-set methods

This section investigates the influence of three different types of image representations. These image-types consist of gray-intensity images (GI), edge-based images (EI), and confident region images (CRI). In addition, three standard level-set methods were selected to evaluate their performances. These level-set methods are the geodesic active contour with the reaction-diffusion (RD-GAC) technique, the original Chan-Vese model with the RD technique (RD-CV), and the edge-based level-

set method with the distance regularized level-set evolution technique (DRLSE-E). Furthermore, Table 4-4, Table 4-5, Table 4-6, and Table 4-7 show the accuracy of liver-image segmentation results.

Table 4-4 Three similarity measures of segmentation results from four patients when an geodesic active contour (GAC) model with the reaction-diffusion (RD) technique is applied to three different types of image representations (unit :%)

Types of Representations	AVS		VOC		DSC		Average	
	Mean	SD	Mean	SD	Mean	SD	Mean	SD
Gray-Intensity Image (GI)	73.98	5.17	74.34	5.15	85.18	3.45	77.83	4.59
Edge-based image (EI)	82.09	6.16	83.59	4.18	91.00	2.64	85.56	4.33
Confident region image (CRI)	82.48	1.85	83.99	1.47	91.29	0.87	**85.92**	**1.40**

Table 4-5 Three similarity measures of segmentation results from four patients when the Chan-Vese (CV) model with the reaction-diffusion (RD) technique is applied to three different types of image representations (unit :%)

Types of Representations	AVS		VOC		DSC		Average	
	Mean	SD	Mean	SD	Mean	SD	Mean	SD
Gray-Intensity Image (GI)	-	-	23.82	20.65	38.47	0.85	20.76	0.50
Edge-based image (EI)	80.81	6.38	82.47	4.11	90.34	2.65	**84.54**	**4.38**
Confident region image (CRI)	-	-	23.52	1.28	38.06	1.69	20.53	0.99

Table 4-6 Three similarity measures of segmentation results from 40 sets of 3D-CT data when edge-based level-set model with the distance regularized level-set evolution (DRLSE) technique is applied to three different types of image representations (unit :%)

Types of Representations	AVS		VOC		DSC		Average	
	Mean	SD	Mean	SD	Mean	SD	Mean	SD
Gray-Intensity Image (GI)	80.54	3.50	81.39	3.43	89.70	2.11	83.88	3.02
Edge-based image (EI)	81.61	7.35	83.86	4.52	91.15	2.89	85.54	4.92
Confident region image (CRI)	83.73	2.42	84.91	1.92	91.83	1.13	**86.82**	**1.82**

Table 4-7 A summary of average similarity measures of segmentation results from 40 sets of 3D-CT data when three standard level-set models are applied into three different types of image representations (unit :%)

Level-set Models	Gray-intensity images		Edge-based images		Confident region images	
	Mean	SD	Mean	SD	Mean	SD
RD-GAC	77.83	4.59	85.56	4.32	**85.92**	**1.40**
RD-CV	20.76	0.50	**84.54**	**4.38**	20.53	0.99
DRLSE-E	83.88	3.01	85.54	4.91	**86.82**	**1.82**

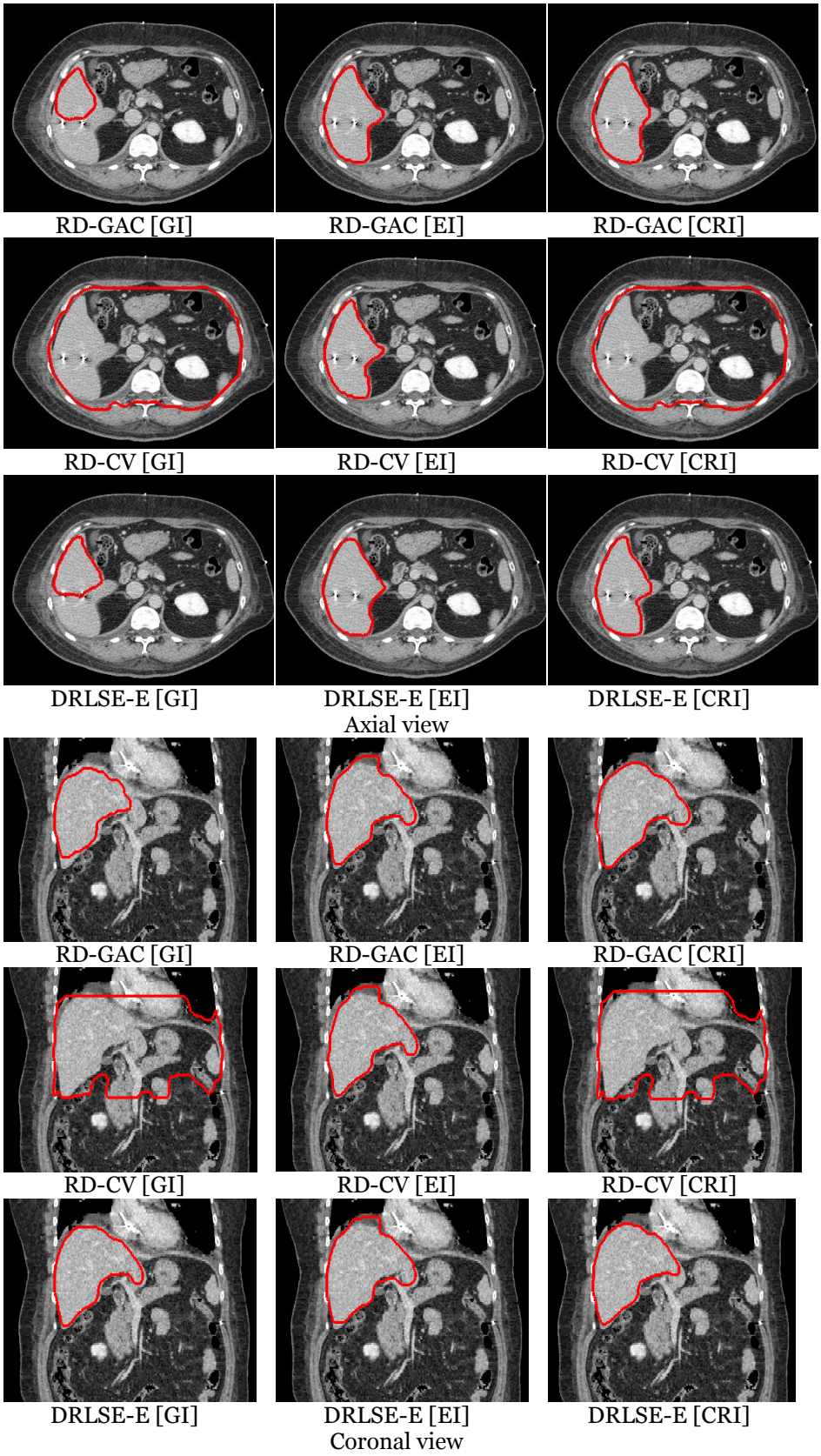

Figure 4-4 Some examples of segmentation results in axial and coronal views when three acceptable different level-set models are applied to three different types of image representations

From comparative results, the confident region image representation possibly improved the accuracy of segmentation when the RD-GAC or DRLSE-E model was applied to segment the liver volume from gray-intensity images or edge-based images. In the case of gray-intensity images, the RD-GAC and DRLSE-E models did not well propagate when metal artifacts appeared inside the liver regions. Meanwhile, the results of both models in edge-based images presented small leakage regions. This problem occurred when a high level of image noise causes some boundaries of the liver regions to open. Furthermore, the RD-CV model well extracted liver regions from edge-based images. However, it failed to segment liver regions from gray-intensity and confident region images. In those cases, the given curve moved outwards from the boundaries of liver to the mask borders (see Figure 4-4).

4.4.4 Performance of the proposed level-set method

In this section, the proposed modified Chan-Vese (MCV) model is applied to three different types of image representations. The results are shown in Table 4-8. Next, the best result of the proposed level-set method was compared with the best results of RD-GAC, RD-CV, and DRLSE-E level-set methods. Furthermore, a modified Chan-Vese model using gradient image (MCV09 [53]) was included into this comparison.

In summary, the MCV09 method formulated the level-set evolution equation as

$$\delta_\varepsilon(\phi)\left(\mu\mathrm{div}\left(\frac{\nabla\phi}{|\nabla\phi|}\right)-v-\lambda_1(I-\rho\nabla I-c_1)^2+\lambda_2(c_1-c_2)^2\right) \tag{4.5}$$

$$c_1(\phi) = \frac{\int_\Omega I(\vec{x})H_\varepsilon\big(\phi(\vec{x})\big)d\vec{x}}{\int_\Omega H_\varepsilon\big(\phi(\vec{x})\big)d\vec{x}}, \tag{4.6}$$

$$c_2(\phi) = \frac{\int_\Omega I(\vec{x})\left(1-H_\varepsilon\big(\phi(\vec{x})\big)\right)d\vec{x}}{\int_\Omega \left(1-H_\varepsilon\big(\phi(\vec{x})\big)\right)d\vec{x}}, \tag{4.7}$$

$$H_\varepsilon(z) = \frac{1}{2}\left(1+\frac{2}{\pi}\arctan\left(\frac{z}{\varepsilon}\right)\right), \tag{4.8}$$

$$\delta_\varepsilon(z) = \frac{1}{\pi}\frac{\varepsilon^2}{\varepsilon^2+z^2}, \tag{4.9}$$

where ρ is a constant. The variable I denotes a given image. Moreover, in this comparison, the MCV09 method was integrated into the RD technique to control curve evolution. Meanwhile, the initial zero level-set function was constructed by the same process as the proposed method for gray-intensity image representation (section 3.5.1).

Table 4-9 shows average accuracy of liver-image segmentation after the best results of modern level-set methods are compared. The best result was released when the proposed level-set method was applied to the confident region images. Further, the proposed modified Chan-Vese model gave a better result than the MCV09 method when both methods were computed under the same conditions of initial zero level-set function and gray-intensity images. The result showed improvement around 5.38% of accuracy. However, a major problem of gray-image representation found in the proposed level-set method is a metal artifact (see Figure 4-5). This problem causes a premature stop in the curve propagation.

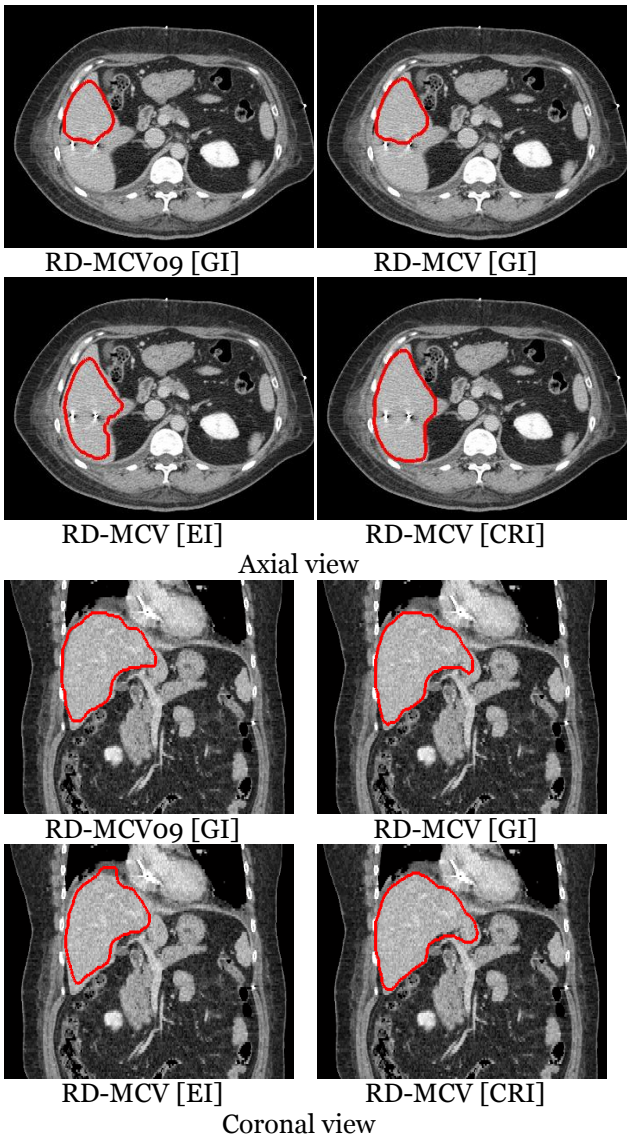

Figure 4-5 An example of segmentations in axial and coronal views when the proposed method and a modified Chan-Vese model using gradient image (MCV09) [53] are compared

Table 4-8 Three similarity measures of segmentation results from 40 sets of 3D-CT data when the proposed modified Chan-Vese model (MCV) with the reaction-diffusion (RD) technique is applied to three different types of image representations (unit :%)

Types of Representations	AVS		VOC		DSC		Average	
	Mean	SD	Mean	SD	Mean	SD	Mean	SD
Gray-Intensity image (GI)	78.55	3.95	79.55	3.86	88.56	2.42	82.20	3.41
Edge-based image (EI)	69.86	4.77	70.65	4.35	82.72	3.05	74.41	4.06
Confident region image (CRI)	84.21	2.34	85.12	2.00	91.95	1.17	**87.09**	**1.84**

Table 4-9 Average accuracy of segmentation results from 40 sets of 3D-CT data when several combinations of level-set methods and image representation are compared (unit :%)

Level-set methods	Types of Representations	Mean	SD
RD-GAC	Confident region images (CRI)	85.92	1.39
RD-CV	Edge-based images (EI)	84.54	4.37
DRLSE-E	Confident region images (CRI)	86.82	1.82
RD-MCV09	Gray-intensity images (GI)	81.71	4.07
RD-MCV (Proposed)	Confident region images (CRI)	**87.09**	**1.84**

4.5 Summary

The proposed 3D CT liver-image segmentation system was applied to CT images, which are acquired from a 4D-CT imaging system. Four issues were investigated in this chapter. First, it is possible to use coronal image planes to assist the construction of initial zero level-set function. The proposed technique showed higher accuracy than the manual-drawing based method. Second, the combination of multilevel edge detectors used in the construction of the confident region images (CRI) presented good boundary detection. Indeed, this detection seems to be better than using only one level of edge detector. Third, the accuracy of liver-segmentation is probably improved when the geodesic active contour (RD-GAC) or edge-based level-set (DRLSE-E) method is applied to the CRI. Actually, dirty regions appear inside the liver regions in the CRI fewer than gray-intensity and edge images. These dirty regions also produce gradient information as image noises. Meanwhile, performances of both RD-GAC and DRLSE-E methods are dependent on the quality of gradient information. Therefore, the RD-GAC and DRLSE-E cannot perform well when they are applied to gray-intensity or edge images. In contrast, the CRI cannot enhance the accuracy of liver-image segmentation when the curve evolution is managed by the Chan-Vese (RD-CV) model. Actually, the RD-CV mainly considers the global variation of mean of gray-intensities. In addition, the CRI describes a gray-intensity

level of a liver region as a mean of gray-intensities, and the large variation of gray-intensities normally appears around boundaries of a patient's body regions. Consequently, it is difficult to stop curve propagation at liver-region borders. Finally, the performance of the proposed modified Chan-Vese (RD-MCV) model was evaluated. The proposed RD-MCV uses the signed region function to present strong forces of approximate liver regions. Furthermore, the force contributions are not computed from all elements in a level-set function space. Meanwhile, the original RD-CV model considers all elements in the space. Thus, the proposed RD-MCV perhaps improves the original RD-CV model. From experimental results, the proposed RD-MCV using the CRI possibly presents the best accuracy of liver-image segmentation when it is compared with RD-GAC, RD-CV, DRLSE-E, and RD-MCV09 [53] methods. However, the proposed method cannot perform well if liver regions include large tumor areas. In that case, the proposed method cannot estimate good shapes of liver because some parts of liver regions are lost in these large tumor areas.

Chapter 5
Integration of Level-Set and Clustering Methods for Liver-Tumor Segmentation

5.1 Introduction

This chapter introduces integration of level-set and clustering methods for giving an example of tumor-region segmentation. It assumes that a liver-segmented image contains tumor regions, which are possibly approximated by a clustering result. Section 5.2 explains the related methods. Section 5.3 proposes a new combination of the modified Chan-Vese model and the clustering method. It is aimed to segment tumor regions in a noisy image. Section 5.4 shows segmentation results.

5.2 Related methods

One of impressive combinations is an integration of the edge-based level-set method [23] and spatial fuzzy C-mean (sFCM) [54] clustering. It is called the FCMLSM method [29]. The sFCM clustering is selected to give the approximate region of interest. Then, the approximate region is used to construct the initial zero level-set function and artificial balloon force in the edge-based level-set method.

Actually, the sFCM is a modified method of the fuzzy C-mean (FCM) clustering [55]. Thus, the FCM is firstly explained. Each data point is described by a degree of membership functions of all given C clusters in a clustering space. Let a set data points be $X = \{x_1, \dots, x_N\}$, and the objective function J_{FCM} given by Equation (5.1) needs to be minimized.

$$J_{\mathrm{FCM}} = \sum_{n=1}^{N} \sum_{i=1}^{C} (u_{i,n})^m \|x_n - c_i\|^2, \tag{5.1}$$

$$u_{i,n} = \left(\sum_{k=1}^{C} \left(\frac{\|x_n - c_i\|}{\|x_n - c_k\|} \right)^{\frac{2}{m-1}} \right)^{-1}, \tag{5.2}$$

$$c_i = \frac{\sum_{n=1}^{N}(u_{i,n})^m \cdot x_n}{\sum_{n=1}^{N}(u_{i,n})^m}, \tag{5.3}$$

where $u_{i,n}$ is a degree of membership functions of pixel x_n in the ith cluster centered at the c_i position. The variable $m \geq 1$ is a weight exponent, and its default value is equal to two. The objective function is minimized by using an iteration approach as follows.

Step 1: Randomize a matrix of membership function $U^{(t=0)} = \{u_{i,n}\}$ where t is an iteration index.

Step 2: Calculate the cluster center c_i

Step 3: Measure the distances among all data points and all cluster centers

Step 4: Update a degree of membership function $U^{(t+1)}$

Step 5: Check the condition, if $\left\|U^{(t+1)} - U^{(t)}\right\| < \varepsilon$ where ε is a constant that is used to stop the iteration; otherwise, return to step 2.

Next, the sFCM clustering was introduced to improve a performance of the FCM clustering when a given image includes image noise. It uses a spatial function $h_{i,n}$ to modify the membership function $u_{i,n}$ as follows.

$$u'_{i,n} = \frac{(u_{i,n})^p (h_{i,n})^q}{\sum_{k=1}^{C}(u_{k,n})^p (h_{k,n})^q}, \tag{5.4}$$

$$h_{i,n} = \sum_{k \in NB(x_n)} u_{i,k}, \tag{5.5}$$

where $NB(x_n)$ is a square window (e.g. 5x5-pixels window) centered at pixel x_n in the spatial domain. The parameters p and q are used to control the relative contribution between the membership function $u_{i,n}$ and the spatial function $h_{i,n}$. For example, if $p = 1$ and $q = 0$, the result of the modified membership function $u'_{i,n}$ will be identical to the conventional fuzzy c-means clustering.

After applying the sFCM clustering to a given image, each pixel in the given image is described by membership functions of all C clusters. Let $R_k \in [0,1]$ be the region of interest, and it is described by the membership function of the kth cluster. Then, a thresholding technique is applied to the region R_k, and a binary region is presented by $B_k = R_k \geq t$. The variable t is a constant indicating the acceptable degree of membership function. Moreover, this binary region is used to construct the

initial zero level-set function as $\phi_0 = -4\varepsilon(0.5 - B_k)$. The variable ε is a width of the Dirac delta function $\delta_\varepsilon(\cdot)$. Afterwards, the edge-based level-set method [23] is referred from

$$\frac{\partial \phi}{\partial t} = \mu\left(\Delta\phi - \operatorname{div}\left(\frac{\nabla\phi}{|\nabla\phi|}\right)\right) + \delta_\varepsilon(\phi)\left(\lambda \operatorname{div}\left(\mathrm{g}\frac{\nabla\phi}{|\nabla\phi|}\right) + v\mathrm{g}\right). \tag{5.6}$$

$$\delta_\varepsilon(\boldsymbol{x}) = \begin{cases} \frac{1}{2\varepsilon}\left(1 + \cos\left(\frac{\pi \boldsymbol{x}}{\varepsilon}\right)\right), & \text{if } |\boldsymbol{x}| \le \varepsilon, \\ 0, & \text{if } |\boldsymbol{x}| > \varepsilon, \end{cases} \tag{5.7}$$

$$\mathrm{g} = \frac{1}{1 + |\nabla G_\sigma * I|^2}, \tag{5.8}$$

The variables μ, λ, v are constants. The Gaussian function with the standard deviation σ is denoted by G_σ. Subsequently, the FCMLSM [29] method replaces the constant v in Equation (5.6) with a dynamic balloon force $G(R_k) = (1 - 2R_k)$. Therefore, the level-set evolution equation of the FCMLSM method is

$$\frac{\partial \phi}{\partial t} = \mu\left(\Delta\phi - \operatorname{div}\left(\frac{\nabla\phi}{|\nabla\phi|}\right)\right) + \delta_\varepsilon(\phi)\left(\lambda \operatorname{div}\left(\mathrm{g}\frac{\nabla\phi}{|\nabla\phi|}\right) + \mathrm{g}G(R_k)\right). \tag{5.9}$$

5.3 Integration of modified Chan-Vese and spatial fuzzy C-means clustering methods

If a noisy image is considered, the FCMLSM method may not perform well because it is dependent on the gradient information. Moreover, the Chan-Vese (CV) model can propagate a given curve without the gradient information, but it is sometimes difficult to stop the curve in a local area. Thus, this chapter proposes the integration of a modified Chan-Vese (MCV) and the spatial fuzzy C-mean clustering. This integration is denoted by the FCMMCV method.

First, the original Chan-Vese (CV) model [31] is referred, and its level-set evolution equation is

$$\frac{\partial \phi}{\partial t} = \delta_\varepsilon(\phi)\left(\mu \operatorname{div}\left(\frac{\nabla\phi}{|\nabla\phi|}\right) - v - \lambda_1(I - c_1)^2 + \lambda_2(I - c_2)^2\right), \tag{5.10}$$

$$c_1(\phi) = \frac{\int_\Omega I(\vec{x}) H_\varepsilon\big(\phi(\vec{x})\big) d\vec{x}}{\int_\Omega H_\varepsilon\big(\phi(\vec{x})\big) d\vec{x}}, \tag{5.11}$$

$$c_2(\phi) = \frac{\int_\Omega I(\vec{x})\left(1 - H_\varepsilon(\phi(\vec{x}))\right) d\vec{x}}{\int_\Omega \left(1 - H_\varepsilon(\phi(\vec{x}))\right) d\vec{x}}, \tag{5.12}$$

$$H_\varepsilon(z) = \frac{1}{2}\left(1 + \frac{2}{\pi}\arctan\left(\frac{z}{\varepsilon}\right)\right), \tag{5.13}$$

$$\delta_\varepsilon(z) = \frac{1}{\pi}\frac{\varepsilon^2}{\varepsilon^2 + z^2}, \tag{5.14}$$

where μ, v, λ_1, and λ_2 are constants. The variable I denotes a given image. Next, the constant v is replaced by a balloon force $\tilde{G}(R_k) = G_\sigma * (1 - 2R_k)$, where G_σ is the Gaussian smooth function with the standard deviation σ. The variable R_k denotes the region of interest in a clustering result of the sFCM clustering method at the kth cluster. Furthermore, a signed pressure force F_{SPF} function [56] is needed to assist in local segmentation, and it is described by

$$F_{\mathrm{SPF}} = \frac{I - \frac{1}{2}(c_1 + c_2)}{\max\left|I - \frac{1}{2}(c_1 + c_2)\right|}. \tag{5.15}$$

Subsequently, the modified Chan-Vese model is formulated by

$$\frac{\partial \phi}{\partial t} = \delta_\varepsilon(\phi)\left(\mu\left(\mathrm{div}\left(\frac{\nabla\phi}{|\nabla\phi|}\right) + \tilde{G}(R_k)\right) + F_{\mathrm{SPF}}\right). \tag{5.16}$$

The constant μ is used to control the smoothness of the given curve. Next, the reaction-diffusion (RD) technique [26] is required to control the curve evolution with free re-initialization process. Consequently, the level-set image segmentation is performed in the following steps.

Step 1: Use the binary region of the clustering result at the class k as $B_k = R_k \geq 0.5$ to generate the initial zero level-set function as

$$\phi_0(\boldsymbol{x}) = \begin{cases} -c_0 & ;\text{if } \boldsymbol{x} \in B_k, \\ c_0 & ;\text{otherwise.} \end{cases} \tag{5.17}$$

where c_0 is a positive constant.

Step 2: Define the reaction time-step k_{R} and compute the reaction term as

$$\phi_{R(i)} = \phi_i + k_{\mathrm{R}}\left(\delta_\varepsilon(\phi)\left(\mu\left(\mathrm{div}\left(\frac{\nabla\phi}{|\nabla\phi|}\right) + \tilde{G}(R_k)\right) + F_{\mathrm{SPF}}\right)\right). \tag{5.18}$$

Step 3: Give the diffusion time-step k_{D} and calculate the diffusion term

$$\phi_{i+1} = \phi_i + k_{\mathrm{D}}\Delta\left(\phi_{\mathrm{R}(i)}\right). \tag{5.19}$$

Step 4: Repeat step 2 and 3 until the stop condition is satisfied.

5.4 Experiment and Results

This study evaluates the performances of three level-set methods. All of them used the same results of the spatial fuzzy C-mean clustering to generate the initial zero level-set functions. Then, the FCMLSM, Chan-Vese (CV), and the proposed method (FCMMCV) were computed. Indeed, the evolution process of the Chan-Vese and the proposed methods were controlled by the reaction diffusion technique (RD).

5.4.1 Qualitative evaluation

Figure 5-1 shows four examples of tumor-region segmentation when RD-CV, RD-FCMMCV, and FCMLSM were applied to a mock CT 8-bit image [29] including some levels of the Gaussian, speckle, and Poisson noises. It was difficult for the RD-CV to extract tumor-regions (dark-gray areas) from the liver-tissue region (a bright-gray area). Actually, all results of the RD-CV method presented the boundary between liver-tissue and background regions. Meanwhile, the RD-FCMMCV and FCMLSM methods possibly distinguished tumor regions from liver-tissue areas. However, in the concave and convex areas, segmentation results of the RD-FCMMCV seemed to show small difference as indicated by blue arrows. In addition, the RD-FCMMCV probably gave the better segmentation result than the FCMLSM when a high level of the Gaussian noise was added into the image. Furthermore, after a speckle noise was added into the image, the result of the RD-FCMMCV perhaps showed a thin region at the in-between two tumor regions as pointed by yellow arrows. Actually, this region was thinner than the result of the FCMLSM. Next, the given image was contaminated by the Poisson noise. In this experiment, the Poisson-distribution numbers was generated by the Knuth's algorithm [57] and mean of distribution was equal to the gray-intensity value of each pixel. The segmentation result of the RD-FCMMCV slightly differed from the segmentation result of the FCMLSM.

Afterwards, the RD-CV, RD-FCMMCV, and FCMLSM methods were applied to a synthetic image (see Figure 5-2) including the Gaussian noise ($\sigma^2 = 0.01$). This synthetic image consists of four bar regions, and the third bar region from the left side is the object of interest. In this result, the RD-CV seemed to present all regions when their means of gray-intensities were equal or higher than the mean of gray-

intensities in the third bar region. Moreover, the third bar region was possibly extracted by the RD-FCMMCV and FCMLSM methods. However, some small dirty regions and a rough contour were appeared in the result of FCMLSM.

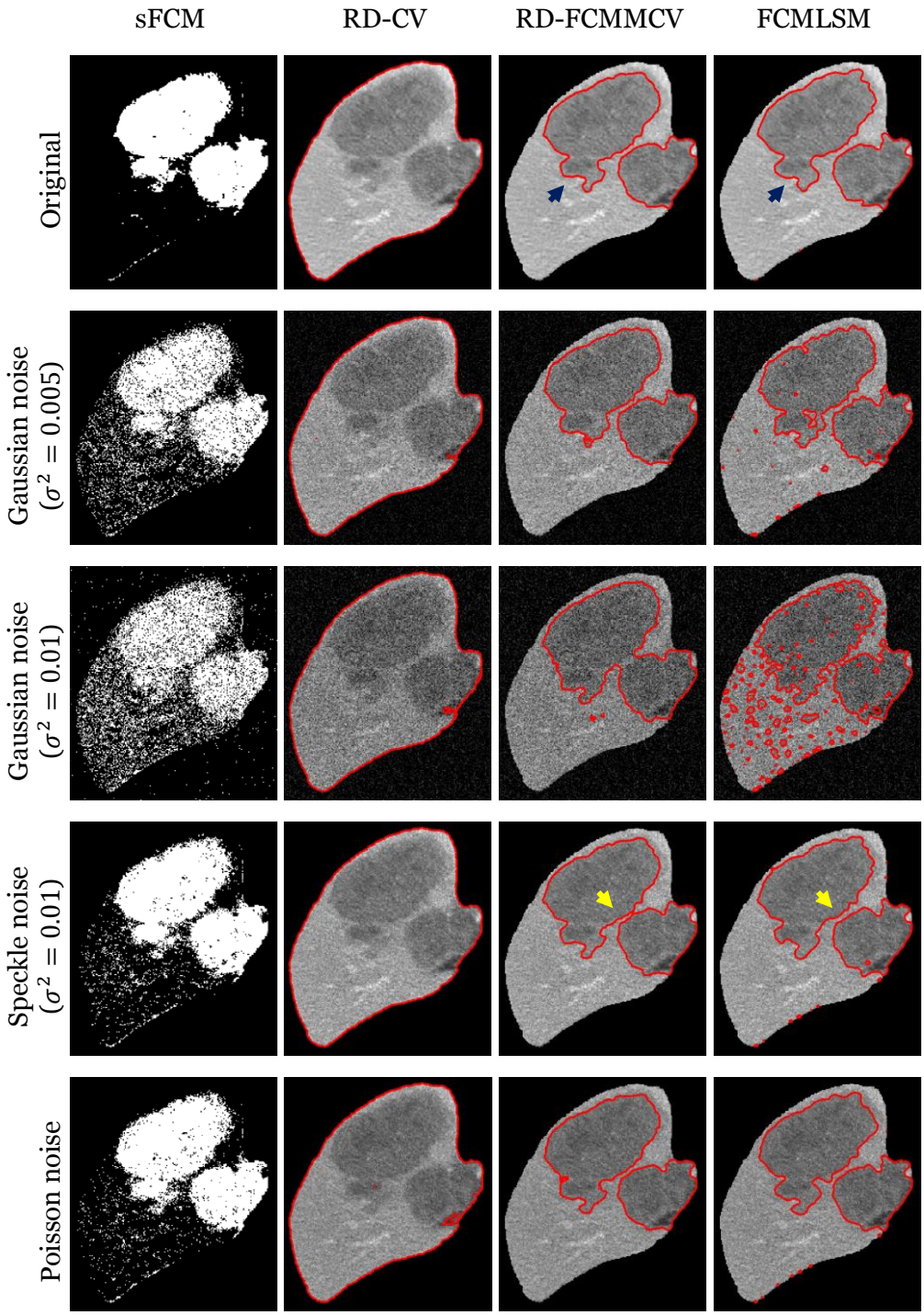

Figure 5-1 Five examples of tumor-segmentation results extracted by sFCM, RD-CV, RD-FCMMCV, and FCMLSM methods after a given image includes some image noises (modified from [58])

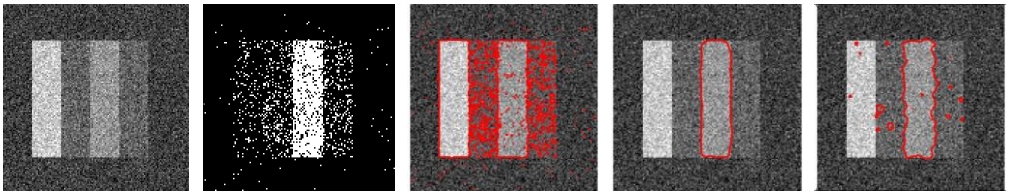

Original image sFCM RD-CV RD-FCMMCV FCMLSM

Figure 5-2 An example of the third bar region extracted by sFCM, RD-CV, RD-FCMMCV, and FCMLSM methods [58]

5.4.2 Quantitative measures

In this section, different variances σ^2 of the Gaussian and speckle noises and different maximum-mean $\lambda_{\max}$ of the Poisson distributions were added into the synthetic image. Furthermore, the level of image noise was measured by computing the signal-to-noise ratio (SNR) [59]. Then, the dice similarity coefficient (DSC) [52] was used to evaluate the accuracy of segmentation and it is described by

$$DSC = \left(\frac{2|S \cap R|}{|S| + |R|}\right) \times 100, \tag{5.20}$$

where the segmented and reference regions are indicated by S and R, respectively. Furthermore, The results are presented in Table 5-1, Table 5-2, and Table 5-3.

Table 5-1 The DSC values of the third bar region extracted from the synthetic images including different levels of the Gaussian noises

σ^2	SNR	RD-CV	RD-FCMMCV	FCMLSM
0.001	22.13	66.65	99.69	99.62
0.002	19.10	66.28	99.69	99.56
0.003	17.36	65.38	99.62	99.47
0.004	16.09	64.23	99.53	99.25
0.005	15.06	62.12	99.43	98.52
0.006	14.37	60.95	99.47	97.88
0.007	13.66	59.25	99.22	97.67
0.008	13.10	58.56	99.18	97.08
0.009	12.58	56.82	98.99	95.99
0.01	12.07	55.40	98.49	92.96
0.02	9.29	44.42	95.24	79.60
0.03	7.76	38.72	93.12	64.26
0.04	6.81	35.03	62.32	57.00
0.05	5.93	32.28	21.53	47.21

Table 5-2 The DSC values of the third bar region extracted from the synthetic images including different levels of the speckle noises

σ^2	SNR	RD-CV	RD-FCMMCV	FCMLSM
0.01	19.94	66.67	99.56	99.44
0.02	17.00	66.02	95.77	84.56
0.03	15.23	61.92	90.03	69.75
0.04	14.08	54.92	96.53	81.12
0.05	13.17	50.47	95.23	70.68
0.06	12.50	49.44	96.53	72.45
0.07	11.85	47.67	84.78	56.45
0.08	11.27	45.67	06.65	45.67

Table 5-3 The DSC values of the third bar region extracted from the synthetic image including different levels of the Poisson noises

$\lambda_{\max}$	SNR	RD-CV	RD-FCMMCV	FCMLSM
140	18.85	66.67	99.62	99.59
110	17.44	66.67	99.62	99.62
80	16.33	66.64	99.66	99.53
50	15.01	66.46	99.62	99.15
40	14.20	66.29	99.28	99.05
30	13.64	66.00	99.31	98.13
25	13.23	65.81	98.38	96.71
20	11.65	65.83	96.94	93.72
15	11.13	65.26	82.87	72.78

The results of RD-CV showed low accuracy because they normally contained the first bar region. It includes a mean of gray-intensities that is higher than the third bar region. Furthermore, the results of RD-FCMMCV slightly differed from the FCMLSM when the Gaussian noises were added into the image and the SNR was higher than 14 dB. However, the results of RD-FCMMCV seemed to be clearly better than the FCMLSM when the SNR was small and it was higher than 7 dB. In addition, the RD-FCMMCV probably improved around 20% of the accuracy of segmentation result from the FCMLSM when the speckle noises were added into the tested image and the SNR was in a range of 12 to 17 dB. Moreover, the different results of the RD-FCMMCV and the FCMLSM were not clearly presented when the tested image included the Poisson noises and the SNR was higher than 14dB. However, the remaining results showed a gradual drop in the accuracy.

5.4.3 Influence of image filtering

From the results in sections 5.4.1 and 5.4.2, the FCMLSM gives low accuracy of segmentation results when some high levels of image noises are added into a given image. A simple solution is to apply an image filter before performing the level-set evolution process. This experiment selected the median and mean-shift filters [60] to examine the influence of image filtering on the result of the FCMLSM and the proposed method (RD-FCMMCV).

First, the liver-tumor image including the variance of the Gaussian noise at $\sigma^2 = 0.01$ was considered. The segmentation results are shown in Figure 5-3. For the FCMLSM, the both of image filters possibly reduce many dirty regions in the liver tissue area appeared in Figure 5-1. On the other hand, the results of RD-FCMMCV display thin regions in-between two tumor regions as pointed by white arrows.

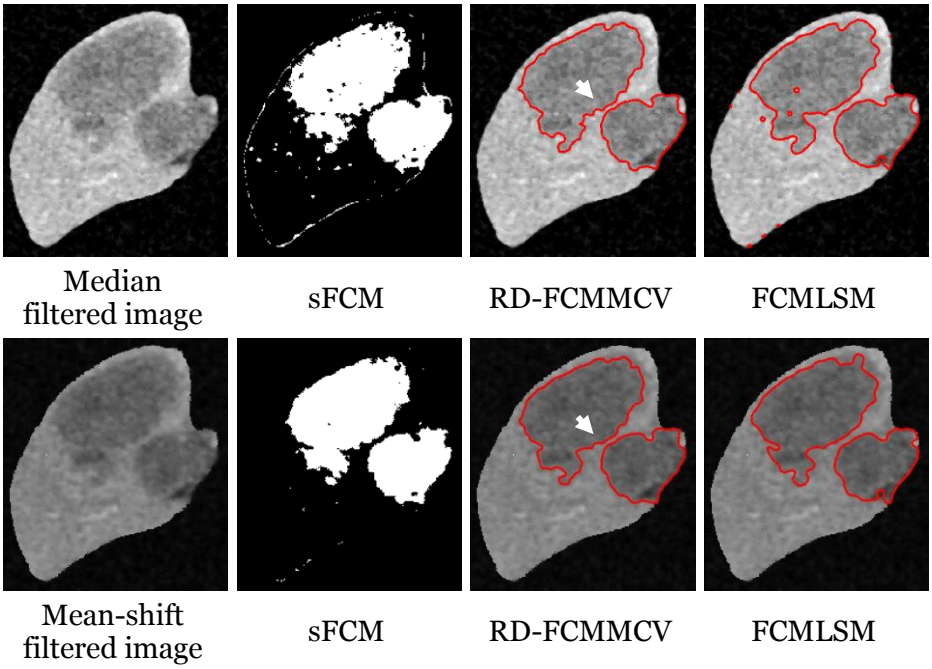

Figure 5-3 An example of tumor-regions segmented by the proposed method (RD-FCMMCV) and the FCMLSM when a given image including the Gaussian noise ($\sigma^2 = 0.01$) is filtered by the median and mean-shift filters.

Next, the Gaussian noise with the variance $\sigma^2 = 0.03$ was added to the four bar-region image. Then, this image was filtered and the third bar-region was extracted. The segmentation results are displayed in Figure 5-4. In the results of FCMLSM, the third bar region is clearly improved after applying one of two image filters. Conversely, a few number of small dirty regions appeared in the results. However, from further experiment, these dirty regions are possibly removed by increasing the large number of iterations in the evolution process. For the RD-FCMMCV, the results

are slightly improved when they are compared with the enhancement in the segmentation results of the FCMLSM.

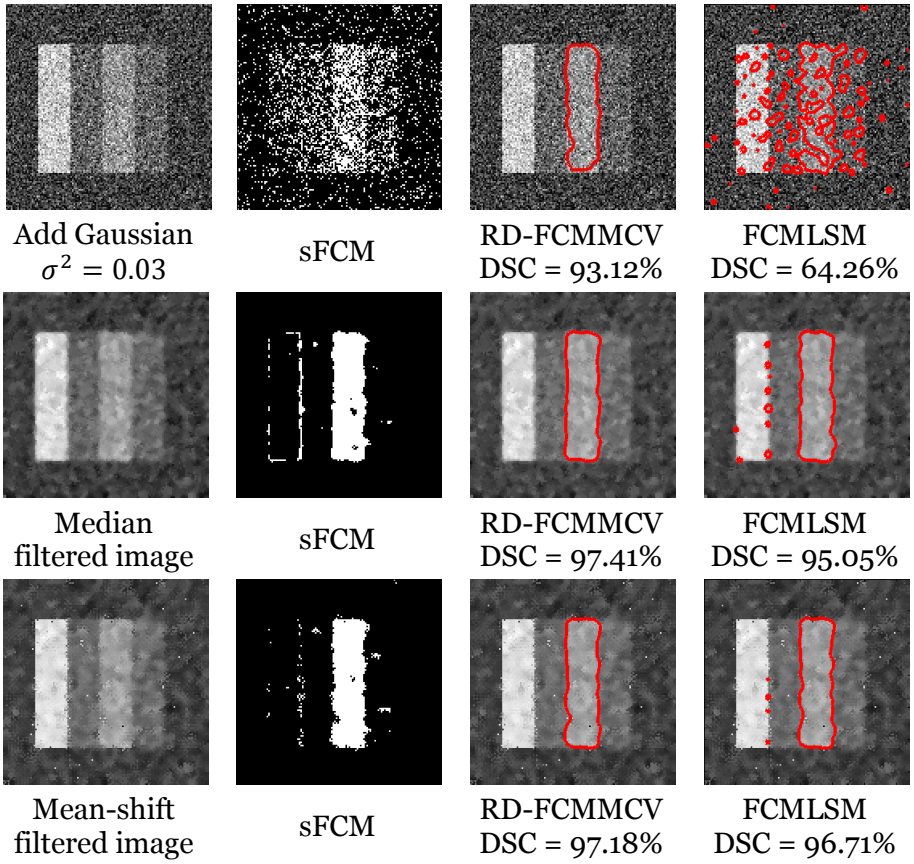

Figure 5-4 An example of the third bar region extracted by the proposed method (RD-FCMMCV) and the FCMLSM when the synthetic image including the Gaussian noise ($\sigma^2 = 0.03$) is filtered by the median and mean-shift filters

5.5 Summary

This chapter shows an example of tumor-region segmentation from a liver-segmented image. The integration of level-set and clustering methods is examined. A good point of this integration is released when the result of clustering gives the good initial zero level-set function. Further, it is possible to use the clustered region for creating force and modifying the Chan-Vese model. From experimental results, the integration of the spatial fuzzy c-mean (sFCM) clustering and modified Chan-Vese model possibly performs better than the integration of the sFCM clustering and edge-based level-set method when a given image includes some high levels of image noises. This improvement is achieved because the proposed method utilizes the relation of mean of gray-intensity between regions inside and outside a given curve. Meanwhile, the edge-based level-set method requires good gradient information to propagate the curve. In fact, this gradient information is sensitive to image noises.

Chapter 6
Visualization Application

6.1 Introduction

This chapter presents an example of liver-image segmentation application in a visualization topic. Section 6.2 briefly explains general concepts of visualization. Section 6.3 describes design of a simple visualization tool for a ray-casting technique. It is used to display a combination of original 3D data and segmentation results. An idea of this combination is explained in section 6.4. Section 6.5 illustrates a simple correlation between color and liver's displacements to visualize liver's motion.

6.2 General concepts of visualization

6.2.1 Multi-planar reconstruction

Generally, the anatomical structures in volumetric data are captured and displayed by cut-planes, which are used as a window to view the data in different locations and orientations. Typically, the axial, coronal, and sagittal planes are commonly required to visualize anatomical images from the head-to-feet, front-to-back, and left-to-right of the human body, respectively (see Figure 6-1).

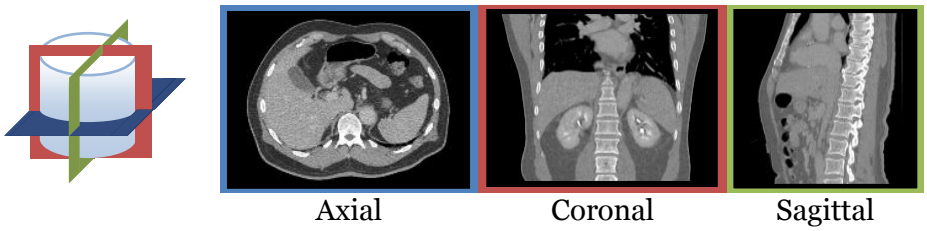

Figure 6-1 An example of axial, coronal and sagittal views

6.2.2 Contour or Surface representation

The boundaries of a specific organ can be enhanced by extracting contours. The marching squares (in 2D) or marching cubes (in 3D) [61] is one of famous algorithms giving outlines of anatomical structures. This algorithm outlines a target region from matching 16 patterns (see Figure 6-2) of cells (in 2D) or 256 patterns of cubes (in 3D) to a specific gray-intensity or a scalar value in each pixel or voxel. In fact, these patterns can be reduced by considering equivalent patterns. The pixels or voxels are located inside the contour if their gray-intensities or scalar values are greater than

this specific value of the contour. Otherwise, the pixels or voxels are positioned outside the curve or surface when their values are less than this specific value.

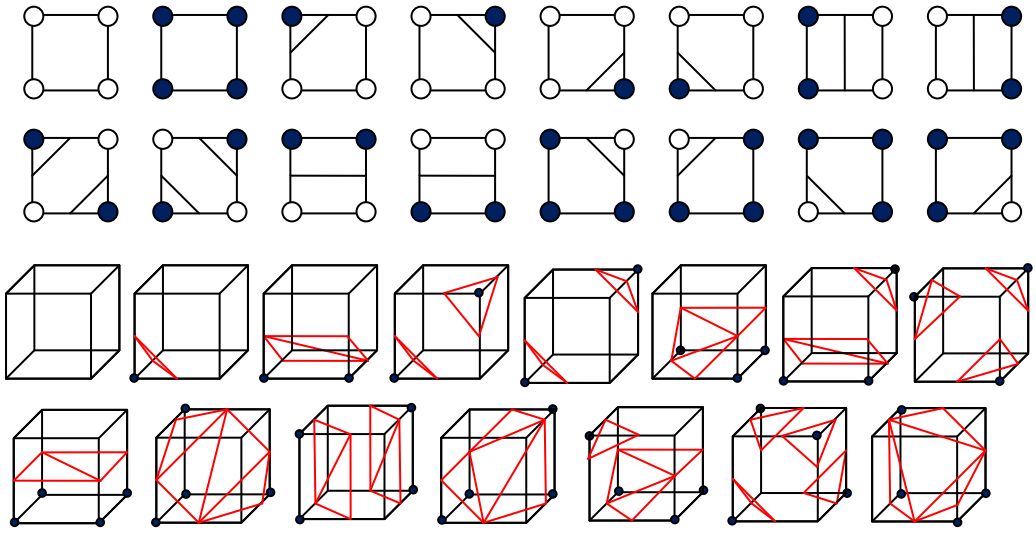

Figure 6-2 Examples of 16 patterns of 2D cells and 15 patterns of cubes represent contours and faces in 3D, respectively; the vertices inside the object are represented by black dots [62].

6.2.3 Volume rendering based on a ray-casting technique

Instead of geometric primitives as line and polygons used in contour or surface representations, an accumulation of scalar values in many voxels can convey visualization of anatomical structures. These scalar values are possibly considered to represent optical properties such as absorption and emission. The basic volume-rendering algorithm is ray casting, and it is investigated in this section.

The ray casting is a combination of scalar values of considered voxels on a given ray. This ray is projected from an image plane to a given volume (see Figure 6-3). Each voxel normally contains opacity and color values. Fundamentally, the opacity value is used to represent a degree of transmitted light after the given ray casts over the considered voxel. Therefore, visualization of each pixel on the image plane depends on the conversion of the combination of these scalar values.

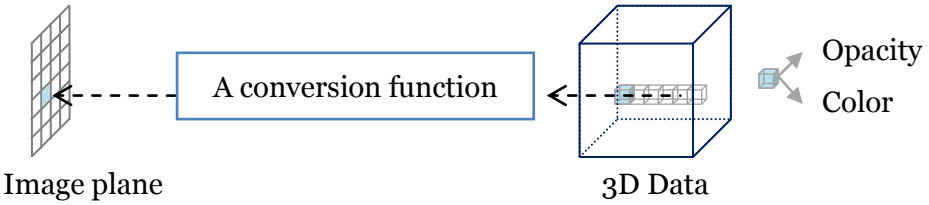

Figure 6-3 An example of ray casting over some voxels

A simple conversion determines the maximum intensity projection (MIP) value. Each pixel on the image plane is equal to the maximum value of all voxels along the given ray. However, it is difficult to explain the depth. Alternatively, an accumulation of opacity and color values can be calculated by the emission and absorptions model [63]. It is approximated by

$$\tilde{C} = \sum_{i=0}^{n} C_i \prod_{j=0}^{i-1} (1 - \alpha_j) \tag{6.1}$$

where $\tilde{C}$ is a final displayed value. The displayed value is equal to a combination of multiplication between current displayed value and transmitted energy $(1 - \alpha)$, where α is opacity. If the composite color is computed from back-to-front, its iterative formula is

$$C'_i = \alpha_i C_i + (1 - \alpha_i) C'_{i+1}, \tag{6.2}$$

where C'_i is the current composite color and C'_{i+1} is the composite color from the last position. Indeed, the location index is counted from an observer to a target. Thus, the index of the farther position is more than the front location. Moreover, the variable α_i denotes opacity at the current position.

For example [64], let the farthest voxel contains a green color $C_\mathrm{b} = [0,1,0]^\mathrm{T}$ and opacity $\alpha_\mathrm{b} = 0.4$. Further, the front voxel includes a red color $C_\mathrm{f} = [1,0,0]^\mathrm{T}$ and opacity $\alpha_\mathrm{f} = 0.5$. Thus, the composite color is $C'_\mathrm{f} = \alpha_\mathrm{f} C_\mathrm{f} + (1 - \alpha_\mathrm{f}) C'_\mathrm{b}$ and $C'_\mathrm{b} = \alpha_\mathrm{b} C_\mathrm{b}$ or

$$C'_\mathrm{f} = \left(0.5 * \begin{bmatrix}1\\0\\0\end{bmatrix}\right) + \left((1 - 0.5) * \left(0.4 * \begin{bmatrix}0\\1\\0\end{bmatrix}\right)\right) = \begin{bmatrix}0.50\\0.20\\0\end{bmatrix}.$$

Similarly, the accumulated opacity is $\alpha'_\mathrm{f} = \alpha_\mathrm{f} + (1 - \alpha_\mathrm{f}) \alpha'_\mathrm{b} = 0.5 + (0.5 * 0.4) = 0.70$.

6.3 Design of a simple visualization tool

6.3.1 Ray casting in the VTK library

In this study, a simple visualization tool is designed and developed by basing on a visualization toolkit (VTK) [65, 62] library. The VTK is an open-source library supporting C++, Tcl, Python, and Java languages. It provides different data representations such as points, polygons, images, and volumes. A concept of implementation is the pipeline. This concept is used to communicate among different

modules from data source to a displayed window. Fundamentally, a simple pipeline is formed as shown in Figure 6-4. It starts from sources or input data. Then, the data is modified by one or several filters. It is an optional module such as an interpolation operation. Next, a mapper module is required to connect between data processing and rendering. Subsequently, an actor is used to define appearance properties such as colors and positions. It is added to a renderer module in a window or a screen. Indeed, the renderer is needed to control a process of transforming geometry, light, and a camera view into an image scene.

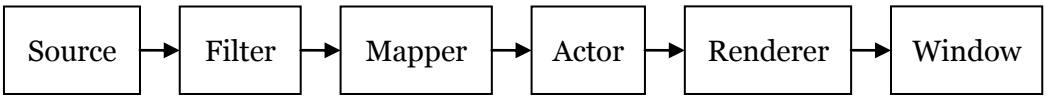

Figure 6-4 An example of a simple pipeline for using the VTK library

In the VTK library, the ray casting with the composite function is available in a simple pipeline as shown in Figure 6-5. The vtkVolumeRayCastMapper class is called to connect between a volumetric image-data and the actor (vtkVolume) for a rendering process. Meanwhile, the vtkVolumeRayCastCompositeFunction class is used to compute the composition of voxel values, which are stored in the vtkVolumeProperty class. Further, a user needs to design color and opacity tables for setting the properties of the rendered volume.

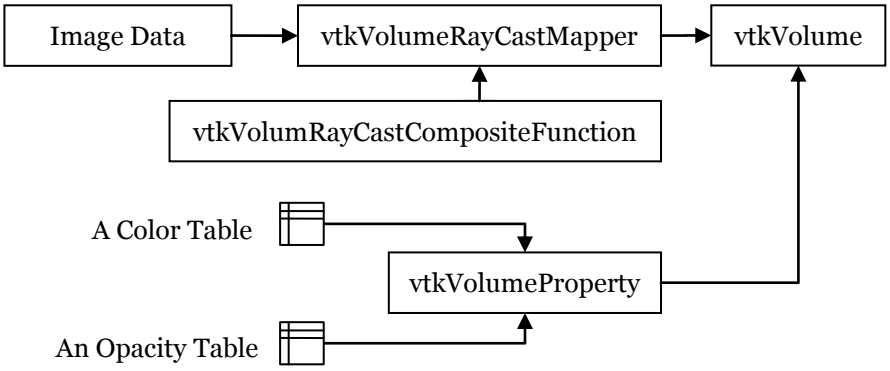

Figure 6-5 An example of a volume rendering pipeline in the VTK library

6.3.2 A concept of class design

To study correlation among gray-intensities, opacity, and color transfer functions, a conceptual class diagram is simply designed as illustrated in Figure 6-6.

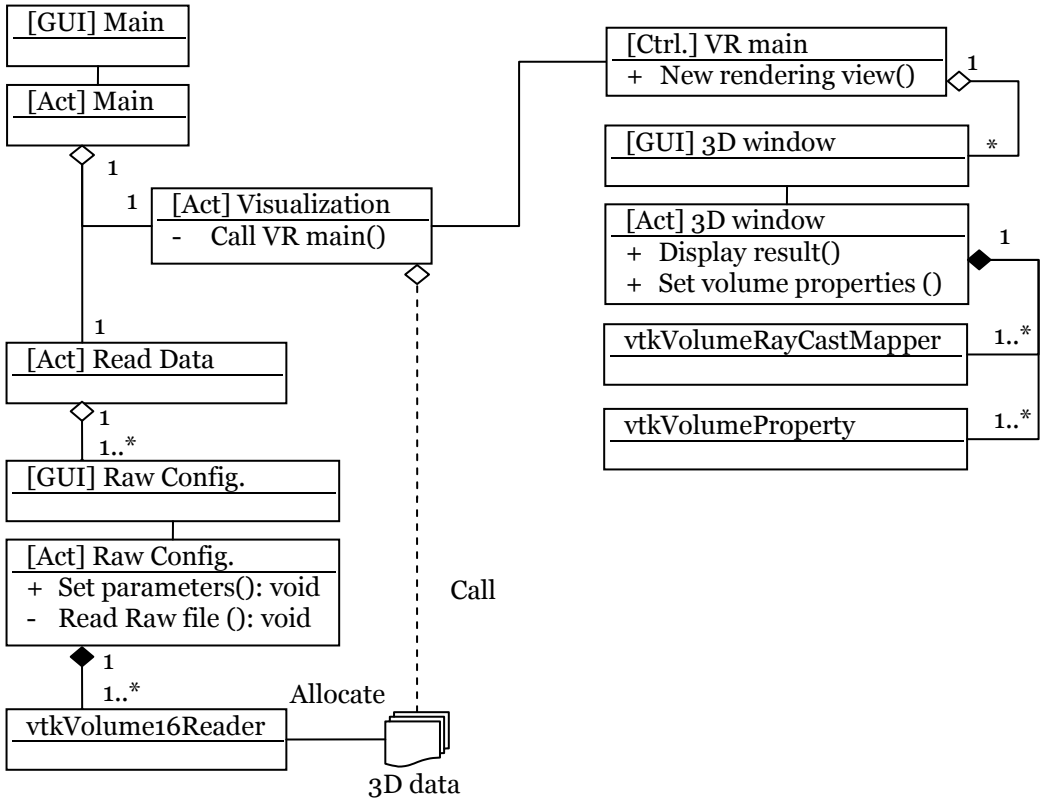

Figure 6-6 An example of a conceptual class diagram designed for a simple visualization tool

In this design, each graphic user interface (GUI) class is associated by the action class. It starts from the main GUI class that receives the command from a user. Then, it conveys one of two actions. First, the read-data class is used to import data in a raw format by using the vtkVolume16Reader class. It requires the raw configuration class to describe data dimensions and spaces. In addition, it is possible to import more than one 3D volume (it is denoted by an asterisk * symbol). Furthermore, the relation between the read-data class and the raw configuration class should be an aggregation type. However, the vtkVolume16Reader class should be destroyed after a window of the raw configuration class is closed. Meanwhile, 3D data is allocated in the temporary memory.

Second, the visualization in the action class type is used to call a volume-rendering module. After the volume-rendering module is preferred, the VR main class displays a ray-casting's result in the 3D window. Further, the 3D window class supports adjustment in the volume properties and updates them into the ray-casting result. For 4D volume rendering, however, this study considers relation between the color transfer function and motion information. This relation is used to define the

volume properties before rendering. Thus, it is assumed that memory and speed of computation are not critical problems.

6.3.3 Opacity and color transfer functions for the volume rendering

This section explains opacity and color transfer functions for indicating appearance of a volume data. These functions are simply converted from gray-intensity values. The opacity values are in a range of zero to one for controlling a degree of appearance. If the opacity is zero, the considered voxel will be disappeared. Moreover, they are usually relied on physical properties. For example, if a range of gray-intensities presents hard tissues in the standard CT number, opacity values should be high.

Figure 6-7 shows an example of adjustments in opacity and color values over a full range of gray-intensities. The blue arrows indicate a change of opacity values and red arrows show the color adjustment.

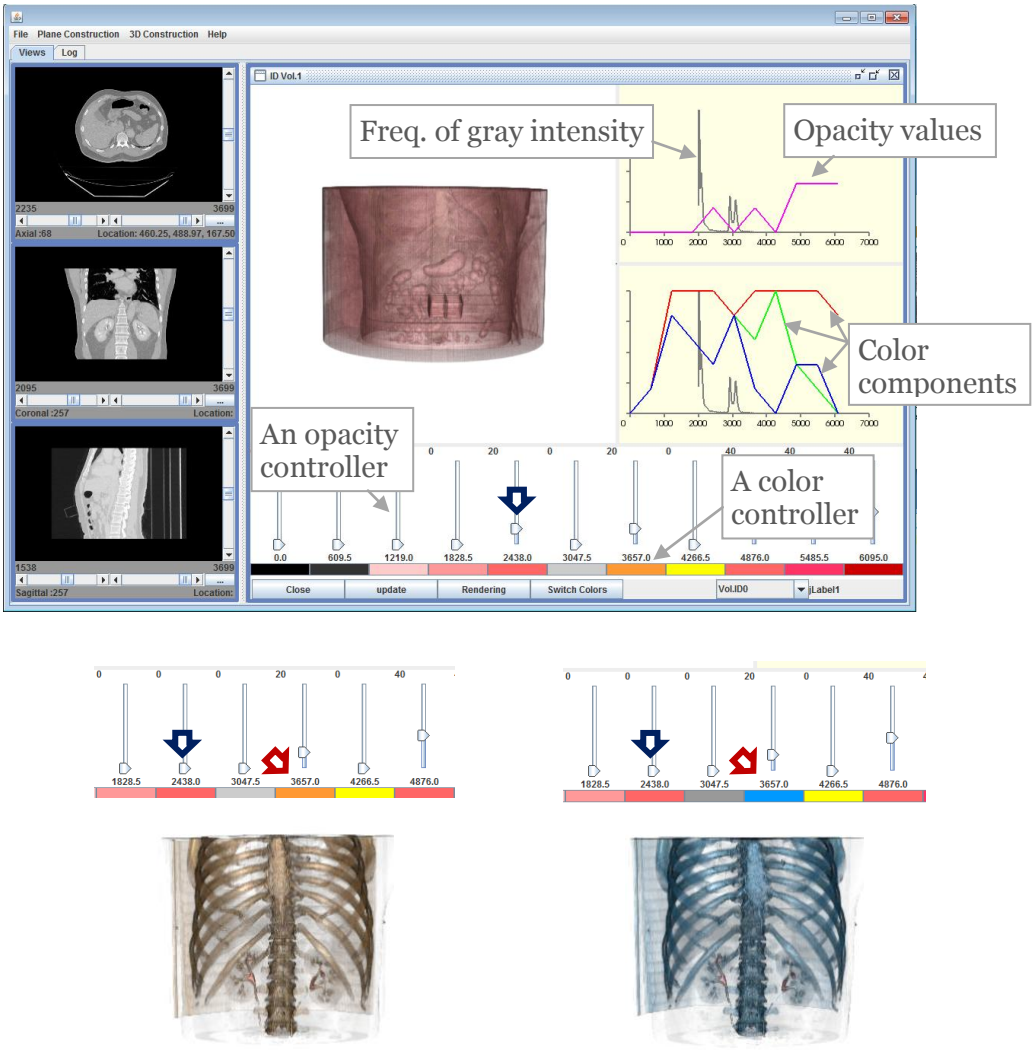

Figure 6-7 An example of design of opacity and color adjustments

Actually, this graphic user interface (GUI) permits a user to control the opacities and colors of sampling points. Thus, it is not necessary to identify opacity and color transfer functions for every level of gray-intensities.

6.4 Integration of original 3D data and segmentation results

6.4.1 A combination of original 3D data and a liver-segmented volume

Two simple combination methods are examined in this section. First, a direct-combination method is given by

$$I_{\mathrm{COM1}}(x) = I(x) + kL(x), \tag{6.3}$$

where $I(x)$ is an original volume, $L(x)$ is the binary liver-volume, and $k > \max\big(I(x)\big)$ is a constant. The variable x is a voxel coordinate. Then, the combined volume is refined by the Gaussian smooth filter to reduce the aliasing effect. Second, an indirect combination method begins with a separation between liver volume and the others. Next, each volume is multiplied by the original volume $I(x)$. This combination is defined by

$$I_{\mathrm{COM2}}(x) = \mathcal{N}_{t_0,t_1}\big(L^{\mathrm{c}}(x) \cdot I(x)\big) + \mathcal{N}_{t_1,t_2}\big(L(x) \cdot I(x)\big), \tag{6.4}$$

where $L^{\mathrm{c}}(x)$ denotes a compliment volume of the liver volume $L(x)$. Let $\mathcal{N}_{t_0,t_1}(\cdot)$ be a normalization operation, and gray-intensities of image input are normalized into a range of t_0 to t_1. This study defines $t_0 = 0$, $t_1 = 4500$, and $t_2 = 5000$. Afterwards, the combined volume is smoothed by the Gaussian smooth filter.

Next, full ranges of gray-intensities in both combination methods are normalized into a range of zero to 5000 gray-level. This normalization is required to compare the ray-casting's results of them.

Figure 6-8 shows enhancement of liver-visualization when a liver-segmented volume is combined with the original gray-intensity images. The opacity transfer functions (magenta line graphs) and color transfer functions (red, green, blue line graphs) are plotted over a histogram (gray line graphs). The opacity and color transfer functions in the first, second, and third rows are applied to original image data, I_{COM1}, and I_{COM2}, respectively.

In addition, (see blue arrows in Figure 6-8) the result of the direct combination method I_{COM1} presented distribution of gray-intensities smaller than the result of the indirect combination method I_{COM2}. However, these results showed insignificant difference.

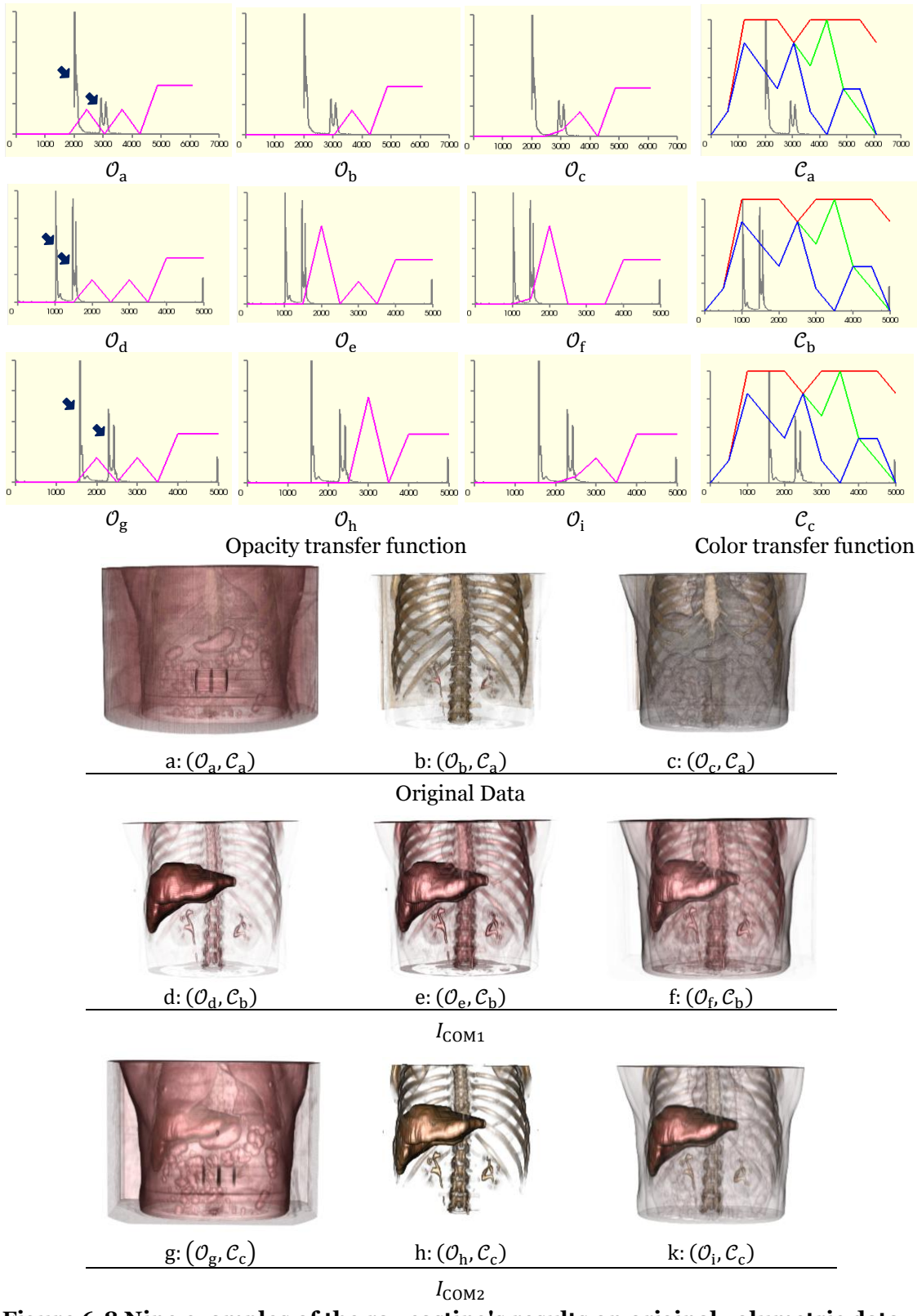

Figure 6-8 Nine examples of the ray casting's results on original volumetric data, and combinations of liver-segmented volume and original data in I_{COM1} and I_{COM2} methods

However, the indirect combination method seems to be a better choice than the direct combination method because it is possible to expand the distribution of gray-intensities. Consequently, it is convenient to adjust opacity and color transfer functions under this expansion. In contrast, this adjustment cannot clearly display remaining anatomical structures.

6.4.2 K-Means clustering for multi-region segmentation

This section shows an example of improvement in bone visualization by using K-means (KM) clustering.

The KM clustering [66] is normally introduced to divide data points $X = \{x_1, \dots, x_N\}$ into K clusters. It supports multi-dimensional vectors and gives high efficiency of computation. The purpose of this algorithm is to minimize the objective function of

$$J_{\mathrm{KM}} = \sum_{n=1}^{N} \sum_{k=1}^{K} b_{n,k} \|x_n - c_k\|^2 \tag{6.5}$$

$$b_{n,k} = \begin{cases} 1 & \text{if } k = \underset{a}{\operatorname{argmin}} \|x_n - c_a\|^2, a \in \{1, \dots, K\}, \\ 0 & \text{Otherwise,} \end{cases} \tag{6.6}$$

$$c_k = \frac{1}{N_k} \sum_{x \in C_k} x \tag{6.7}$$

where $\|\cdot\|$ is a distance measure. The variables c_k and N_k denote the center and the number of data points in the cluster C_k indexed by k. This algorithm can be summarized as follows.

Step 1: Initial cluster center $\{c_1, \dots, c_K\}$ is randomly sampled from the data points X.

Step 2: Measure the distances among all data points and all cluster centers

Step 3: Label cluster index (k) to each data point in accordance with the shortest distance.

Step 4: Determine new cluster centers from all member points in the same cluster.

Step 5: Repeat step 2 to 4 until the cluster labels do not change.

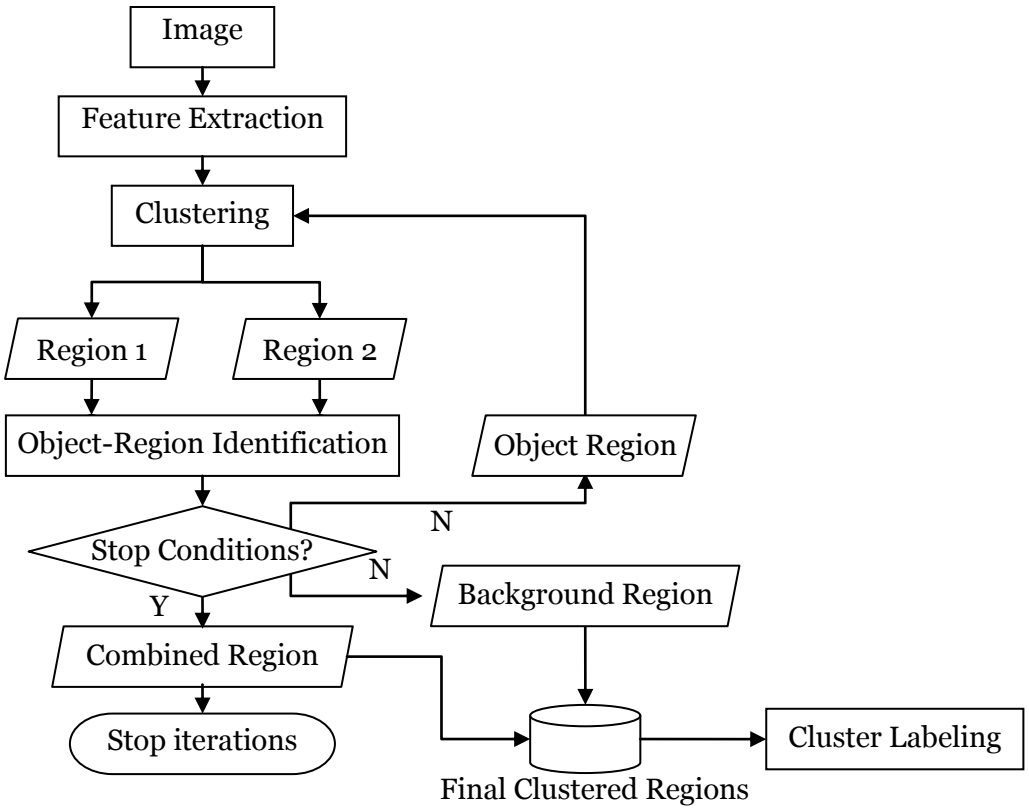

Figure 6-9 A diagram of the proposed multiple-regions segmentation [67]

To segment multi-regions in CT images, this study utilizes a simple approach as shown in Figure 6-9. It performs an iteration process under a hierarchical concept. It starts from the feature extraction, and each voxel is described by two components. The first component is collected from original gray-intensity image $I_{\mathrm{g}}(x)$, where x is a voxel coordinate. Meanwhile, the second component is acquired by applying a 3x3x3 median filter $I_{\mathrm{m}}(x)$. If a 3D volume includes N voxels, feature vector $\mathcal{F}$ is formed as

$$\mathcal{F} = \{f(x) | 1 \leq x \leq N\}, \tag{6.8}$$

$$f(x) = \{I_{\mathrm{g}}(x), I_{\mathrm{m}}(x)\}. \tag{6.9}$$

Next, a clustering process is performed under a hierarchical concept. In each level of a hierarchical model, all remaining feature vectors are subdivided into two clusters $K = 2$. Let D is the number of remaining feature vectors. Indeed, $D = N$ at the first clustering process. Further, if initial cluster centers are randomly defined, clustering results may be changed. To avoid the change in clustering result, initial cluster centers c_k are possibly obtained by

$$c_k = \{\text{mean}\left(\{I_{\text{g}}(p)|d_0 \le p \le d_1\}\right), \text{mean}\left(\{I_{\text{m}}(p)|d_0 \le p \le d_1\}\right)\} \tag{6.10}$$

$$d_0 = 0.5D \times (k-1) + 1, \tag{6.11}$$

$$d_1 = 0.5D \times k, \tag{6.12}$$

where $k \in \{1, 2\}$ is a cluster index. Give $\text{mean}(\cdot)$ is a mean operation. Then, all feature vectors in each group are transformed into a binary region b_k. If the clusters is denoted by C_k, the region will be created by

$$b_k(x) = \begin{cases} 1 & \text{if } f(x) \in C_k, \\ 0 & \text{Otherwise.} \end{cases} \tag{6.13}$$

After two regions are generated, one of them is identified as an object-region and the other is a background region. To indicate the object region, two parameters are determined. The first parameter μ_k is the mean of gray-intensities in each region. It can be obtained after multiplying the binary region b_k and original gray-intensities from the given images. Further, a threshold T_{gray} is used to limit a range of gray-intensities in the same type of materials or tissues. On the other hand, the second parameter s_k is the number of white pixels in each binary region b_k. Moreover, a threshold T_{size} is used to define size of small region that should not be further extracted in the next iteration.

Indeed, parameters $b_k, \mu_k, s_k, T_{\text{gray}}$, and T_{size} are used to produce some conditions for indicating the object-region and stopping the iteration process. These conditions are shown in Algorithm 6-1 [67], and there are three ideas behind this algorithm. First, the difference in means of gray-intensities between two clustered regions should be large adequately to verify that both clustered regions are not the same type of materials or tissues. Second, if a considered region is very small or it possibly includes one type of material, it is not necessary to further subdivide the considered region. Third, a considered region will be the object region if its size is large adequately and its mean of gray-intensities is higher than the other region.

Algorithm 6-1: Object-Region Identification and Stop Conditions

Input	b_1, b_2, μ_1, μ_2, s_1, s_2, T_{gray}, and T_{size}
Output	object region(r_{obj}), background region(r_{bg}), and a stop flag (f_{stop})

```
If (|μ1 − μ2| > T_gray) ∨ ((s1 + s2) > T_size)
   If      (μ1 > μ2)
           If          (s1 > T_size) ∧ (s2 > 0)
                       r_obj = b1 and r_bg = b2
           Else If     (s2 > T_size) ∧ (s1 > 0)
                       r_obj = b2 and r_bg = b1
           Else
                       f_stop = true and r_bg = b1 ∪ b2
           End If
   Else
           If          (s2 > T_size) ∧ (s1 > 0)
                       r_obj = b2 and r_bg = b1
           Else if     (s1 > T_size) ∧ (s2 > 0)
                       r_obj = b1 and r_bg = b2
           Else
                       f_stop = true and r_bg = b1 ∪ b2
           End If
   End If
Else
   f_stop = true and r_bg = b1 ∪ b2
End If
```

However, if the stop conditions are satisfied, both regions are merged and integrated into a final clustering result. Otherwise, if the stop conditions are not verified, all feature vectors in the object region will be sent backwards to the clustering process. Simultaneously, the background region is combined with the final clustering result. After the final clustering result is released, each region in this result is labeled by

$$l = \underset{t}{\text{argmin}}(|\mathbf{L}(t) - \mu_k|), \tag{6.14}$$

where $\mathbf{L} = \{-1000, 0, 50, 200\}$ is a set of estimated means of gray-intensities in background, fat, soft tissue, and hard tissue. The variable $l \in \{1, \dots, 4\}$ is a label related to the index of the set $\mathbf{L}$, and $\mu_k$is a mean of gray-intensities inside a region of the k^{th} cluster. Thus, all labeled regions are presented as subsequent indexes of background, fat, soft tissue, and hard tissue, which are denoted by $\boldsymbol{C} = \{c_{\text{air}}, c_{\text{fat}}, c_{\text{soft}}, c_{\text{hard}}\} = \{1,2,3,4\}$.

6.4.3 Integration of original 3D data, a clustering result, and a liver-volume

All labeled regions in the clustering result $\boldsymbol{C}(x)$ and a binary liver volume $L(x)$ are simply combined with the original 3D data as formed in Equation (6.15). The variable x denotes the voxel coordinate. This combination begins with multiplication between the clustering result and an original volume $I(x)$ in each labeled region. Then, the result of each multiplication is normalized into the specific range of gray-intensities. Similarly, the binary liver-volume is multiplied by the original volume $I(x)$ before the normalization is performed by giving $\{t_0, \dots, t_5\} = \{0,500,1000,3500,4500,5000\}$.

$$I_{\mathrm{COM3}}(x) = \mathcal{N}_{t_0,t_1}\big(c_{\mathrm{air}}(x)\cdot I(x)\big) + \mathcal{N}_{t_1,t_2}\big(c_{\mathrm{fat}}(x)\cdot I(x)\big) + \mathcal{N}_{t_2,t_3}\big(c_{\mathrm{soft}}(x)\cdot I(x)\big) + \mathcal{N}_{t_3,t_4}\big(c_{\mathrm{hard}}(x)\cdot I(x)\big) + \mathcal{N}_{t_4,t_5}\big(L(x)\cdot I(x)\big) \quad (6.15)$$

Figure 6-10 illustrates six examples of ray-casting's results when three types of color transfer functions $\mathcal{C}$ and six types of opacity transfer functions $\mathcal{O}$ are applied to the combined images $I_{\mathrm{COM3}}(x)$. The clustering results can help to enhance visualization of sternum, costal cartilages, and ribs. Further, surfaces of kidneys and some parts of blood vessels are possibly enhanced. Figure 6-10 (d)-(f) presents a little influence on ray-casting's result when the Gaussian function is applied to the opacity transfer function in each interval of gray-intensities. The Gaussian helps to reduce accumulation of opacity values among different classes. In fact, this effect is not significantly presented if a user can freely adjust opacity values over a full range of gray-intensities. However, the free adjustment on both opacity and color transfer functions may be a tedious process for a user.

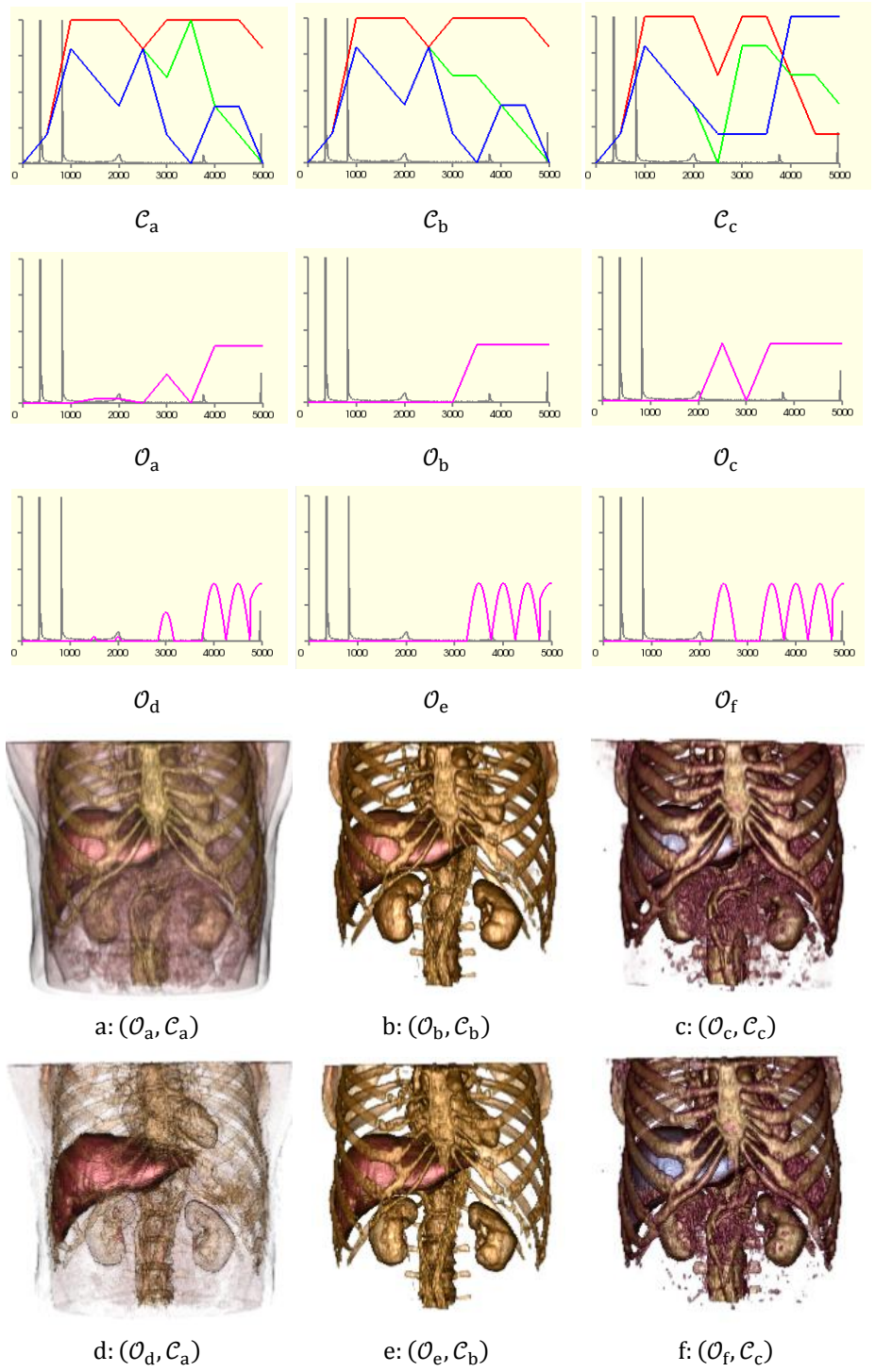

Figure 6-10 Six examples of ray casting results after combining original 3D CT data, clustering result, and liver-segmented volume; let $\mathcal{O}$ and $\mathcal{C}$ denote opacity and color transfer functions.

6.5 Visualization of liver's motion

Fundamentally, a 4D CT data set contains a series of different 3D CT data sets. In this study, 10 different sets of 3D CT data $\{P_0, \dots, P_9\}$ are collected from a patient, and they are acquired in different phases of a breathing cycle. Thus, it is possible to visualize liver's motion by giving correlation between color transfer function and displacement parameters. This idea is explained in this section.

First, the displacements in three axes of a Euclidean space are obtained by using a rigid image registration. The basic framework of image registration based on the insight toolkit (ITK) [68] library is referred. This framework is shown in Figure 6-11.

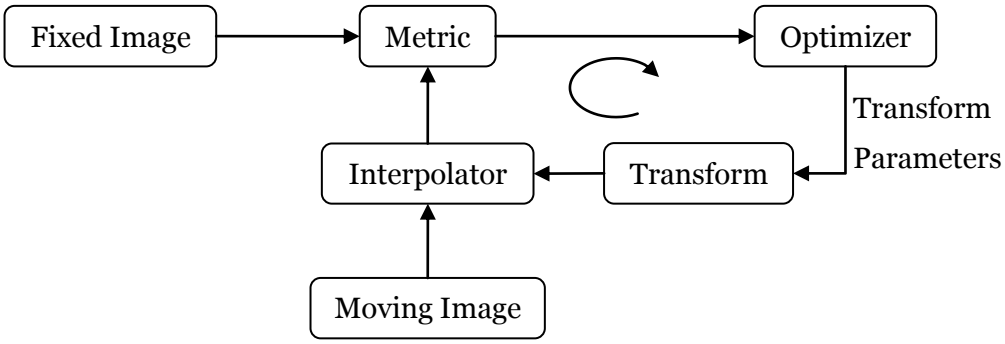

Figure 6-11 A basic image-registration framework [68]

Let the zero phase of a breathing cycle P_0 be the fixed image. Meanwhile, remaining data sets $\{P_1, \dots, P_9\}$ are defined as moving images. The target is to transform each data in remaining data sets to the zero phase P_0. Further, the linear interpolation is required to evaluate pixel value at non-grid locations after applying transform parameters to the moving image. To validate accuracy of image registration, mean of square differences (MS) is used as a metric component.

$$MS(A, B) = \frac{1}{N}\sum_{i=1}^{N}(A_i - B_i)^2 \tag{6.16}$$

where A_i and B_i denote two comparative images indexed by pixel coordinate i. In addition, this similarity metric is used to be an indicator for the optimizer component. This study utilizes the gradient descent to perform optimization for giving optimal parameters of the transform.

After every moving-image is transformed by the rigid image registration, translation parameters in x, y, and z-axes are presented. Actually, these translation

parameters describe displacements of the liver volume from P_0 to P_n, where $n = \{1, \dots, 9\}$ (see Figure 6-12).

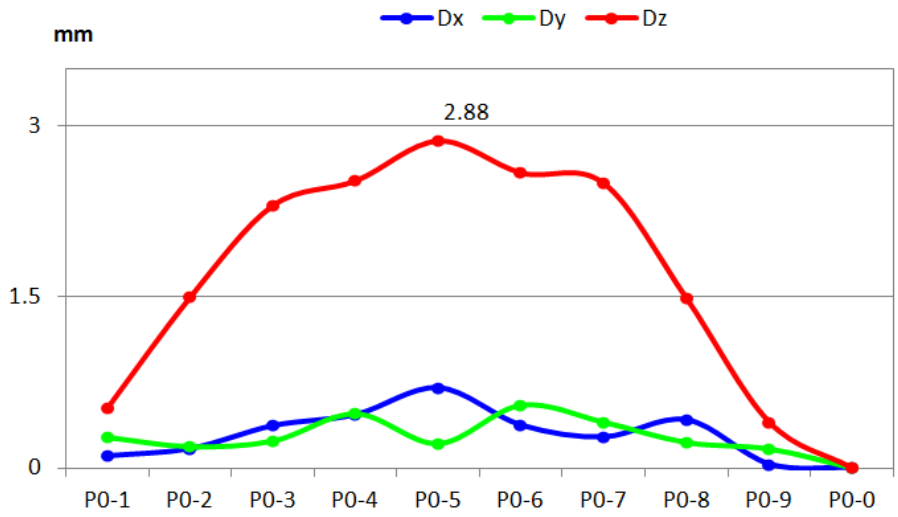

Figure 6-12 Three line graphs of displacements in x, y, and z-axes

Subsequently, the color transfer function is designed to explain two properties. The first property is to indicate the major direction of the liver's displacements. This property is simply defined by using B, G, and R color components for presenting translations in x, y, and z-axes, respectively. For example, if the displacement mainly appears in x-axis, the liver volume will be displayed in the blue color-component. Thus, let $a \in \{1,2,3\}$ be an index of the color set $\mathcal{C} = \{B, G, R\}$ and translation set $T = \{t_x, t_y, t_z\}$. Thus, absolute values of translations are used to indicate the presented color-component c_p by indexing as

$$c_\mathrm{p} = \mathcal{C}\left(\underset{a\in\{1,2,3\}}{\operatorname{argmax}} |T(a)|\right). \tag{6.17}$$

Next, the second property is to describe relation of displacement in the major displacement axis. Let $d_{\max}$, $d_{\min}$, and d be maximum, minimum, and current values of absolute displacement. Then, a color component c_p is represented in a range of zero to one [0,1]. Therefore, the final color c_f of the liver volume is

$$c_\mathrm{f} = \frac{d - d_{\min}}{d_{\max} - d_{\min}} c_\mathrm{p} \tag{6.18}$$

From Equation (6.18), a liver volume will be presented in the brightest color if the absolute displacement is the maximum. An example of the visualization is shown in Figure 6-13.

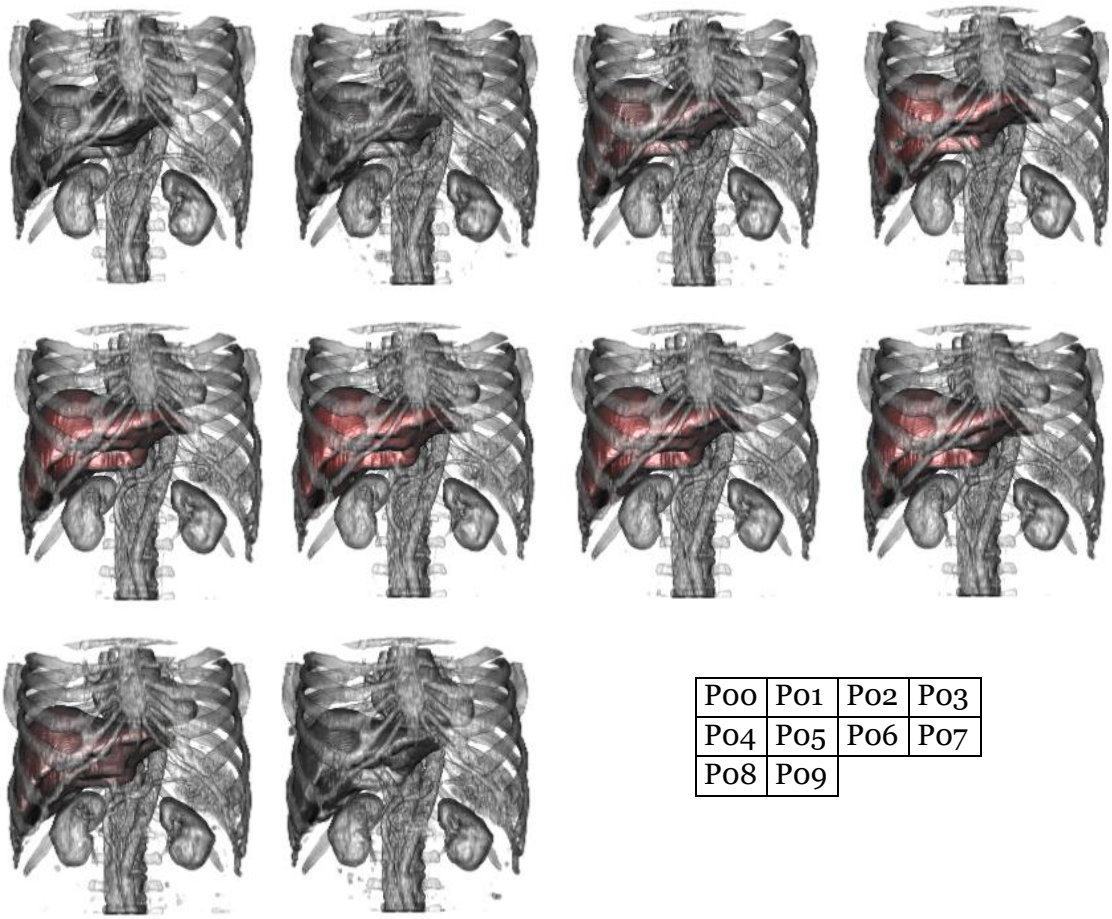

Figure 6-13 An example of correlation between liver motion and color transfer function

6.6 Summary

This chapter uses a ray-casting technique to demonstrate an example of liver-image segmentation application. First, the liver-segmented volume is integrated into the original 3D data before rendering. Next, the K-mean clustering is selected to show an example of multi-regions segmentation. Then, the clustering result is combined with the original 3D data and the liver-segmented volume. Actually, segmentation results are used to separate ranges of gray-intensities among liver-segmented volume, clustering result, and original 3D data. This separation helps a user to control opacity and color transfer functions. Thus, the combination of an original 3D data and segmentation results possibly enhance the visualization of anatomical structures. Lastly, the correlation between the color transfer function and the volume displacements is utilized to visualize liver's motion. However, this motion cannot be well visualized when the displacement value is small.

Chapter 7
Conclusion

This thesis consists of two main parts. The first part proposes the liver-image segmentation system based on a level-set method. It is aimed to segment a liver volume from 3D CT images. The proposed system contains three main modules.

The first module is utilized to transform a gray-intensity image into edge-image or confident region image (CRI) representation. Actually, the CRI representation is proposed to describe approximate liver-regions as homogeneous regions. Furthermore, good boundaries of anatomical structures are obtained by a combination of edge information.

The second module is created to perform a two-resolution level-set image segmentation approach. It consists of two main components. The first component conducts the initialization process for generating the initial zero level-set function. The second component computes the level-set evolution. This evolution is dependent on the speed or energy function, and this study proposes the modified Chan-Vese (MCV) model. Lastly, the segmentation results are refined in the last module.

The proposed system was applied to CT images acquired from four patients by a 4D-CT imaging system. Two main experiments were considered. First, influences of gray-intensity, edge, and confident region images were compared when the geodesic active contour (GAC), edge-based, and Chan-Vese (CV) methods were applied to control the level-set evolution. From experimental results, the use of confident region images possibly improves segmentation results from using gray-intensity or edge images. This improvement is occurred if the GAC or edge-based level-set method is utilized to propagate a given curve. Second, a performance of the proposed level-set method was investigated in a comparative assessment. Experimental results show that the use of confident region images and the proposed level-set method possibly outperforms other pairs.

For the second part, the results of liver-image segmentation are utilized to demonstrate two related applications. The first application is liver-tumor segmentation. This study proposes integration of modified Chan-Vese and spatial fuzzy C-mean clustering methods to segment tumor-regions in a noisy image. This study assumes the liver-segmented region contains tumor regions, and these tumor regions are possibly estimated by the clustering result. The clustering result is used to

create the initial zero level-set function and modify the Chan-Vese method. The proposed method was applied to an eight-bit mock liver-tumor image. From experimental results, if a given image includes some levels of image noises, the proposed level-set method possibly gives better segmentation result than the integration of an edge-base level-set model and a clustering method.

In the second application, the liver-segmented volume is used to demonstrate an example of enhancement in visualization application. In this application, the segmentation result is combined with the original 3D data before applying the ray-casting technique. This combination possibly improves visualization of anatomical structures. Furthermore, it is possible to control appearance of the segmented volume by adjusting opacity and color transfer functions. In addition, this study uses the color transfer function to visualize liver's motion when the 4D volume rendering is considered. The color of the liver volume is changed in accordance with an axis of the maximum displacement.

In this thesis, several interesting research topics will be possibly extended and investigated in the future. For example, creation of initial zero level-set function in the level-set image segmentation should be more simplified. Moreover, medical image segmentation in other organs, such as brain and heart, is also an impressive and challenging topic. In addition, 4D visualization of motion analysis possibly gives useful information for diagnosis.

Bibliography

[1] F. Ferlay J; Soerjomataram I; Ervik M; Dikshit R; Eser S; Mathers C; Rebelo M; Parkin DM; Forman D; Bray, *Cancer Incidence and Mortality Worldwide: IARC CancerBase No. 11,* GLOBOCAN 2012 v1.0.

[2] *Cancer research UK:Worldwide cancer mortality statistics, http://www. cancerresearchuk.org/cancer-info/cancerstats/world/mortality/#Trends.*

[3] Cancer.Net, *Liver Cancer, http://www.cancer.net/cancer-types/liver-cancer.*

[4] *American Cancer Society: Liver Cancer, http://www.cancer.org/cancer /livercancer/detailedguide/liver-cancer-treating-general-info.*

[5] Y. Nakayama, Q. Li, S. Katsuragawa, R. Ikeda, Y. Hiai, K. Awai, S. Kusunoki, Y. Yamashita, H. Okajima, Y. Inomata and others, "Automated Hepatic Volumetry for Living Related Liver Transplantation At Multisection CT 1," *Radiology,* vol. 240, no. 3, pp. 743-748, 2006.

[6] A. Barrett, J. Dobbsand, S. Morris and T. Roques, *Practical Radiotherapy Planning*, Hodder Arnold, An Hachette UK Company, 2009.

[7] S. B. Jiang, "Radiotherapy of mobile tumors," *Seminars in radiation oncology,* vol. 16, no. 4, pp. 239-248, 2006.

[8] M. Matoba, K. Oota, I. Toyoda, M. Kitadate, N. Watanabe and H. Tonami, "Usefulness of 4D-CT for Radiation Treatment Planning of Gastric MZBCL/MALT," *Journal of Radiation Research,* vol. 53, no. 2, pp. 333-337, 2012.

[9] P. Campadelli, E. Casiraghi and A. Esposito, "Liver segmentation from computed tomography scans:A survey and a new algorithm," *Artificial Intelligence in Medicine,* vol. 45, pp. 185-196, 2009.

[10] T. Heimann, B. van Ginneken, M. A. Styner and others, "Comparison and Evaluation of Method for Liver Segmentation from CT Datasets," *IEEE Transactions on Medical Imaging,* vol. 28, no. 8, pp. 1251-1264, 2009.

[11] A. M. Mharib, A. R. Ramli, S. Mashohor and R. B. Mahmood, "Survey on liver CT image segmentation methods," *Artificial Intelligence Review,* vol. 37, no. 2, pp. 83-95, 2012.

[12] A. Beck and V. Aurich, "Hepatux--a semiautomatic liver segmentation system," *Proceedings of MICCAI workshop on 3D Segmentation in The Clinic: A Grand Challenge*, 2007, pp. 225-233.

[13] R. Beichel, C. Bauer, A. Bornik, E. Sorantin and H. Bischof, "Liver segmentation in CT data: A segmentation refinement approach," *Proceedings of" 3D Segmentation in The Clinic: A Grand Challenge*, 2007, pp. 235-245.

[14] Y. Boykov and G. Funka-Lea, "Graph cuts and efficient ND image segmentation," *International journal of computer vision,* vol. 70, no. 2, pp. 109-131, 2006.

[15] A. Bornik, R. Beichel and D. Schmalstieg, "Interactive editing of segmented volumetric datasets in a hybrid 2D/3D virtual environment," *Proceedings of the ACM symposium on Virtual reality software and technology*, 2006, pp. 197-206.

[16] S. Pan and B. M. Dawant, "Automatic 3D segmentation of the liver from abdominal CT images: a level-set approach," *Medical Imaging 2001: Image Processing, Proceeding of SPIE,* vol. 4322, 2001, pp. 128-138.

[17] B. M. Dawant, R. Li, B. Lennon and S. Li, "Semi-automatic segmentation of the liver and its evaluation on the MICCAI 2007 grand challenge data set," *Proceedings of MICCAI workshop on 3D Segmentation in The Clinic: A Grand Challenge*, 2007, pp. 215-221.

[18] P. Slagmolen, A. Elen, D. Seghers, D. Loeckx, F. Maes and K. Haustermans, "Atlas based liver segmentation using nonrigid registration with a B-spline transformation model," *Proceedings of MICCAI workshop on 3D segmentation in the clinic: a grand challenge*, 2007, pp. 197-206.

[19] F. Maes, A. Collignon, D. Vandermeulen, G. Marchal and P. Suetens, "Multimodality image registration by maximization of mutual information," *Medical Imaging, IEEE Transactions on,* vol. 16, no. 2, pp. 187-198, 1997.

[20] D. Rueckert, L. I. Sonoda, C. Hayes, D. L. Hill, M. O. Leach and D. J. Hawkes, "Nonrigid registration using free-form deformations: application to breast MR images," *Medical Imaging, IEEE Transactions on,* vol. 18, no. 8, pp. 712-721, 1999.

[21] S. Osher and J. A. Sethian, "Fronts propagating with curvature-dependent speed: algorithms based on Hamilton-Jacobi formulations," *Journal of*

computational physics, vol. 79, no. 1, pp. 12-49, 1988.

[22] M. Sussman, P. Smereka and S. Osher, "A level set approach for computing solutions to incompressible two-phase flow," *Journal of Computational physics,* vol. 114, no. 1, pp. 146-159, 1994.

[23] C. Li, C. Xu, C. Gui and M. D. Fox, "Level set evolution without re-initialization: a new variational formulation," *Computer Vision and Pattern Recognition, 2005. CVPR 2005. IEEE Computer Society Conference on,* vol. 1, pp. 430-436, 2005.

[24] C. Li, C. Xu, C. Gui and M. D. Fox, "Distance regularized level set evolution and its application to image segmentation," *Image Processing, IEEE Transactions on,* vol. 19, no. 12, pp. 3243-3254, 2010.

[25] X. Xie, "Active contouring based on gradient vector interaction and constrained level set diffusion," *Image Processing, IEEE Transactions on,* vol. 19, no. 1, pp. 154-164, 2010.

[26] K. Zhang, L. Zhang, H. Song and D. Zhang, "Reinitialization-free level set evolution via reaction diffusion," *Image Processing, IEEE Transactions on,* vol. 22, no. 1, pp. 258-271, 2013.

[27] C. Li, C.-Y. Kao, J. C. Gore and Z. Ding, "Implicit active contours driven by local binary fitting energy," *Computer Vision and Pattern Recognition, 2007. CVPR'07. IEEE Conference on*, 2007, pp. 1-7.

[28] C. Li, C.-Y. Kao, J. C. Gore and Z. Ding, "Minimization of region-scalable fitting energy for image segmentation," *Image Processing, IEEE Transactions on,* vol. 17, no. 10, pp. 1940-1949, 2008.

[29] B. N. Li, C. K. Chui, S. Chang and S. H. Ong, "Integrating spatial fuzzy clustering with level set methods for automated medical image segmentation," *Computers in Biology and Medicine,* vol. 41, no. 1, pp. 1-10, 2011.

[30] V. Caselles, R. Kimmel and G. Sapiro, "Geodesic active contours," *International journal of computer vision,* vol. 22, no. 1, pp. 61-79, 1997.

[31] T. F. Chan and L. A. Vese, "Active contours without edges," *Image processing, IEEE transactions on,* vol. 10, no. 2, pp. 266-277, 2001.

[32] G. Aubert and P. Kornprobst, *Mathematical problems in image processing: partial differential equations and the calculus of variations*, vol. 147, Springer, 2006.

[33] B. Merriman, J. K. Bence and S. J. Osher, "Motion of Multiple Junction: A Level Set Approach," *Journal of Computational Physics,* vol. 112, no. 2, pp. 334-363, 1994.

[34] V. Caselles, F. Catt'e, T. Coll and F. Dibos, "A geometric model for active contours in image processing," *Numerische mathematik,* vol. 66, no. 1, pp. 1-31, 1993.

[35] S. Osher and N. Paragios, *Geometric Level Set Methods*, Sringer-Verlag New York, Inc.,, 2003.

[36] J. Lee, N. Kim, H. Lee, J. B. Seo, H. J. Won, Y. M. Shin, Y. G. Shin and S.-H. Kim, "Efficient liver segmentation using a level-set method with optimal detection of the initial liver boundary from level-set speed images," *Computer Methods and Programs in Biomedicine,* vol. 88, no. 1, pp. 26-38, 2007.

[37] R. T. Whitaker and X. Xue, "Variable-conductance, level-set curvature for image denoising," *Image Processing, 2001. Proceedings. 2001 International Conference on,* vol. 3, 2001, pp. 142-145.

[38] W. Narkbuakaew, H. Nagahashi, K. Aoki and Y. Kubota, "An Efficient Liver-Segmentation System Based on a Level-Set Method and Consequent Processes," *Journal of Biomedical Science and Engineering,* vol. 7, no. 12, pp. 994-1004, 2014.

[39] M. Sonka, V. Hlavac and R. Boyle, *Image processing, analysis, and machine vision*, Cengage Learning, 2007.

[40] N. Otsu, "A threshold selection method from gray-level histograms," *IEEE Transactions on system, man, and cybernetics,* Vols. SMC-9, no. 1, pp. 62-66, 1979.

[41] M. Sezgin and others, "Survey over image thresholding techniques and quantitative performance evaluation," *Journal of Electronic imaging,* vol. 13, no. 1, pp. 146-168, 2004.

[42] D.-Y. Huang and C.-H. Wang, "Optimal multi-level thresholding using a two-stage Otsu optimization approach," *Pattern Recognition Letters,* vol. 30, no. 3, pp. 275-284, 2009.

[43] D.-Y. Huang, T.-W. Lin and W.-C. Hu, "Automatic Multilevel Thresholding Based On Two-Stage Otsu's Method With Cluster Determination By Valley Estimation," *ICIC International Journal of Innovative Computing, Information*

and Control, vol. 7, no. 10, pp. 5631-5644, 2011.

[44] P.-S. Liao, T.-S. Chen and P.-C. Chung, "A fast algorithm for multilevel thresholding," *J. Inf. Sci. Eng.,* vol. 17, no. 5, pp. 713-727, 2001.

[45] Q. Hu, Z. Hou and W. L. Nowinski, "Supervised range-constrained thresholding," *IEEE Transactions on Image Processing,* vol. 15, no. 1, pp. 228-240, 2006.

[46] Y. Qiao, Q. Hu, G. Qian, S. Luo and W. L. Nowinski, "Thresholding based on variance and intensity contrast," *Pattern Recognition,* vol. 40, no. 2, pp. 596-608, 2007.

[47] X. Xu, S. Xu, L. Jin and E. Song, "Characteristic analysis of Otsu threshold and its applications," *Pattern recognition letters,* vol. 32, no. 7, pp. 956-961, 2011.

[48] K. Iniewski, Medical imaging: *Principles, detectors, and Electronics*, John Wiley & Sons, 2009.

[49] N. B. Smith and A. Webb, *Introduction to medical imaging: Physics, engineering and clinical applications*, Cambridge University Press, 2010.

[50] D. W. Jones, P. Hogg and E. Seeram, *Practical SPECT/CT in nuclear medicine*, Springer, 2013.

[51] R. Keith R. Britton and Lei Dong and Mohan, "Image-Guide Rationtherapy Lung Cancer," R. James D. Cox and Joe Y. Chang and Komaki, Ed., Informa Healthcare USA, 2008, pp. 63-81.

[52] L. R. Dice, "Measures of the amount of ecologic association between species," *Ecology,* vol. 26, no. 3, pp. 297-302, 1945.

[53] L. F. de Manuel, J. L. Rubio, M. J. Ledesma-Carbayo, J. Pascau, J. M., Tellado, E. Ramón, M. Desco and A. Santos, "3D Liver Segmentation in Preoperative CT Images using a Level-Sets Active Surface Method," *31st Annual International Conference of the IEEE EMBS*, 2009, pp. 3625-3628.

[54] K.-S. Chuang, H.-L. Tzeng, S. Chen, J. Wu and T.-J. Chen, "Fuzzy c-means clustering with spatial information for image segmentation," *computerized medical imaging and graphics,* vol. 30, no. 1, pp. 9-15, 2006.

[55] J. C. Bezdek, R. Ehrlich and W. Full, "FCM: The fuzzy c-means clustering algorithm," *Computers & Geosciences,* vol. 10, no. 2, pp. 191-203, 1984.

[56] K. Zhang, L. Zhang, H. Song and W. Zhou, "Active contours with selective local or global segmentation: a new formulation and level set method," *Image and*

Vision computing, vol. 28, no. 4, pp. 668-676, 2010.

[57] D. E. Knuth, *The Art of Computer Programming*, Volume 2: Seminumerical Algorithms, The, Addison-Wesley Professional, 1969.

[58] W. Narkbuakaew, H. Nagahashi, K. Aoki and Y. Kubota, "Level-Set Image Segmentation based on Integration of Artificial Balloon and Signed Pressure Forces," *Proceeding of the Fourth IIEEJ International Workshop on Image Electronics and Visual Computing 2014 (IEVC2014),* pp. [1A-1]1--6, 2014.

[59] R. Gonzalez and R. Woods, Digital Image Processing, Prentice Hall, 2008.

[60] D. Comaniciu and P. Meer, "Mean shift: A robust approach toward feature space analysis," *Pattern Analysis and Machine Intelligence, IEEE Transactions on,* vol. 24, no. 5, pp. 603-619, 2002.

[61] W. E. Lorensen and H. E. Cline, "Marching cubes: A high resolution 3D surface construction algorithm," in *ACM Siggraph Computer Graphics*, 1987.

[62] W. Schroeder, K. Martin and B. Lorensen, *The Visualization Toolkit: An object-oriented approach to 3D Graphics*, Pearson Education, Inc., 2002.

[63] K. Engel, M. Hadwiger, J. M. Kniss, A. E. Lefohn, C. R. Salama and D. Weiskopf, "Real-time Volume Graphics," *ACM SIGGRAPH 2004 Course Notes,* 2004.

[64] G. Chen, "COSC6344 Visualization (Fall2014)," 2014.

[65] W. J. Schroeder, L. S. Avila and W. Hoffman, "Visualizing with VTK: a tutorial," *Computer Graphics and Applications, IEEE,* vol. 20, no. 5, pp. 20-27, 2000.

[66] C. M. Bishop and N. M. Nasrabadi, Pattern recognition and machine learning, vol. 1, springer New York, 2006.

[67] W. Narkbuakaew, H. Nagahashi, K. Aoki and Y. Kubota, "Bone Segmentation in CT-Liver Images Using K-Means Clustering for 3D Rib Cage Surface-Modeling," *WSEAS Transactions on Biology and Biomedicine,* vol. 11, pp. 183-193, 2014.

[68] L. Ibanez, W. Schroeder, L. Ng and J. Cates, "The ITK software guide," 2003.

Publication List

Journal papers

Walita NARKBUAKAEW, Hiroshi NAGAHASHI, Kota AOKI, and Yoshiki KUBOTA, "An Efficient Liver-Segmentation System Based on a Level-Set Method and Consequent Processes," *Journal of Biomedical Science and Engineering*, vol. 7, no. 12, pp.994-1004, 2014.

Walita NARKBUAKAEW, Hiroshi NAGAHASHI, Kota AOKI, and Yoshiki KUBOTA, "Bone Segmentation in CT-Liver Images Using K-Means Clustering for 3D Rib Cage Surface-Modeling," *WSEAS Transaction on Biology and Biomedicine*, vol. 11, no. 24, pp.183-193, 2014.

International conferences

Walita NARKBUAKAEW, Hiroshi NAGAHASHI, Kota AOKI, and Yoshiki KUBOTA, "Liver Segmentation Based on Reaction-Diffusion Evolution and Chan-Vese Model in 4DCT," *Biomedical Informatics and Technology*, *First International Conference, ACBIT 2013, Aizu-Wakamatsu, Japan, September 16-17, 2013. (Revised Selected Papers), Series: Communications in Computer and Information Science (CCIS), Springer Berlin Heidelberg,* vol. 404, pp. 138-149, 2014.

Walita NARKBUAKAEW, Hiroshi NAGAHASHI, Kota AOKI, and Yoshiki KUBOTA, "Integration of Modified K-Means Clustering and Morphological Operations for Multi-Organ Segmentation in CT Liver-Images," *Recent Advances in Biomedical & Chemical Engineering and Material Science, Proceeding of the 2014 International Conference on Biology and Biomedical Engineering (BBE'14),Venice, Italy, March 15-17, 2014*, pp. 34-39.

Walita NARKBUAKAEW, Hiroshi NAGAHASHI, Kota AOKI, and Yoshiki KUBOTA, "Level-Set Image Segmentation based on Integration of Artificial Balloon and Signed Pressure Forces," *Proceeding of the Fourth IIEEJ International Workshop on Image Electronics and Visual Computing 2014 (IEVC2014), Koh Samui, Thailand, October 7-10, 2014,* [1A-1], pp.1-6.